Atomistic Simulation of Uranium Dioxide Interfaces

Williams, Nicholas

Award date:
2014

Awarding institution:
University of Bath

Atomistic Simulation of Uranium Dioxide Interfaces

Nicholas Richard Williams

A thesis submitted for the degree of Doctor of Philosophy

University of Bath

Department of Chemistry

March 2014

Contents

Abstract

The aim of work described in this thesis is to gain insight into the role of interfaces on atomic transport processes in polycrystalline uranium dioxide at high temperatures. Previous studies have highlighted the importance of grain boundaries as fast diffusion pathways and their potential to significantly effect the oxidation of nuclear fuel samples. The effect of interfacial transport is also significant in terms of helium produced through the α-decay of actinides throughout the life-cycle of nuclear fuels. The resultant swelling can have important implications for the long term storage of nuclear materials and can even lead to radionuclide release.

Chapter 1 comprises a review of the relevant literature focussing on the uranium oxide system, oxide microstructure and the transport properties of both helium and oxygen. In Chapter 2 the computational methodologies used throughout this investigation are described in detail including both energy minimisation and molecular dynamics. Chapter 3 focuses on the development of a new potential for uranium dioxide derived to be computationally efficient and suitable for large simulation cells. Additionally the model needed to be capable of modelling the high temperature structures of tilt and twist grain boundaries and accurately representing oxygen transport. Having developed and validated the model, we explored protocols for generating grain boundaries and in Chapters 4 and 5 model a range of tilt and twist grain boundaries. In each case the structure, stability and transport properties of each were investigated in depth. Chapter 6 introduces a new helium potential model and uses it to evaluate the diffusion and segregation in a range of tilt grain boundaries. Also introduced is a new type of interface that models the interface where grain boundaries and surfaces meet. The approach of routinely generating such interfaces is explored and is then applied to look at the release of helium from bulk UO_2 to the gas phase. The thesis concludes in Chapter 8 with a summary of the thesis and possible direction of future work.

Acknowledgements

First of all I would like to say an enormous thank you to my supervisor, Professor Steve Parker. Steve was my personal tutor as an undergraduate as well as my PhD supervisor and has constantly supported me throughout my time at university. Without his enthusiasm and belief it is highly unlikely I would be in the position I am in today.

Another big thank you must go to Dr Marco Molinari, whose extensive knowledge of grain boundaries has made this investigation possible. I would also like to thank Parker group members past and present, especially Tom Shapley and Stephen Yeandle for their help with technical problems as well as Nick Brincat, Joe Flitcroft and Richard Driscoll for their thorough proof reading.

I would like to thank AWE for funding my research and to acknowledge the materials chemistry consortium for HECToR time and the Bath HPC Aquila facility.

Finally I must say thank you to my family and friends for their support especially during the final few months with a special mention must also be made to Alistair and Josh for allowing me to sleep on their floor for extended periods while writing up.

Publications and Presentations

Publications:

Williams, N. R.; Parker S. C.; Molinari, M.; Storr, M. Structure, Stability and Transport Properties of Tilt Grain Boundaries in UO_2 (in preparation)

Presentations:

Atomistic simulation of oxygen transport in actinide oxides and at their interfaces

Poster, Chemistry Postgraduate Symposium, Internal, May 2011

Atomistic simulation of oxygen transport in actinide oxides and at their interfaces

Poster, 21st Goldschmidt Conference, Prague, Czech Republic, August 2011

Atomistic simulation of oxygen transport in actinide oxides and at their interfaces

Poster, South West Computational Chemistry Meeting, Cardiff University, September 2011

Atomistic Simulation of Structure and Transport Properties in Polycrystalline UO_2

Poster, RSC Solid State Chemistry Group Christmas Meeting, University of Liverpool, December 2011

Simulation of Structure and Dynamic Properties of Binary Oxides

Poster, Materials Chemistry Consortium Meeting, UCL, March 2012

Oxygen diffusion in polycrystalline UO_2

Talk, Second Year Talks, Internal, April 2012

Oxygen diffusion in polycrystalline UO_2

Talk, AWE Research Symposium, Aldermaston, May 2012

Atomistic simulation of structure, stability and transport at actinide oxide interfaces

Poster, AWE Materials Science Exhibition, Aldermaston, May 2012

Atomistic simulation of oxygen transport in actinide oxides and at their interfaces

Poster, ATALANTE 2012, Montpellier, September 2012

Computer Modelling of Defect Structures in Actinide Oxides

Poster, CCP5-MDNet Meeting, University of Warwick, April 2013

Oxygen diffusion in polycrystalline UO_2

Talk, Chemistry Postgraduate Symposium, Internal, May 2013

Atomistic Simulation of Structure and Transport Properties in Polycrystalline UO_2

Talk, AWE Materials Symposium, Aldermaston, May 2013

Atomistic Simulation of Structure and Transport Properties in Polycrystalline UO_2

Talk, 9th European Conference on Computational Chemistry, Sopron, Hungary, September 2013

Chapter 1

Introduction

1.1 Uranium Dioxide as a Nuclear Fuel

Actinides such as uranium and its oxides are receiving increasing attention recently as a result of renewed interest in nuclear fuels not least because of awareness of issues associated with CO_2 emissions, security of energy supply and waning fossil fuel reserves [1]. Nuclear energy has the potential to generate vast amounts electricity at a competitive price and on a commercial scale without producing CO_2 emissions [2]. This along with the fact that 66% of the worlds greenhouse gas emissions [3] are as a result of electricity generation suggests nuclear energy can have a large role to play in future energy production and the drive to reduce dependence on fossil fuels. However promising as a clean energy source, there are still significant technical challenges that need to be overcome. These challenges centre around the hazardous nature of UO_2 and the need to more accurately understand the evolution of the fuel over all aspects of its lifespan whether under reactor conditions or in long term storage. Computational techniques provide an valuable method in which to investigate the behaviour of nuclear fuels not only by providing a safe method of study, but also by providing a better understanding of its material properties at an atomistic scale.

Uranium dioxide (UO_2) is a technologically important material, the primary use of which is in the production of electricity in nuclear power stations. Its suitability stems from its ability to produce incredibly large amounts of energy that can be obtained from a relatively small amount of fuel, especially when compared with other conventional sources of electricity.

In 2011, 435 nuclear reactors were in operation with another 108 under construction or on order worldwide providing a total of 478 GW*e* of electrical capacity [3]. In the same year nuclear energy accounted for 12% of total worldwide electricity generation [4]. In 2013 the UK government committed to the construction of a new two reactor power station at Hinckley Point in Somerset. The first new nuclear power station to be built in the UK since Sizewell B in 1995.

Large scale research into actinide oxides as nuclear fuels started in the 1950's [5] and since then a large number of different reactor types and designs have been utilised. By far the most common of these is the pressurised light water reactor (PWR) which accounts for 61% of all reactors [3] and uses UO_2 as its primary fuel. The reason UO_2 has been so widely adopted as the nuclear fuel of choice is as a result of the desirable properties it exhibits. These include its innate chemical stability, the ability to incorporate large numbers of fission products within the structure without severe distortion of the material and the ability of the fluorite lattice to maintain its structure over a wide range of temperatures [6, 7] .

A major problem in the life cycle of nuclear fuels is the tendency of UO_2 to oxidise at high temperatures. Oxidation of nuclear fuels can have major implications for the safe running and storage, it can cause swelling of the material as well as altering thermal performance, changes in local burn up and physical properties. UO_2 has an incredibly complex microstructure due to both the high reactor temperatures to which it is subjected and as a result of the fission process and the high energy collisions that take place. The rate of oxidation is determined by the transport properties of UO_2 which in turn is dependent on the fuel's microstructure. However there are gaps in our understanding of this process particularly with respect to the role of extended defects such as grain boundaries. The effect on transport properties of the oxide microstructure is relevant not just to fuel oxidation but also to the behaviour of fission gases such as helium. Produced as a result of α-decay, helium can also cause fuel swelling as well as altering thermal properties and leading to radionuclide release.

1.1.1 Reactor Operation

Nuclear reactors produce electricity through heat generated by nuclear fission, a process that is sustained by the collision of neutrons with uranium atoms. Coolant removes heat

from the reactor core and generates steam. In some reactor types, coolant passes through a heat exchanger to produce steam to drive turbines whereas in others turbines are driven directly by the coolant. Fast neutrons are produced as product of nuclear fission and once slowed down are referred to as thermal neutrons. There are two main types of reactors and these are named after these neutrons. Fast reactors do not use a moderator whereas thermal reactors use a moderator to slow neutrons down. Thermal reactors make up all of the world's currently operational commercial nuclear reactors.

1.1.1.1 Thermal Reactors

Nuclear fission, the process which generates the heat within a nuclear reactor is the result of neutrons colliding with the uranium fuel. The result of one of these collisions is that the uranium atom involved in the collision splits. As well as heat being generated, fission also creates two roughly even sized atoms known as fission products and more neutrons. If this were to occur between an isolated neutron and uranium atom then only a small amount of heat would be released and any neutrons produced would likely be travelling too quickly to be able to interact with any further uranium atoms.

Thermal nuclear reactors typically use water or graphite to moderate these neutrons, slowing them down and increasing their chances of interacting with uranium atoms. Selecting the correct amount of moderator enables a chain reaction to occur where fission generates more neutrons than it requires. It is also essential that the amount of nuclear material is sufficient to enable this chain reaction to continue. This is often referred to as criticality and the term critical mass refers to the amount of uranium needed to sustain a nuclear reaction. Excess neutrons are absorbed by control rods ensuring the chain reaction does not increase progressively and to make sure the reaction produces a constant level of heat.

The chain reaction within a reactor is started by withdrawing the control rods allowing the number of free neutrons within the system to increase. The control rods are withdrawn to a position where the number of neutrons being produced is slightly more than those being absorbed, starting a chain reaction. In order to vary the heat and therefore electrical output of a reactor the position of the control rods can be varied. Control rods are also used to shut down a reactor by inserting them fully into the fuel core stopping the chain reaction. Other neutron absorbing media are often used to help stop the reaction in the instance of an

emergency. There are a number of different types of thermal reactors including Pressurised Water Reactors, Advanced Gas-cooled Reactors, Boiling Water Reactors, CANDU Reactors and Boiling Water Graphite Moderated Reactors.

1.1.1.2 Fast Reactors

As previously mentioned, the main difference between a fast and thermal reactor is that in a fast reactor the neutrons produced through fission are not moderated and remain at very high energies. As a consequence fuels for fast reactors need to contain more fissile material. The chain reaction is sustained instead by including fertile material as part of the fuel and by surrounding the reactor with a material that reflects neutrons back into the core. Fertile material captures neutrons from the reaction, creating plutonium which releases more neutrons to sustain the reaction. For this reason fast reactors are often referred to as breeder reactors as they 'breed' their own fuel.

1.2 The Uranium Oxide System

The oxygen uranium system in nuclear fuels is incredibly complex as a result of the range of oxidation states in which uranium can exist (U^{3+}- U^{6+}). This range of stable oxidation states and the ready oxidation of UO_2 at high temperatures give rise to the existence of 16 non-stoichiometric oxides between UO_2 and UO_3 [1]. Many of these oxides contain uranium atoms of varying charge states which are poorly understood. Of all the known oxides of uranium the principle stable structures consist of UO_2, U_4O_9, U_3O_8 and UO_3 while the other oxides tend to be only metastable [8]. Due to the complexity of the system many of the intermediate oxides and in particular the oxides that are only metastable are poorly characterised with little more than structural data available in the literature. The complexity of the U/O system is illustrated by the phase diagram in Figure 1.1.

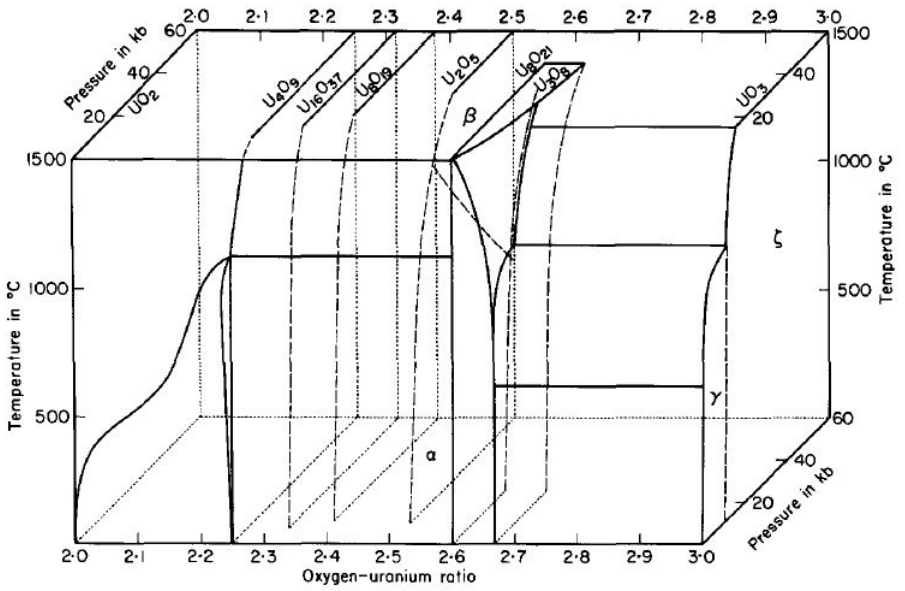

Figure 1.1: Phase diagram for the U/O system in the UO_2 - UO_3 composition range [9].

UO_2 is the most widely studied and by far the most characterised of all the uranium oxides due to its technical importance. It is a fluorite type structure with the $Fm-3m$ space group. Oxygen atoms in stoichiometric UO_2 are tetrahedrally coordinated whilst the uranium atoms have cubic coordination. The full structure of the UO_2 unit cell can be seen in Figure 1.2.

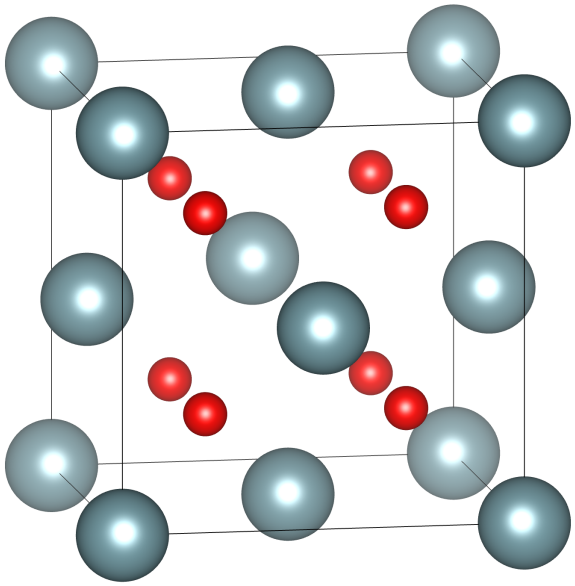

Figure 1.2: The full UO_2 unit cell. Uranium ions are shown in blue, while oxygen ions are shown in red.

Whilst not shown in the phase diagram, oxides with oxidation states lower than 4+ are thought to exist. The solubility of oxygen in uranium metal has been shown to increase with temperature and can reach a composition of up to $UO_{0.05}$ at 2700 K [10]. At this temperature solid $UO_{1.65}$, liquid $UO_{1.46}$ and $UO_{0.05}$ are all known to exist at equilibrium [8]. Previously there have been suggestions that initial oxidation of uranium metal gave rise to the stoichiometric oxide UO [11], however despite a number of studies focusing on this oxide [12, 13] no claims have been suggested relating to the synthesis of bulk UO [14]. This has lead to the suggestion that the UO previously reported as synthesised is in fact either uranium oxycarbide (UC_xO_{1-x}) or uranium oxynitride (UN_xO_{1-x}) [14]. Hypostoichiometric UO_2 (UO_{2-x}) has also been observed however it is only stable at very high temperatures [15]. UO_{2-x} is based on the cubic UO_2 structure but incorporates oxygen vacancies [16].

In addition to the inclusion of oxygen vacancies to form non-stoichiometric oxides, UO_2 is known to incorporate oxygen atoms in interstitial positions (shown in Figure 1.3) within the fluorite structure to form hyperstoichiometric UO_2 or UO_{2+x} [17]. However these interstitial defects are present only in stoichiometry ranges that are close to 2.0 [18] At increased hyperstoichiometry levels different structures are observed.

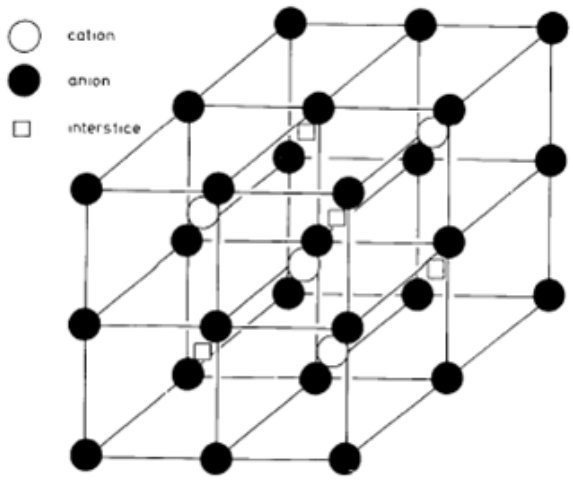

Figure 1.3: Interstitial positions in UO_2 [17].

At increased hyperstoichiometry ranges structures of complex defects are observed, such as the Willis cluster [19] that constitutes the structure of $UO_{2.12}$. Willis clusters are formed as a result of interstitial oxygen atoms displacing lattice oxygen to create more interstitial atoms

and in the process forming oxygen vacancies at the vacant oxygen sites. The combination of two additional gas phase oxygen atoms along with a displaced lattice oxygen ion and the vacancy formed as a result give rise to the di-interstitial cluster (a more detailed description of these clusters can be found in section 1.3.1). Any further oxygen can be incorporated via long range ordering of interstitials producing the U_4O_{9-y} phase which is stable up until 1400 K and has a stoichiometry of $UO_{2.245}$ [20].

U_4O_9 is an intermediate product of oxidation with a similar structure to UO_2 and is only stable at temperatures lower than 673K [21]. Three polymorphs of U_4O_9 exist, namely α, β and γ. The only well characterised phase is β-U_4O_9. While attempts have been made to discover the exact structures of the alpha and gamma phases, no attempt has so far been successful. Some structural information for the alpha phase such as the space group is known and work is being done to try and refine neutron diffraction data [22]. The α phase is thought to have a rhombohedral structure, has the space group R3c and is stable at temperatures below 328 K. The β and γ phases however are cubic with the space group $I-43d$. The β phase is stable at temperatures between 338 K and 873 K whereas γ-U_4O_9 is the high temperature phase existing only above 873 K [23]. All three phases of U_4O_9 have a large unit cell compared to UO_2, the structure of which has been described as a fluorite sublattice with a superimposed oxygen superlattice [18].

Similar to U_4O_9, the crystal structure of U_3O_7 resembles the fluorite structure of UO_2 and is normally produced as a result of high pressure oxidation or alternatively when UO_2 percolates into water [24]. U_3O_7 is metastable and an intermediate production of oxidation towards U_3O_8. One monoclinic and three tetragonal phases of U_3O_7 exist, all of a similar size to UO_2 [25]. As with a large number of the intermediate oxides, the charge states of the uranium ions are unknown. Little is also known about U_2O_5 which marks the transition point between the fluorite based structures and the reduced density structures featuring uranyl type bonds. However three phases have been synthesised by Hoekstra et al. [9].

U_3O_8 is the most stable of the intermediate oxides and as a result is the major oxidation product from the nuclear fuel cycle and long term storage of UO_2 [21, 26]. For this reason it is the most studied of the intermediate oxides, however while this may be the case the majority of focus has centred on structural studies and there is still some debate about the charge states of uranium in U_3O_8. This arises from the fact that assuming all the oxygen atoms are in the state O^{2-}, a variation in oxidation sates must be observed between the

uranium ions in order to balance the charges. Computational studies suggest a U^{5+}/U^{6+} [27] which doesn't agree with x-ray photoelectron spectroscopy studies suggesting a U^{4+}/U^{6+} arrangement [28, 29]. The oxidation of $U_4O_9$to U_3O_8 results in significant swelling of the material corresponding to a reduction in density from about 11 g cm^{-3} for UO_2 [9] to approximately 9gcm^{-3} and an increase in volume of 36% [30]. This change in density results from the transition from fluorite type structures to layered structures. U_3O_8 has a number of crystalline polymorphs. Of these the α and β forms share similar structures, with α existing in the *AMM*2 space group [31] and β in the *CMCM* space group [32], and both of these phases are stable at room temperature [8]. The structure of α-U_3O_8 was first characterised by Loopstra [31]. It adopts a pseudo-hexagonal orthorhombic structure that consists of layers of UO_5 pentagons that share edges. Perpendicular to the layers the UO_5 pentagons are connected by chains consisting of U-O-U-O [33], the structure of which can be seen in Figure 1.4.

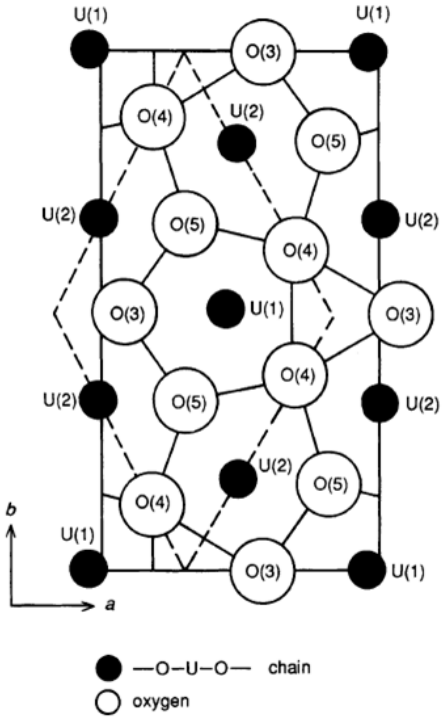

Figure 1.4: Structure of α-U_3O_8 [33].

In a similar way to many of the other uranium oxides, U_3O_8 can incorporate a range of stoichiometry from $2.64 \leq O/U \leq 2.68$ [34]. The orthorhombic structure of α-U_3O_8 persists all the way to UO_3 where all uranium atoms have a charge of +6. UO_3 is known to exist in

7 crystalline phases as a result of the range of coordination states which the uranium atoms can adopt [35]. UO_3 is based on α-U_3O_8 with 12% less uranium ions [36].

1.3 Fuel Microstructure

The microstructure of UO_2 is complex, incorporating a range of point and extended defects including grain boundaries and dislocations. In addition to this a range of fission products can be present within nuclear fuels as well as gases released as a result of $\alpha-$decay. The process of defect formation is driven entropically by the high temperatures encountered during power generation. The presence of these defects can have significant implications for the properties of UO_2 and as a result significant research has focused on these structures. In this section the different types of defects present in UO_2 are discussed.

1.3.1 Point Defects and Clusters

A variety of point defects are found within nuclear fuels including both anion and cation vacancies, interstitial ions, divacancies, trivacancies as well as a range of clusters [16]. In some cases the presence of defects and clusters is directly linked to the formation of non-stoichiometric uranium oxides discussed in Section 1.2.

1.3.1.1 Intrinsic Point Defects

The experimental energies of both anion (equation 1.1) and cation (equation 1.2) Frenkel pairs as well as Schottky defects (equation 1.3) were summarised by Matzke [16]. The experimental energy values quoted suggest that the most favourable and therefore most likely defect to form is the oxygen Frenkel defect. These consist of an oxygen vacancy as well as an interstitial oxygen atom. Matzke also discusses a thermodynamic model [37] for predicting the quantity of defects present in stoichiometric, hypo and hyperstoichiometric UO_2. However this ignores any clustering effects and does not include the effect of entropy. Alongside the experimental defect energies, there have been a number of theoretical studies [38–40] using a variety of methods and reproducing defect energies to varying degrees of accuracy. Details can be found in section 3.3.3 where literature values are compared with the

results of this investigation. Defect energies determined using a large number of different UO_2 potentials are detailed in work by Govers [41].

$$O_O^x \rightarrow V_{\ddot{O}} + O_I^{''} \tag{1.1}$$

$$U_U^x \rightarrow V_U^{''''} + U_I^{\cdots} \tag{1.2}$$

$$2O_O^x + U_U^x \rightarrow 2V_{\ddot{O}} + V_U^{''''} + \mathrm{U}O_{2_{SURFACE}} \tag{1.3}$$

Interstitial oxygen atoms within a UO_2 lattice are known to cause the material to swell. At low concentrations these interstitial oxygen ions have been shown to occupy the interstitial sites in the uranium sub-lattice [42]. It has however also been observed that interstitial oxygen atoms can occupy sites displaced from the octahedral interstitial sites. Using neutron diffraction techniques Willis [43] identified two distinct oxygen positions (O' and O") each approximately 1 Å from the octahedral interstitial hole in different directions. These observations were backed up by potential based calculations by Catlow [44] who calculated the relative energy of distortion for both sites compared to the octahedral interstitial hole as well as by electronic structure calculations [45].

1.3.1.2 Extrinsic Point Defects

Fuel burn-up results in the formation of a large number of different decay products including products in solid solution, volatile products, oxide precipitates and metal precipitates [46]. The consequences of the presence of fission products within UO_2 is swelling of the fuel caused by either bubbles of fission gas or solid precipitates [47]. Literature investigations into fission products have often focused on the determination of solution and migration energies as well as the bubble growth of insoluble fission gases. Grimes and Catlow [46, 48] modelled the incorporation of the fission products; Xe, I, Ba, Kr, Rb and Br using pair potentials. They demonstrated that the charge state of the solvated fission product is dependent on the stoichiometry of the fuel. In UO_{2-x} where oxygen vacancies are present

iodine should be present only as I^-. However in UO_{2+x} iodine demonstrated it can be stable as either I^- at oxygen lattice sites or I^+ at uranium lattice sites. This was further demonstrated in a later study [49] where a larger range of fission products were studied (Br, Kr, Rb, Sr, Y, Zr, Te, I, Xe, Cs, Ba, La and Ce). By calculating solution energies at different positions within the UO_2 lattice and using variable charge states and stoichiometry it was found that Y, La and Sr are soluble in UO_2 and UO_{2+x}. Cs, Rb, Sr and Ba are soluble only in UO_{2+x} with Cs, Rb and Ba being most stable as binary oxide precipitates. I, Br and Te as cations are more stable in UO_{2+x}, but in UO_2 and UO_{2-x} an anion charge state is favoured. There has also been significant study of the diffusion behaviour of fission products [50–52]. The diffusion behaviour of helium produced as a result of α-decay is discussed in detail in section 1.4.2.

1.3.1.3 Defect Clusters

Oxygen interstitials in the UO_2 lattice undergo stabilisation as a result of clustering with other defects, the ensuing clusters further enhance the swelling effect noted for individual interstitial anions and affecting a reduction in the mechanical stability of the oxide [49]. A large number of clusters have been identified within the U/O system and as mentioned earlier in some cases may be related to the structures of some of the intermediate oxides discussed in section 1.2. The Willis or 2:2:2 cluster is one of the most well known. It is named for the fact that it consists of 2 oxygen vacancies, 2 O' interstitials and 2 O" interstitials [17]. Each of the two sets of interstitial oxygen ions occupy two separate sets of lattice position. From XPS results it has also been suggested that groups of 2:2:2 clusters can form chains in UO_{2+x} (for $x<0.25$). Higher values of x were linked to an increase in length and size of cluster chains [53]. In addition to the 2:2:2 cluster Catlow [38] predicted a 1:2:2 structure at low concentrations of x although as yet no experimental evidence has been found to confirm this. Another cluster the 4:3:2 has been proposed [54] and found to be energetically favourable using atomistic calculations [38]. Allen [20] proposed a method for the construction of 4:3:2 clusters via the combination of 2:2:2 clusters and oxygen interstitials. Another cluster, the cuboctahedron has been proposed in other fluorite structured materials and its possible existence in UO_2investigated [55]. Allen et al. [20] used x-ray photoelectron spectroscopy experiments to predict that the structure of the cuboctahedron in UO_2 consists of a cube of 8 oxygen vacancies is surrounded by 12 oxygen interstitials,

while there is some dispute as to the occupation at the centre of the cluster. Catlow et al. [38] suggest the presence of a pair of interstitial oxygen ions whereas Bevan suggests that it is empty [56]. The energetics of a range of clusters including both Willis-type clusters and cuboctahedrons were determined by Geng et al [45]. It was found that in UO_{2+x} cuboctahedral clusters will be more favoured the higher the value of x.

1.3.2 Extended Defects

Nuclear fuels are generally polycrystalline in nature but, due to the difficulty in modelling these systems only a few studies exist. Some of the most important features of these systems are grain boundaries, which can have a dramatic impact on material properties [57]. A grain boundary is defined as the interface between two differently orientated crystalline grains [57]. Different types exist including both tilt and twist systems. Attempts have been made to model polycrystalline systems. Sayle et al. [58] developed a model to produce large polycrystalline materials which by selecting differently sized nanoparticles from a library allows control of grain size distribution. The model developed in this study was then used to investigate the effect of grain boundary networks on fission gas diffusion. More recently Govers and Verwerft [51] used atomistic potentials to model high temperature uranium, oxygen and xenon diffusion in nano-polycrystalline UO_2. By investigating grain boundaries and other extended defects it is hoped that greater insight can be gained into the behaviour of polycrystalline systems. For UO_2 literature on grain boundaries is scarce, however there have been numerous studies into the effect of grain boundaries in other fluorite structured materials.

1.3.2.1 Surfaces

The low Miller index surfaces of UO_2 have been characterised using both LEED (low energy electron diffraction) [59–61] and scanning electron microscopy [62–64] techniques. The energy and relaxation of (111), (110) and (100) surfaces of UO_2 was investigated by Skomurski et al. [65]. Surfaces were evaluated using both quantum mechanical and atomistic potential methods. Agreement was found between the relative energies of the surfaces calculated by both quantum mechanical and potential methods but the absolute values of the surfaces differ depending on the method and/or potential used. The (111) surface was most

stable in all cases with (100) being the least stable. Abramowski et al. [66] investigated the growth of grains within UO_2 using five different potential models. Abramowski concluded that if allowed to form under equilibrium conditions UO_2 nano crystals will form an octahedron showing only (111) faces. On the other hand it was also observed that if thermodynamic equilibrium was not reached and the formation of nano crystals was dependent on kinetic factors then (111) surfaces are still dominant but a truncated octahedron is formed with (200) facets. Similar studies of nanoparticles in CeO_2 also show the formation of (111) terminated octahedra with (100) truncations [67].

The effect of adding water to the low Miller index surfaces was investigated using quantum mechanical techniques [68]. The study showed that dissociated water is less stable than molecular water when adsorbed to the surface. It was also found that the rate of oxidation of the (111) surface was significantly enhanced if water is present so much so that it is almost instantaneous. If however no water is present then the rate of oxidation is very slow. Increased oxidation rate in the presence of water results from the change in the electronic structure near the surface.

1.3.2.2 Tilt Grain Boundaries

Tilt grain boundaries are defined by having an axis of rotation that is parallel to the plane of the boundary. A number of models have been developed to model tilt grain boundaries including the dislocation model, CSL theory and the structural unit model. Further information on modelling grain boundaries can be found in chapter 4. Grain boundaries in ceramic materials are often characterised by open structures which have reduced atomic densities when compared to the bulk [57]. This is in contrast to what is often observed in similar structures in metals.

Nerikar et al. [69] investigated the distribution and structure of grain boundaries within a sample of UO_2, finding that nuclear fuel samples contain both general grain boundaries and coincident site lattice boundaries. This investigation also details the different CSL boundaries that are found in the sample. Studies of the structures of both the $\Sigma 3(111)$ and $\Sigma 5(310)$ tilt boundaries showed that the $\Sigma 3$ system had a lower grain boundary formation energy. A similar study has been performed on CSL grain boundary distribution in alumina and zirconia and its dependence on sintering temperature by Vonlanthen and Groberty [70]. It was

found that for both materials the percentage of grain boundaries that are CSL boundaries is higher in experimental samples than was predicted by simulated models. Also noted is the particular prevalence of the $\Sigma 3$ grain boundary.

The segregation of defects to grain boundaries is a well known phenomena with significant research focusing on this property especially in relation to effects on structure and properties. Lei et al. [71] used Z-contrast imaging and electron energy loss spectroscopy (EELS) to investigate the composition of grain boundaries in both yttria stabilised zirconia (YSZ) and Gd-doped ceria. They observed the segregation of oxygen vacancies to the grain boundary core in both materials and as a result predicted similar behaviour for all fluorite structured materials. Baik et al. [72] predicted similar behaviour in HfO_2 using a combination of electron microscopy, EELS and first principles theory to further support this idea. The energetics of oxygen vacancies at the grain boundaries were investigated by Marinopoulos et al. [73] for the $\Sigma 5(310)$ boundary in YSZ using first principles calculations. They found that vacancies formed in the boundary were the most favourable, suggesting that oxygen vacancies will segregate to this point. However even though the majority of the vacancy formation energies at the boundary were favourable no overall correlation can be seen between defect energy and distance from the interface.

Dickey et al. [74] used Z-contrast scanning electron microscopy to analyse the structures of the $\Sigma 13(510)$ and $\Sigma 5(310)$ tilt boundaries in YSZ. The structure characterised for the $\Sigma 5(310)$ system was seen to differ from the structure predicted by CSL theory by the removal of a plane of cations from the grain boundary core. A similar effect is suggested for the $\Sigma 13(510)$ system. The structure of the $\Sigma 5(310)$ boundary was also investigated by Mao et al. [75] using density functional theory with the predicted structure agreeing with experimental results by Dickey et al. [74]. Fisher and Matsubara [76] compared the structures and energies of the $\Sigma 5(310)$ and $\Sigma 13(320)$ systems using atomistic methods. Results suggested that the former was the most stable. Hojo et al. [77] used Z-contrast scanning electron microscopy and electron energy-loss spectroscopy to determine the atomic structure of the $\Sigma 5(210)$ grain boundary in CeO_2, it was found that a reduced oxygen density had the effect of stabilising this boundary. A similar study found that in contrast to the studies of other grain boundaries the atomic structure of the $\Sigma 3(111)$ system in CeO_2 is stoichiometric and does not promote the formation of oxygen vacancies [78].

Van Brutzel and Vincent-Abulant [79] used molecular dynamics to study how the presence

of grain boundaries can influence displacement cascades in UO_2. Six different grain boundaries were studied ($\Sigma5(310)$, $\Sigma13(510)$, $\Sigma25(710)$, $\Sigma41(910)$, $\Sigma29(\bar{7}\bar{3}0)$, $\Sigma17(\bar{5}\bar{3}0)$) and part of the investigation focused on the structures and formation energies of each boundary. $\Sigma5(310)$ had the lowest formation energy and the (n10) series of grain boundaries formation energy increased with the value of Σ apart from $\Sigma41$ which was the second most stable boundary. A general trend showed that higher misorientation angles correlated with higher formation energies except in the case of $\Sigma5(310)$.

In the case of YSZ it has been suggested that the segregation of point defects will have an impact on the conductivity of both the bulk and boundaries [80]. Sutton and Balluffi [81] suggested that the excess free volume at the grain boundaries would cause large cationic defects such as yttria to segregate to these regions in order to reduce elastic strain energy. Shibata et al. [82] investigated the structure and energy of nine different [110] grain boundaries in YSZ. They observed that local grain boundary structure in YSZ was responsible for the differences in grain boundary energies and the degree of solute segregation. However no link was seen between free volume and cation segregation. Instead they suggested that the degree of cation segregation was dependent on the amount of coordination-deficient cations present at the boundary. Other grain boundary studies in UO_2 have centred around transport properties, particularly fission gas and self diffusion, a discussion of which can be found in section 1.4.

1.3.2.3 Twist Grain Boundaries

Twist grain boundaries are defined as having an angle of rotation that is perpendicular to the grain boundary plane. Twist boundaries have received considerably less attention than tilt boundaries, particularly in the case of UO_2 and other fluorite type structures where very little literature exists. There has however been a more significant amount of work devoted to twist boundaries in rock salt structured materials such as MgO and it is from these studies that much of what is known about twist systems is derived.

Early simulation work focused on the determination of stable grain boundary structures for simple MgO twist boundaries [83, 84]. These early simulations suggested that the [001] twist boundary was unstable even though it had been observed experimentally [85]. It was later found that the disagreement between theory and experiment could be resolved by

reducing the density of ions at the grain boundary interface in the simulations and in order to find the most stable configuration it is necessary to minimise the system at different densities at the interface [86, 87]. A similar result was reported by Duffy [57]. When investigating the [011] twist boundary, she found that whilst this system is stable in its full density state the energy of the system can also be reduced by reducing the density of ions at the boundary interface.

There have been relatively few studies relating to the behaviour of twist boundaries in UO_2. Nerikar et al. [69] used yttria stabilised zirconia as a model to study the structure and stability of the $\Sigma 5\,(001)$ twist boundary in comparison to low Σ tilt boundaries. Twist boundaries were included in another study on the effect of boundary type on the segregation of fission gases to the boundary interface in UO_2 [88]. Other investigations characterising the effect of twist boundary systems in UO_2 looked at the role of twist grain boundaries in stress induced phase transformations [89]. Potentially more useful in the context of this current study is an investigation into their effects on ionic conductivity in YSZ by Fisher and Matsubara [76]. They found that twist boundaries have an enhancing effect on ionic conductivity in yttria stabilised zirconia in contrast to tilt boundaries in the same material which have no effect. It was suggested that the tilt grain boundaries trap oxygen vacancies unlike the twist system which may account for the difference in ionic conductivity

1.4 Transport Properties of UO_2

The transport properties of UO_2 are of interest at all stages in the life cycle of nuclear fuel materials including manufacture, reactor operation and long term storage [90]. Transport properties are relevant not just to self diffusion of uranium and oxygen atoms within the fluorite lattice but also to the transport of the various impurities and fission gases present in nuclear fuel samples.

1.4.1 Self Diffusion

The rate of cation diffusion within nuclear materials has been linked to the grain growth, diffusional creep and sintering as well as the formation and behaviour of fission gas bubbles [91]. As mentioned previously oxygen transport has particular importance in relation

to the safe operation of nuclear fuels, as inhomogeneous oxide distribution is related to lowering thermal conductivity and melting point as well as altering local burn up [92, 93]. Variations in the relative distribution of anions can also have a bearing on the materials thermo-chemical properties as well as altering the chemical states of fission products.

The transport of oxygen through UO_2 is not a new area of research, many studies have been conducted over the years using a range of techniques. In 1957 Aronson et al. [94] investigated the oxidation of UO_2 to U_3O_8 finding that it occurred via a two-step reaction. They also identified that the controlling factor in the initial stage of this oxidation was the diffusion of oxygen through the UO_2 lattice. Following on from this Auskern and Belle [95] investigated oxygen transport in both hyper-stoichiometric and stoichiometric UO_2 using an isotropic exchange method where ^{18}O in a gas exchanges with the ^{16}O of the sample. They concluded that oxygen diffusion in hyper-stoichiometric UO_2 was faster than that in stoichiometric UO_2 and proposed an interstitialcy mechanism for diffusion for the latter.

Very little experimental data has been reported on high temperature oxygen diffusion in UO_2, this is due in part to the inherent safety problems associated with experimental work involving radioactive materials. Computational methods allow a safer and more convenient way to study the transport effects in UO_2 and to date a number of studies have been published in this vein. Kupryazhkin et al. [96] used molecular dynamics simulations to investigate both oxygen and uranium diffusion in nanocrystals, determining diffusion coefficients and activation energies in the bulk, surface and near surface regions of the nanocrystals for temperatures ranging from 2280 K to 3950 K.

As well as looking at diffusion some molecular dynamics studies have also been performed to investigate physiochemical properties like heat capacity and thermal conductivity such as the study by Kurosaki et al. [97]. Morelon et al. [40] developed a new interatomic potential specifically fitted to simulate defect formation and migration energies. Quantum mechanical techniques have also been used to investigate transport properties in UO_2. Dorado et al. [90] used density functional theory to calculate activation energies of diffusion predicting an interstitialcy mechanism to dominate which agreed with inferences from earlier experimental work [95].

Sabioni et al. [98] investigated both oxygen and uranium diffusion in UO_2 grain boundaries between of 1498 °C and 1697 °C for uranium and 605 °C and 750 °C for oxygen diffusion.

This was achieved by comparing ionic transport properties of both mono and polycrystalline systems. It was suggested that diffusion of uranium at the boundaries was five orders of magnitude higher than in the bulk while oxygen diffusion was unaffected by the presence of grain boundaries. This result agreed with previous work by Marin and Contamin [99] who investigated oxygen transport using ^{18}O tracer diffusion. In this study single crystals and sinters displayed diffusion coefficients that were similar within experimental scatter. It was also noted that no enrichment of ^{18}O could be verified at the grain boundaries.

However, more recently Vincent-Abulant et al. [100] used molecular dynamics techniques to study diffusion in the stoichiometric UO_2 grain boundaries $\Sigma 5$ and $\Sigma 41$ over a larger range of temperatures and found that the presence of boundaries greatly enhanced diffusion of both uranium and oxygen in a region up to several nanometers from the grain boundary interface. Additionally this study predicted that diffusion of oxygen at the boundary was directionally dependant with a hopping mechanism observed at the interface. Arima et al. [101] also supported the idea that oxygen diffusion was enhanced in the grain boundaries and also predicted that the diffusion coefficient at the boundaries was influenced by grain boundary structure and misorientation angle. Also predicted in this study was the existence of three different regions of diffusion within UO_2 each characterised by a different mechanism.

Oxidation of nuclear fuels is also relevant with respect to water as if uranium is exposed to water, adsorption can occur at the surface with the result being that hydrogen is formed as part of the oxidation process [58]. Formation of pyrophoric UH_3 ensues. Under exposure to open atmosphere the formation of UH_3 is an intermediate to the formation of UO_2 with the hydrogen being recycled. If uranium is stored in a sealed container all available oxygen from water vapour and the air is consumed through oxidation. Hydrogen gas released as a result of oxidation can permeate through the layer of uranium oxide reacting to form UH_3 with the metal underneath. This system is stable in the absence of oxygen. However a dangerous reaction is likely to ensue if it is then exposed to oxygen, for example if a storage container was opened [102, 103]. This behaviour underlines the importance of being able to understand and predict the structure and diffusion properties of UO_2.

1.4.2 Helium Transport

Fission gas release in UO_2 has seen extensive study over the years. Fission gases such as helium are produced by the radioactive decay of actinides. The importance of understanding the transport behaviour of helium in UO_2 is related to safety through all phases of a fuel's life cycle. Radiation damage and the associated release of helium can cause changes in the microstructure of UO_2 which can result in radionuclide release [104].

The diffusion coefficients and solubility of helium in UO_2 have been investigated previously over a range of temperatures. The first such investigation was by Bostrom [105] looking at temperatures below $1000°C$. This was then followed by Rufeh et al. [106] and Sung [107]. All three investigations were undertaken by infusing helium into solid UO_2. Similar investigations were performed by Guilbert et al. [108] and Roudil et al. [104], however these two studies were carried out using the technique of ion implantation. Results for powdered UO_2 obtained by Roudil [104] at temperatures lower than $1000°C$ measured a diffusion coefficient one or two orders of magnitude higher than those of Bostrum over the same range of temperatures [109].

More recently an investigation by Ronchi and Hiernaut [110] measured diffusion of helium produced homogeneously by the α-decay of a ^{238}Pu dopant within the bulk. By using this method Ronchi and Hiernaut were able to investigate concentrations of helium significantly higher than the saturation level. Diffusion coefficients measured in this investigation were 3 or 4 orders of magnitude higher than measurements from previous studies. The activation energy of diffusion determined in this investigation was 2.6eV which generally agrees with previous studies [109].

The solubility of helium and indeed other fission gases in UO_2 is extremely low and as a result fission gas release tends to lead to bubble formation [111]. This low solubility causes helium to accumulate in bubbles within fuel grains and spaces between the grains of fuel, resulting in swelling of the fuel matrix [110, 112–115]. The size of these intragranular bubbles increases and their numbers decrease as the fuel is further irradiated these eventually evolve into elongated pores causing the bubbles to come into contact with the grain boundaries. The results of this is that continuous pathways can develop that assists the venting of fission gases [116]. Helium at the grain boundary interface is seen to diffuse very quickly to the point where grain boundaries can almost be considered as free surfaces [117]. Similarly

to what has been observed for oxygen diffusion in the region around the grain boundaries, helium diffusion is also enhanced in the near vicinity of these interfaces albeit at lower temperatures. No similar effect has been observed for other micro-structural defects such as pores and fractures.

1.5 Aims of Thesis

Whilst significant literature exists relating to the areas of defect and transport properties in UO_2, there are a number of gaps. The first of these areas relates to the precise effect of different grain boundaries on the diffusion of oxygen in polycrystalline UO_2. The second is the effect grain boundaries and surfaces have on the sequestration, transport and release of helium in UO_2. The aims of this thesis include:

- Derivation and validation of a robust potential model to build and investigate transport properties of grain boundary systems in UO_2. This potential must accurately represent the experimental structure and elastic properties allowing the modelling of stress on the crystal at high temperatures. Good representation of both defect and surface energies particularly oxygen Frenkel and migration energies are essential. This should be extended to include a new helium potential stable at high temperatures which accurately represents defect and migration energies in both stoichiometric and defective UO_2.

- Investigation into the implications of grain boundary type and structure on the diffusion of oxygen in polycrystalline UO_2 using the newly derived potential. We will incorporate a range of tilt and twist grain boundaries into this study and in each case paying particular attention to developing methods to generate different boundaries efficiently in a controlled manner and subsequently using models to investigate stability and effect on oxygen diffusion. Any observed dependence of oxygen diffusion on structure will have important implications for using modelling to relate the properties of individual grain boundaries to polycrystalline samples. We will use both energy minimisation and molecular dynamics to achieve this.

- Investigation into the sequestration, transport and release of helium from polycrystalline UO_2. Using previously developed grain boundary models we will look into the stability of helium interstitial defects in the bulk and at tilt boundaries paying particular focus to any potential variations in behaviour observed for different grain boundaries. We then intend to look at the influence of temperature on these defective boundary systems, studying its effect on stability, segregation and transport. For the final part of this investigation we propose a preliminary study into a new type of interface to simulate where a grain boundary intersects an external grain surface.

Chapter 2

Computational Methodology

Computer modelling of atomic level processes requires a reliable description of the interaction between atoms. This can be achieved by using either quantum mechanical or potential models. Although quantum mechanical methods are now largely accurate, they are not suitable for modelling large configurations. Thus as our aim is to explore grain boundaries in UO_2 and their structure and behaviour we need to use potential models.

2.1 Potential Forms

The Born model of solids [118] is used as the basis for the potential based approach utilised in this study. Using the Born model it is assumed that the sum of all interactions gives the total lattice energy (U):

$$U_{ij} = \sum_{ij} \frac{q_i q_j}{r_{ij}} + \sum_{ij} \phi_{ij}\left(r_{ij}\right) + \sum_{ijk} \phi_{ijk}\left(r_{ijk}\right) \ldots \tag{2.1}$$

where r_{ij} is the separation between ions i and j, the charge is represented by q. Short range interactions are represented by the second and third terms whereas the long range electrostatic interactions are accounted for by the first term.

2.1.1 onge Range Interactions

Long range interactions account for the electrostatic contribution to the lattice energy. As shown in equation 2.2.

$$U = \sum_{ij} \frac{q_i q_j}{4\pi\varepsilon_0 r_{ij}} \tag{2.2}$$

The permittivity of a vacuum is given by ε_0. Ion charges are given by q_i and q_j. The $\frac{1}{r}$ term has the disadvantage of converging very slowly, for systems periodic in only two dimensions two summations (Ewald [119] and Parry [120]) can be used.

The Ewald summation method is used to model three dimensional systems and divides the coulombic interaction into three parts. A term in reciprocal space φ_1, one in real space φ_2 and one representing self-interaction φ_3. By splitting the long range interaction into three terms, faster convergence can be achieved. These components when summed give the overall Coulombic interaction.

$$\varphi = \varphi_1 + \varphi_2 + \varphi_3 \tag{2.3}$$

The Parry summation is particularly useful when modelling surfaces and other systems with two dimensional periodicity. Crystals modelled using the Parry summation are treated as consisting of a number of infinitely sized charged planes instead of an infinite lattice as is the case for the Ewald Summation.

2.1.2 Short Range Interactions

In order to describe short range forces a number of different functional forms can be used utilising both attractive and repulsive terms. Repulsion is seen at very short distances between two atoms and is a result of the physical proximity of electron clouds. At longer distances attraction occurs and the effect of van der Waals interactions becomes more significant. The different forms of short range interactions are defined in this section.

2.1.2.1 Lennard Jones Potential

The Lennard-Jones potential takes the form of:

$$U(r_{ij}) = \frac{A_{ij}}{r_{ij}^{12}} - \frac{B_{ij}}{r_{ij}^{6}} \tag{2.4}$$

Repulsive forces are described by the first term which dominates at very short distances due to r_{ij}^{-12}. The second term describes attractive van der Waals dispersion forces. The parameters A and B can be modified so as to depend on more intuitive parameters.

$$A_{ij} = \varepsilon r_m^{12} \tag{2.5}$$

$$B_{ij} = 2\varepsilon r_m^{6} \tag{2.6}$$

Where, r_m refers to the ion separation at the minimum of the energy well and ε describes the depth of the energy well.

2.1.2.2 Buckingham Potential

Similar to the Lennard-Jones approximation the first term of the Buckingham potential describes the repulsive forces the second represents van der Waals dispersion forces.

$$U(r_{ij}) = A_{ij} e^{\left(\frac{-r_{ij}}{\rho_{ij}}\right)} - \frac{C_{ij}}{r_{ij}^{6}} \tag{2.7}$$

Parameters A and ρ are related to the repulsion between the ions electronic charge clouds. This potential is used more frequently for modelling polar solids as its repulsive term is more flexible than the Lennard-Jones potential, because of its additional parameter.

2.1.2.3 Morse Potential

The Morse potential introduces a further parameter which relates to the curvature of the potential well.

$$U(r_{ij}) = D_{ij}\left(1 - e^{\left[-B_{ij}\left(r_{ij}-r_0\right)\right]}\right)^2 - D_{ij} \tag{2.8}$$

where r_0 is the ion separation at the minimum of the energy well, D_{ij} is the depth of the well and B_{ij} is related to the curvature of the slope of the potential energy well. Historically, this potential was used for covalent bonds, and these parameters were obtained from structural and spectroscopic data.

2.1.2.4 Morl Potential

In the Morl we use a soft Morse potential, to ensure that to ensure that the repulsion is strong enough at short distances we add a repulsive term from a Lennard-Jones potential

$$U(r_{ij}) = \left(D_{ij}\left(1 - e^{\left[-B_{ij}\left(r_{ij}-r_0\right)\right]}\right)^2 - D_{ij}\right) + \frac{A}{r^{12}} \tag{2.9}$$

2.1.2.5 Ionic Polarisation

Ionic polarisability can be modelled reliably using the shell model [121]. It is defined as the induction of a dipole in an ion's electron density when in contact with an asymmetric electric field. The shell model describes the atom by splitting it into two parts, a core of charge X representing the nucleus and core electrons and a shell containing all the valence electrons with no mass which surrounds the core with a charge of Y. A harmonic spring of constant K links the core and shell. The ions' position within a crystal lattice is described by the position of the core, while the position of the shell has no physical significance. Shell charge and spring constant are related to polarisability α by:

$$\alpha = \frac{Y^2}{K} \tag{2.10}$$

By using the shell model the interactions between the nucleus and the electron cloud can be calculated. A potential disadvantage with using the shell model for large systems is the increase in computation time required as a result of the inclusion of two new parameters. A diagram representing the shell model is shown in figure 2.1.

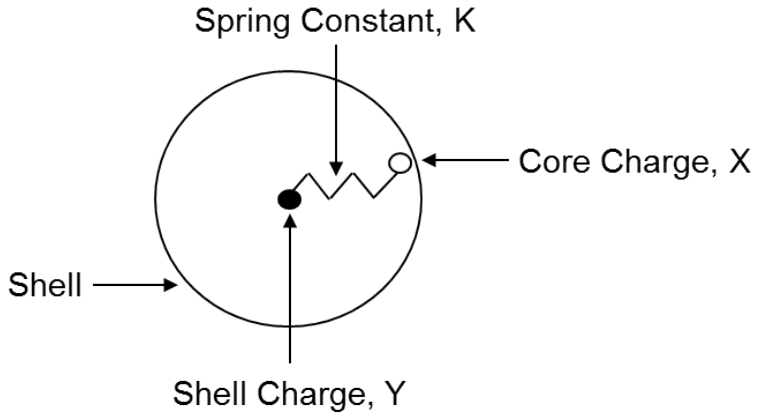

Figure 2.1: Shell Model

In our work we have a simpler treatment, which is to assume that the polarisability is independent of the environment around each atom.

2.1.3 Potential Derivation

2.1.3.1 Least Squares Method

Potentials specifically derived for use in this work were derived using the method of least squares fitting. The sum of squares can be defined as:

$$F = \sum w\,(f_{calcs} - f_{obs})^2 \tag{2.11}$$

where w is a weighting factor and f_{obs} andf_{calc} are the observed and calculated values. By fitting an attempt is made to minimise the sum of squares by altering the potential parameters. Fitting was done using GULP (General Utility Lattice Program) [122]. Potentials were fitted to reproduce experimental crystallographic data in an effort to develop models that will as accurately as possible reproduce these experimental data. In an ideal world the

sum of squares will equal zero however this is not always the case and the aim is to get as close to this as is possible.

2.2 Techniques

The work in this thesis employs two techniques for modelling structural and dynamic properties. These are energy minimisation and molecular dynamics.

2.2.1 Energy Minimisation

The lowest energy configuration of a structure is found by energy minimisation. A variety of suitable codes exist for modelling oxides using a potential model based strategy. Energy minimisation calculations were performed using the METADISE [123] and GULP [122] codes. In order to use this technique an initial structure is required. There are also two drawbacks first, temperature is neglected and secondly it is also possible that minimisation will cause a structure to find a local rather than global minimum.

In order to run an energy minimisation calculation one of two different approaches can be selected. Constant pressure minimisation allows both the cell dimensions and the ions to relax whereas constant volume allows only the ions to move and holds the cell parameters fixed. When all forces are equal to zero the system is considered to be at an energy minimum.

$$\frac{\delta U}{\delta_{r_i}} = 0 \tag{2.12}$$

where the change in energy is given by δU and the change in ion position is given by δr. So to give the bulk lattice strain Hooke's law is applied.

$$\varepsilon = C^{-1}\sigma \tag{2.13}$$

where C^{-1} is the second order derivative of lattice energy with respect to strain and σ is the stress, which is the sum of the static and applied pressure.

$$P_{static} = \left(\frac{1}{V}\right)\left(\frac{\delta U_L}{\delta \varepsilon}\right) \tag{2.14}$$

Two iterative techniques are applied in order to perform minimisations. These are conjugate gradient and Newton-Raphson

2.2.1.1 Conjugate Gradient Minimisation

The conjugate gradient method [124] uses previous information on the force with each successive step to direct the minimisation. This method is an extension of the steepest descent method with new positions of the atoms being calculated by:

$$r_{n+1} = r_n - \alpha_n S_n \tag{2.15}$$

where S_n is the displacement vector, r_n is the position at iteration n, α_n is a numerical constant defined with iteration and g_n is the force.

$$S_n = -g_n \tag{2.16}$$

where

$$g_n = \frac{-\delta U}{\delta r_n} \tag{2.17}$$

This method is limited by the fact that each new displacement vector is orthogonal to the last but not to any values previous to that. The steepest descent is only followed for the initial iteration whereas from then on iterations calculate the displacement vector using information from previous gradients.

$$S_n = -g_n + \gamma_n S_{n-1} \tag{2.18}$$

$$\gamma_n = \frac{g_n^T g_n}{g_{n-1}^T g_{n-1}} \tag{2.19}$$

When S_n equals zero minimisation occurs. The transpose of the vector is represented by T. Conjugate gradient methods are more efficient than steepest descent methods.

2.2.1.2 Newton Raphson Minimisation

The Newton-Raphson method [125] includes the second derivative of energy with respect to displacement to estimate α in equation 2.15.

$$\frac{\delta U}{\delta r} = g = kr \tag{2.20}$$

Then

$$W_{ij} = \frac{\delta^2 U}{\delta r^2} \tag{2.21}$$

As **k** is a second derivative matrix, it is represented above by W_{ij} which describes the stiffness of the bond between atoms i and j.

$$g_n(r) = W_{ij}\,(r_{n+1} - r_n) \tag{2.22}$$

where r_{n+1} is the position at iteration n.

$$r_{n+1} = r_n - \left(W_{ij}^{-1}\right)^n g_n \tag{2.23}$$

Fewer iterations are generally required by the Newton-Raphson method than the gradient method. However this is not to say that Newton-Raphson is faster as the inversion of W_{ij} is computationally very expensive. Often evaluation of an approximate minimum is found using conjugate gradient methods and then Newton-Raphson is applied to increase the chances of finding the global minimum.

2.2.1.3 BFGS

BFGS (Broyden-Fletcher-Goldfarb-Shanno) is a quasi-Newton technique. It approximates W^{-1} at each step instead of calculating it. W^{-1} is however only at set intervals or if a large change in energy occurs rendering the approximated value invalid. To approximate W^{-1}, forces, strains and the previous approximate value are required. BFGS converge faster than Newton-Raphson but it does however require more iterations to complete a minimisation.

One approach that allows us to include the effect of temperature explicitly is molecular dynamics.

2.2.2 Molecular Dynamics

Molecular dynamics can be defined as a method of solving Newton's Laws of motion over a finite time period. By assigning all particles in a system with a velocity, molecular dynamics includes kinetic energy. This can often enable a system to find a global minimum that would otherwise be unattainable due to energy barriers. However due to the small time frames which molecular dynamics can model, atoms are generally only able to overcome small energy barriers in the order of $k_B T$.

$$a = \frac{F}{m} \tag{2.24}$$

F is the force, m is mass and a is acceleration. The same method is used to calculate the forces on each atom as in energy minimisation. It is also possible to calculate new velocities and positions over a very small time step if the acceleration is known.

$$v_i(t+\delta t) = v_i(t) + a_i(t)\,\delta t \tag{2.25}$$

$$r_i(t+\delta t) = r_i(t) + a_i\frac{\delta t^2}{2} \tag{2.26}$$

r_i and v_i are the new position and velocity respectively. These equations are relevant for a very small time step and as a result finite time step algorithms are applied to prevent errors that occur as a result of time steps that are not infinitely small.

2.2.2.1 Integration Algorithms

In order to update the velocities and positions of ions at a finite time step integration algorithms are used. Molecular dynamics codes evaluate the evolution of a system by using a Taylor expansion.

$$r_i(t+\delta t) = r(t) + v(t)\,\delta t + \frac{1}{2}a(t)\,\delta t^2 \frac{1}{6}b(t)\,\delta t^3 + ... \tag{2.27}$$

$$v(t+\delta t) = v(t) + a(t)\,\delta t + \frac{1}{2}b(t)\,\delta t^2 + ... \tag{2.28}$$

$$a(t+\delta t) = a(t) + b(t)\,\delta t + ... \tag{2.29}$$

$$b(t+\delta t) = b(t) + ... \tag{2.30}$$

where a is the acceleration, v is the velocity, r is the position and b is the third derivative of r with respect to time. The Verlet algorithm [126] is widely utilised by molecular dynamics codes due to its simplicity. Third order Taylor expansions of ion positions at time t and the previous step $t-\delta t$ are used.

$$r(t+\delta t) = r(t) + v(t)\,\delta t + \frac{1}{2}a(t)\,\delta t^2 + \frac{1}{6}b(t)\,\delta t^3 + \theta\left(\delta t^4\right) \tag{2.31}$$

$$r(t-\delta t) = 2r(t) - v(t)\,\delta t + \frac{1}{2}a(t)\,\delta t^2 - \frac{1}{6}b(t)\,\delta t^3 + \theta\left(\delta t^4\right) \tag{2.32}$$

where the order of accuracy is given by θ. In order to determine atom positions these equations can be added together.

$$r(t+\delta t) = 2r(t) - r(t-\delta t) + a(t)\,\delta t^2 + \theta\left(\delta t^2\right) \tag{2.33}$$

While the Verlet algorithm does not calculate velocity as this is not required to determine ion trajectories, it can however be used to estimate velocities.

$$v(t) = \frac{r(t+\delta t) - r(t-\delta t)}{2\delta t} + \theta\left(\delta t^4\right) \tag{2.34}$$

The major disadvantage of the Verlet algorithm is that velocities cannot be computed until ion positions have been determined. The Verlet Leapfrog [127] algorithm is an alternative which calculates velocities at half integer time steps and calculates new ion positions from them. It is this algorithm that is utilised by the DL_POLY Classic code.

$$v\left(t+\frac{1}{2}\delta t\right) = \frac{r(t+\delta t) - r(t)}{\delta t} \tag{2.35}$$

$$v\left(t-\frac{1}{2}\delta t\right) = \frac{r(t) - r(t-\delta t)}{\delta t} \tag{2.36}$$

By using these expressions another equation to determine the new positions of the ions can be formulated using the velocities at the half integer time step and the old positions.

$$r(t+\delta t) = r(t) + v\left(t+\frac{1}{2}\delta t\right)\delta t + \theta\left(\delta t^4\right) \tag{2.37}$$

The main disadvantage with this method is the positions and velocities of the ions are not calculated simultaneously, so potential and kinetic energy contributions to the total energy cannot be calculated at the same time. The accuracy of calculated velocities are of the order δt^3 compared with δt^4 for the Verlet algorithm.

Information from the previous time step is required in both algorithms and therefore when a simulation begins initial velocities need to be assigned. This is done at random, but consistent with the required temperature and ensuring that there is no translational movement of the simulation cell. This is demonstrated by equations 2.38 and 2.39.

$$\Sigma_{i-1}^{N} m v^2 = 3Nk_BT \tag{2.38}$$

$$\Sigma_{i=1}^{N} mv = 0 \tag{2.39}$$

where the number of particles is given by N and k_B is the Boltzmann constant.

2.2.2.2 Time Step and Equilibrium

In molecular dynamics simulations it is essential that the appropriate time step is used. If the time step is too small then the simulations take too much cpu time to reach a meaningful amount of real time that longer time steps would. Too long a time step means the atoms move unphysical distances with the end result being failure of the simulation. In this work I have used two different time steps depending on the potential type being used in a simulation. For the partially charged potentials a time step of $1x10^{-15}$ seconds was used, whereas for the shell model potentials $2x10^{-16}$ seconds is usually employed. Shell model potentials require a slightly shorter time step as the shells are given a small mass and hence require a very small amount of time to relax.

In order to allow the system being simulated to reach equilibrium at the stated pressure and temperature the initial stage of the simulation is given up to an equilibration period. This equilibration period normally comprises tens of thousands of steps.

2.2.2.3 Ensembles

An ensemble is the name given to the conditions of a molecular dynamics simulation. There are three main types of ensemble which are discussed in this section.

The microcanonical ensemble or NVE, holds the volume, total energy and number of particles constant. The Hamiltonian, H is given by

$$H_{NVE} = U + K.E. \tag{2.40}$$

The canonical ensemble, NVT keeps constant the number of particles as well as the volume and temperature of the system. This study uses a Nosé-Hoover [128] thermostat to keep the

temperature constant. This thermostat algorithm alters Newton's equations of motion with the addition of a friction coefficient, x.

$$\frac{\delta x(t)}{\delta t} = \frac{N_f k_B}{Q}\left(T(t) - T_{ext}\right) \tag{2.41}$$

The number of degrees of freedom in the system is given by N_f and T_{ext} and $T(t)$ are the heat bath and instantaneous temperatures respectively. Q is the effective mass of the thermostat which is represented in equation 3.33.

$$Q = f k_B T_{ext} \tau_T^2 \tag{2.42}$$

where the specified time constant is given by τ_T. The initial prediction of $v(t)$ and T in the DL_POLY code are calculated using the Verlet Leapfrog algorithm. The conserved quantity for this system is derived from the extended Hamiltonian.

$$H_{NVT} = U + K.E. + \frac{1}{2}Qx(t)^2 + \frac{Q}{\tau_t^2}\int_0^{\tau} x(s)\,\delta s \tag{2.43}$$

NPT or the isobaric-isothermal ensemble holds constant the pressure and temperature as well as the number of particles under either isotropic or anisotropic conditions. The shape of the cell is allowed to change under anisotropic conditions. In this work the Melchionna [129] modification of the Hoover algorithm was used which uses a similar algorithm to before using a Nosé-Hoover thermostat and barostat.

2.2.2.4 Properties

Molecular dynamics can be used to calculate a range of properties. Shown in equation 2.44 is the formula representing the configuration energy of a system.

$$U = \left\langle \Sigma_{i=1}^{N} \Sigma_{\substack{j=1 \\ j\neq 1}}^{N} U\left(r_{ij}\right) \right\rangle \tag{2.44}$$

The distribution of particles relative to one another is described by the radial distribution function. Expression 2.45 describes how to determine the RDF for a single type of atom.

$$g(r) = \frac{1}{N^2} \left\langle \sum_{i,j=1}^{N} \delta(r - r_{ij}) \right\rangle \tag{2.45}$$

Mean Square displacements can be calculated as shown in equation 2.46.

$$2Dt = \frac{1}{3} \left\langle |r_i(t) - r_i(0)|^2 \right\rangle \tag{2.46}$$

From the mean square displacement diffusion coefficients can in turn be calculated either in the directions parallel to the grain boundary interface or perpendicular to it as a function of distance. Diffusion coefficients were determined by dividing the simulation cell into segments in the X direction and calculating the X, Y and Z (Dx,Dy, Dz) components of diffusion in each segment [130, 131].

$$D_x(x) = \frac{\lim_{t\to\infty} \left\langle [x(t) - x(0)]^2 \right\rangle}{2t} \tag{2.47}$$

$$D_y(x) = \frac{\lim_{t\to\infty} \left\langle [y(t) - y(0)]^2 \right\rangle}{2t} \tag{2.48}$$

$$D_z(x) = \frac{\lim_{t\to\infty} \left\langle [z(t) - z(0)]^2 \right\rangle}{2t} \tag{2.49}$$

We consider the trajectory of a particle, correlating its initial position $z(0)$ with its final position $z(t)$ and assign the trajectory to segment of the system in which the particle resided at $z(0)$. To do this we must define two essential parameters, the segment width and correlation time. Therefore for each system we need to adjust both in order to ensure the results are converged. This approach has recently been used Crabtree et al. [132] to investigate transport and adsorption on zeolite surfaces.

2.2.3 Periodic Boundary Conditions

In order to simulate a system of infinite size but using only a finite number of images, periodic boundary conditions are used. The simulation cell is surrounded by images of itself, effectively reproducing the unit cell in three dimensions. Simultaneous identical movement of the particles in each cell enables a much larger system to be simulated than would normally be allowed by the computing power available. By utilising boundary conditions the efficient convergence of the coulombic interactions is enabled. When generating surfaces, two dimensional periodic boundary conditions are used effectively making the simulation infinite in two dimensions. When using two dimensional periodic boundary conditions the Parry summation is applied as opposed to three dimensional boundary conditions which use the Ewald summation (Section 2.1.1).

2.3 Simulation of Defects

2.3.1 Point Defects

A further procedure developed in this work is where we automatically scan point defects as a function of position in a crystal or interface. To model point defects the Mott-Littleton method [133] is used which gives the energy to form a defect at infinite dilution. This approach involves dividing the crystal lattice into two regions centred on the point defect. Region I contains the point defect, during minimisation all ions in this region are relaxed explicitly. Region II is split into a further two regions; region IIa and region IIb. Region IIb is the outer region which extends to infinity and as a result the forces are weaker. The ions in this region are not displaced but experience only a dielectric effect resulting from the charge of the defect. The ions in region IIa are relaxed harmonically as a result of forces from the point defect or all the atoms in region I. In equation 2.50 three terms are used to calculated the total system energy (U)

$$U(x,y) = U_1(x) + U_2(xy) + U_3(y) \tag{2.50}$$

where the energy of region 1 is given by $U_1(x)$, the interaction between regions 1 and 2 is given by $U_2(xy)$ and the total energy of the rest of the crystal is given by $U_3(y)$. The

coordinates of the ions in regions I and II are represented as the vectors x and y. In order to calculate long range coulombic interactions extending into region II, a continuum approximation is used. Here the displacements are as a result of the total charge of the defect at the defect origin. Equation 2.51 shows how polarisation (P) can be calculated as a function of distance (r) where ε_0 designates the static dielectric constant . This results in a $\frac{1}{r^4}$ contribution to the energy, which decreases with the increasing size of region I.

$$P = \frac{1}{4\pi}\left(1 - \frac{1}{\varepsilon_0}\right)\frac{Z_e r}{r^3} \tag{2.51}$$

When running an energy minimisation simulation using the Mott-Littleton method the region sizes must be specified. To ensure convergence it is necessary to ensure region sizes are sufficiently large that increasing them does not cause a significant difference to defect energies. This approach has been widely adopted when investigating defects in UO_2 [38,49] and other materials [134, 135].

2.3.2 Surfaces

In order to produce surfaces, bulk crystals are cut along Miller indices. By cutting the bulk crystal along different planes, various different surfaces can be produced, which display different stabilities. Bertaut [136] showed that the energy of the surface will diverge to infinity if a dipole moment perpendicular to the surface is present. Tasker [137] defined three different types of surfaces that can be generated as a result of cleaving the crystal along different planes.

The type I surface consists of neutral planes where each plane consists of the stoichiometric composition. The crystal is generated by adding multiple layers of these planes. The type II surface is made up of symmetrically stacked charged planes however, as multiple planes are present there is no net dipole moment. A type III surface is made of asymmetrically stacked charged planes with a dipole moment perpendicular to the surface. This net dipole moment has the effect of making type three surfaces completely unstable unlike type one and two surfaces. If half the surface ions are repositioned at the bottom of the cell the result is the cancelling of the dipole moment [138]. This process is analogous to the micro-faceting of surfaces observed in naturally occurring minerals.

By using Tasker's approach to modelling surfaces a complete crystal is made up of a large amount of charged planes. This can cause problems as it can be expensive in terms of computer time. The two region approach [137] was a method designed to overcome this problem. It involves simulating the surface as two blocks made up of two distinct regions. Region I is the crystal region close to the surface and region II is the crystal region that is more distant. It is often required to run a set of simulations to determine the optimum region size. Regions that are too small will not relax fully and therefore give an incorrect energy, whereas if the region is too large it will be computationally expensive.

The ions comprising region 2 are held fixed at bulk equilibrium positions whereas the region 1 ions are allowed to relax. A surface calculation is performed utilising a single block with the surface present at the top of region one. Bulk calculations are run using two blocks and positioned so that the region 1's of the two crystals are adjacent. The block energies can be calculated by adding together the interactions of the various regions. The surface energy (U_S) and bulk energy(U_B) are determined by equations 2.52 and 2.53.

$$U_B = \left(E^B_{I-I} + E^B_{I-II}\right) + \left(E^B_{II-I} + E^B_{II-II}\right) \tag{2.52}$$

$$U_S = \left(E^S_{I-I} + E^S_{I-II}\right) + \left(E^S_{II-I} + E^S_{II-II}\right) \tag{2.53}$$

The superscripts ^{S} and ^{B} refer to surface and bulk respectively. E_{II-I} represents the energy of ions from region two interacting with ions from region one and E_{I-I} represents the energy of ions from region one interacting with ions from region one. The difference in energy between the bulk system and the surface system for the same number of atoms per unit area is defined as the surface energy:

$$\gamma = \frac{U_S - U_B}{S} \tag{2.54}$$

where S is the surface area. As a consequence to save computational time we assume $E^B_{II-II} = E^S_{II-II}$ and hence their calculation is not required.

2.3.3 Crystal Morphologies

The METADISE code predicts equilibrium morphologies by using surface energy calculations. This was based on work by Gibbs [139], who stated that for a crystal of given volume, the equilibrium form will have the lowest surface energy.

$$\gamma = \Sigma_i \gamma_i S_i \tag{2.55}$$

where S_i and γ_i are the area of the i^{th} crystallographic face and the surface energy respectively. Research by Wulff [140] indicated crystal morphology would be dependent on the surface energy of a particular face (γ_i) being proportional to the normal vector to the face (h_i).

$$h_i = \lambda \gamma_i \tag{2.56}$$

The term λ represents a constant which is dependent on crystal size. Therefore it is expected that for a crystal grown under equilibrium conditions and without taking into account kinetic factors such as growth rate that high energy surfaces will not be observed.

2.3.4 Grain Boundaries

Grain boundaries are defined as the interface between two crystalline grains with different orientations [57]. In the next section a detailed description can be found of how to generate these interfaces.

2.3.4.1 Generating Tilt Boundaries

By mirroring block 1 with respect to block 2 a twin grain boundary interface can be created. Two mirrored surfaces with the same Miller index will create a system that is the same as the bulk, so it is necessary to apply a vector displacement perpendicular to the interface in order to create a shear plane. The interface is situated between the region I's of both block 1 and block 2, with all ions in both of these regions being allowed to relax. In the same way

as when generating surfaces the region II is used to simulate the bulk and all atoms within the region are kept fixed.

In order to find the most stable vector displacement a scan simulation is performed utilising the METADISE [123] code. An ideal net is constructed parallel to the interface with a mesh that can be changed depending on the intricacy of the structure being simulated. The scan is computationally expensive and the smaller the mesh the more demanding it will be. The energies calculated at each point can be represented using a hypersurface depicted along two structural coordinates. Once the optimum displacement has been determined, a full minimisation is performed to determine the energy of the grain boundary.

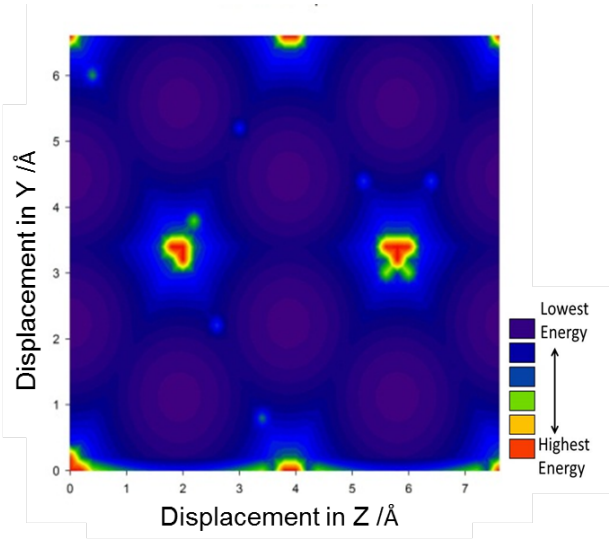

Figure 2.2: Grain boundary hypersurface produced by scanning the $\Sigma 3(111)$ grain boundary

The formation and cleavage energies can be used to express the stability of a grain boundary. The cleavage energy E_c, is defined as the energy required to completely separate the boundary into two surfaces. Formation energy E_f, is the energy needed to form the grain boundary from the bulk per unit area. Both are determined using the surface area A, energy of the structure containing the interface E_{gb}, the energy of the bulk containing the same number of atoms per unit area E_{bulk}, and energy of the system containing the structure with half the unit atoms per area E_{surf}.

$$E_f = \frac{E_{gb} - E_{bulk}}{A} \tag{2.57}$$

$$E_c = \frac{E_{gb} - 2E_{surf}}{A} \tag{2.58}$$

As crystals grow the chance of them coming together at different angles to form twist boundaries increases. In chapter 5 we focus on these more complex interfaces and discuss the methodology developed as part of this investigation to model these interfaces. Similarly in chapter 6 we discuss a further adaptation of tilt boundaries, the T-interface including an investigation of how to generate this new type of interface where a grain boundary intersects with the grain surface. However before describing the results on simulating grain boundaries the next chapter will discuss work on testing and ultimately deriving a new potential for UO_2.

Chapter 3

Potential Models

In this chapter we present the potential models that have been derived as part of this investigation. Bulk material properties including defect energies are evaluated for UO_2 using the newly derived potentials and where possible are compared with experimental results and previously reported simulations (including DFT). As noted in Chapter 1 we required a potential model that was computationally cheap, but can reliably model the structure, elastic and oxygen transport properties. Whilst the main focus is on simulations involving UO_2, potentials are also derived for ThO_2 and U_3O_8.

3.1 Potential Literature

In the case of UO_2 many different models have been derived over the years using varying functional forms to suit a broad range of purposes. All of these potentials are fitted with varying success to reproduce experimental data.

The first study utilising interatomic potentials was conducted by Benson et al. [141] to calculate the cohesive energy of a UO_2 crystal using a potential fitted to compressibility and lattice parameters. This was followed by four sets of potentials fitted to phonon dispersion curves derived by Dolling et al. [142]. Three of these potentials used the shell model [121] and the remaining one was based on a rigid ion model.

Tharmalingam [143] published the first sets of potentials derived to model point defect energies. Catlow [38, 144] developed potential models that not only reproduced the defect

energies but were able to explain the appearance of defect clusters. The shell model was not however, useful for modelling transport at high temperatures. Hence a rigid ion potential was developed by Walker and Catlow [145] fitted to structural parameters and the static dielectric constant for use in molecular dynamics simulations of UO_2 at high temperatures. Later Lewis and Catlow [146] produced a library of potentials for a range of different metal oxides all using the same oxygen-oxygen interaction with the aim being that a large number of different alloys could be investigated. The models were transferable because only one oxygen-oxygen potential was used. Three UO_2 potentials were mentioned in this paper, one of which was rigid ion and two were shell model based.

The models developed by Catlow [38] were modified by Jackson et al. [147] to use a Buckingham four range form in order to make the potential more robust at low interatomic distances. This potential was used to predict defect formation [39], activation and substitution energies as well as solution energies of fission products [148, 149]. Jackson also created a second potential with the aim of calculating dynamical properties, which saw use studying grain growth [66] and activation energies of oxygen diffusion [150]. Sindzingre and Gillan [151] calculated high temperature oxygen diffusion coefficients, melting point and thermal expansion utilising a new potential based on Jackson's anion - anion interaction derived with the intention of reducing the amount of time required to calculate dynamical properties. It was then further modified by Karakasidis and Lindan [152] to simulate the transition to the fast ionic diffusion regime.

Morelon [40] modified earlier work to produce a partially charged potential that very accurately reproduced defect energies. This potential model was used in the simulation of grain boundary diffusion [51, 100] and displacement cascades [153]. The shell model based potential by Grimes and Catlow [49] was also developed with the intention of modelling defects in UO_2. This potential saw extensive use in modelling the migration and solution energies of a large range of impurities [46, 48, 52, 154, 155].

Yamada et al. [156] used a partially charged rigid ion type model to investigate the thermal properties of UO_2. This potential was developed as part of a set using a consistent anion - anion interaction to investigate MOX fuels. Two rigid ion based potentials of a similar form to Yamada's were derived for UO_2 by Arima [157], one using a partially charged regime and the other using formal charges. These were subsequently used as the basis for calculating thermal properties and then modelling oxygen diffusion in grain boundary systems [101].

In the same year Meis and Chartier [158] investigated the thermodynamic properties of UO_2 using a new potential based on elastic, dielectric and crystallographic data.

For this investigation we needed a model that accurately reproduced the structure of UO_2 and its elastic constants to model heat transport and the effect of stress on the crystal. Combined with good representation of anion Frenkel defect energies and activation energies to model the oxygen transport correctly.

3.2 Potential Models Derived In This Study

3.2.1 UO_2 Morl Potential

New potential models were derived with the aim of being able to model a wide range of nuclear materials. To do this partially charged rigid ion potential models based on Morse potentials but with the addition of the repulsive term from a Lennard-Jones type potential as in Malavasi et al. [159] were employed. This type of potential will be referred to as the 'Morl potential' throughout. One of the key features of this model is that we wanted to use a partial charge model rather than a shell model as it was thought that it might model in part the effect of polarisation compared to a formally charged model without having the computational overhead of using the shell model. A second feature is that we chose to scale all charges by 60%. This way we can incorporate non-stoichiometry more easily and no charge adjustment is needed with change in composition. In addition such models exist and hence have parity for other oxides.

All of the potential models in this section utilise the same anion - anion interaction which is based on the work of Sayle et al. [160] who showed that this form originally designed for use in glasses gives good representation of fluorite structures by using it to model CeO_2. The potential models developed are rigid ion type models and as a result are relatively simple to compute allowing the study of large systems.

In the case of UO_2 the U-O interaction was derived specifically to reproduce the experimental lattice parameter of UO_2 [161] as well as elastic constants [162] and like all other potentials was derived using the GULP code [163] using the method described in chapter 2. Table 3.2.1 lists the potential parameters$D$, B, r_0 and A for each interaction. Also shown in

the table are parameters for ThO_2 which has often been suggested as an alternative nuclear fuel to UO_2. The structure of ThO_2 is also based on fluorite and lattice parameters differ only slightly from those of UO_2, but thorium exhibits only one oxidation state compared to the variable oxidation states seen for uranium [164]. A potential was derived for ThO_2 along similar lines to the UO_2 potential and utilising the same potential form and anion - anion parameters. This ThO_2 rigid ion potential was fitted in the same manner as UO_2 to experimental data quoted by Taylor [165] and Machedo [166].

The morl potential form has also been used to model non fluorite structures such as U_3O_8. This is the major oxidation product of UO_2 and one of the few higher oxides of uranium with well defined physical and crystallographic data. A potential was derived with the aim of in the future being able to model interfaces between UO_2 and U_3O_8. Similar to other potentials the anion-anion interaction is kept constant. However as U_3O_8 is not a fluorite structure the uranium partial charge is no longer 2.4. The partial charge ratio is however kept constant at 60%. There has been some disagreement as to the formal charges of uranium in U_3O_8. However, Ball et al. [33] used atomistic potentials to model U_3O_8 and in doing so looked at the effect of different suggested uranium charge states. It was found that by using an average charge on the uranium of +5.33 the closest fit to experimental results was observed. Therefore a partial uranium charge of +3.198 is employed here.

Table 3.1: Potential parameters for UO_2, ThO_2, U_3O_8, and CeO_2

Ion Pair	D/ eV	B/ Å	r_0/Å	A/ eV Å^{12}
$O^{-1.2}$- $O^{-1.2}$	0.04173	1.886824	3.189367	22
$U^{2.4}$ - $O^{-1.2}$	0.083352	1.946417	2.946396	1
$U^{3.198}$ - $O^{-1.2}$	0.083352	1.946417	2.946396	1
$Th^{2.4}$ - $O^{-1.2}$	0.011639	2.405891	3.201846	1
$Ce^{2.4}$ - $O^{-1.2}$	0.083352	1.946417	2.946396	1

3.3 Validation and Comparison

The potential models derived in this study were employed to calculate structural and diffusion properties of UO_2 using energy minimisation and molecular dynamics. Where possible

the calculated values were compared with results from experimental and other simulation work, which included experiments on polycrystalline samples [95, 99, 167, 168]. Results for UO_2 are compared to two other rigid ion potential models that have previously been used to simulate UO_2 grain boundaries (Σ5, Σ41, Σ13, Σ29) [100, 101]. Bulk properties of ThO_2 and U_3O_8 are also calculated using newly derived potentials and comparisons are made where data is available.

3.3.1 Structural Properties

Table 3.3.1 displays the experimental and predicted lattice (a_0) and elastic (C_{11},C_{12},C_{44}) constants as well as the bulk modulus (B) calculated using the morl potential in METADISE [123]. This is also compared with results predicted by Morelon et al. [40], Arima et al. [157], Catlow [38] and Grimes [169] .

Table 3.2: Experimental and predicted properties of UO_2 using the shell model based potentials of Catlow and Grimes and partial charged Morl, Morelon and Arima potential models.

Property	Exp	Morl	Morelon [40]	Arima [157]	Catlow [38]	Grimes [169]
a_0 /Å	5.4862 [1]	5.468	5.446	5.464	5.521	5.462
B /GPa	209.0 [162]	197.7	125.0	217.8	211.8	272.9
C_{11} /GPa	389.3 [162]	387.6	216.9	436.1	434.4	524.2
C_{12} /GPa	118.7 [162]	102.9	79.1	108.7	100.4	147.3
C_{44} /GPa	59.7 [162]	88.1	78.5	101.6	57.3	89.2

Structural properties are particularly well reproduced by all models but the significant improvement of the morl potential is in the elastic constants which relate to how the system responds to stress and as we intend to perform a number of relaxations at different temperatures it is essential that our model matches these values closely. This improvement is likely due to morl potential being fitted to elastic constants as well as the lattice parameter.

3.3.1.1 ThO_2

Bulk properties for ThO_2 were calculated using the partially charged Morl ThO_2 potential. Table 3.3 shows the experimental properties of ThO_2, compared with properties predicted by both the Morl potential and gas potentials from work by Colbourn [170].

Table 3.3: Experimental and predicted properties of ThO_2 using the partial charged Morl potential model and shell model based potential of Colbourn.

Property	Exp	Morl	Colbourn [170]
a_0 /Å	5.5974 [165]	5.595	5.598
B /GPa	193 [166]	199	258
C_{11} /GPa	367 [166]	359	495
C_{12} /GPa	106 [166]	119	139
C_{44} /GPa	79 [166]	95	63

The experimental structure of ThO_2 is reproduced to a high degree of accuracy. The elastic constants and bulk modulus are also reproduced successfully. It is clear that fitting the morl potential to these properties is offering a significant improvement when compared to other potential based work. This improvement is likely due to the fact that the morl potential model was fitted to reproduce these constants.

3.3.1.2 α-U_3O_8

Bulk properties for α-U_3O_8 were calculated using the partial charge α-U_3O_8 potential derived for this work. The parameters that describe this potential can be found in table 3.2.1. Table 3.4 shows the experimental properties of α-U_3O_8 compared with predicted properties and another set of properties derived using a potential calculated by Ball and Dickens [33].

Table 3.4: Experimental and predicted properties of α-U_3O_8 using the partial charged Morl potential model and shell model based potential of Ball and Dickens.

Property	Exp	Morl	Ball & Dickens [33]
a_0 /Å	4.15 [171]	4.16	4.14
b_0 /Å	11.96 [171]	11.88	12.06
c_0 /Å	6.72 [171]	6.86	6.96
B /GPa	-	332.8	310.9
C_{11} /GPa	-	424.0	373
C_{12} /GPa	-	287.2	279.8
C_{44} /GPa	-	66.91	57

The table shows good agreement between the partial charge potential and the experimental results. Compared to the Ball and Dickens potential the partial charge potential describes

the lattice vectors to a higher degree of accuracy. It is not possible to accurately compare the predicted elastic constants of the two potentials as no experimental elastic constants are available. However both potentials show some agreement to each other especially with respect to the C_{12} and C_{44}.

3.3.2 Point Defects

3.3.2.1 UO_2

In table 3.5 the formation energies for both anion and cation Frenkel as well as Schottky defects at infinite dilution are presented for all five UO_2 potentials, compared alongside experimental values. The equations for each of these defect types are displayed in equations 3.1-3.3.

$$O_O^x \rightarrow V_{\ddot{O}} + O_I^{''} \tag{3.1}$$

$$U_U^x \rightarrow V_U^{''''} + U_I^{\cdots} \tag{3.2}$$

$$2O_O^x + U_U^x \rightarrow 2V_{\ddot{O}} + V_U^{''''} + \mathrm{U}O_{2_{SURFACE}} \tag{3.3}$$

Defects were generated using GULP [122] and energies determined using the Mott-Littleton [133] method which is detailed in chapter 2. Also included in the table is the activation energy of oxygen migration which was calculated statically.

Table 3.5: Comparison of experimental and predicted defect and migration energies in UO_2 using shell model based potentials of Catlow and Grimes and partial charged Morl, Morelon and Arima potential models.

Property /eV	Exp	Morl	Morelon [40]	Arima [157]	Catlow [38]	Grimes [169]
E_a Vac Mig	0.5-0.6 [16]	0.6	0.3	0.3	0.3	0.7
E_f U Frenkel	4.8-6.3 [1]	10.3	6.3	10.4	8.4	12.1
E_f O Frenkel	1.6-2.7 [1]	3.4	1.6	3.6-3.8	2.6	3.5
E_f Schottky	2.0-2.3 [1]	5.2	2.2	2.5-3.0	2.5	4.5

The morl potential, as well as the Arima potential, generally overestimates all defect energies which is a slight disadvantage to using a rigid ion potential as it does not take into account ionic polarisability. However, the shell model based potential of Grimes does not reproduce defect energies particularly accurately. The Morelon potential was specifically derived to replicate these energies and is one of the few UO_2 potentials that predicts these values accurately. All potential models correctly predict the relative stabilities of the defects. The morl potential accurately reproduces the activation energy of oxygen vacancy migration. This migration path is the lowest energy and most favourable diffusion mechanism observed in bulk UO_2 [90]. The other potentials largely underestimate the experimental value. One particular disadvantage of the morl potential is its poor representation of cation Frenkel defects. While it is not the only potential with this problem it does mean that we cannot use it to reliably investigate uranium diffusion in UO_2.

3.3.2.2 ThO_2

The formation energies of defects in ThO_2 at infinite dilution are shown in table 3.11 alongside experimental data and values determined using other potential models.

Table 3.6: Comparison of defect and migration energies in ThO_2 predicted using both potential models and DFT.

Property	Morl /eV	Colbourn [170] /eV	QM [164] /eV
E_a Vac Mig /eV	0.7	0.8	1.3
E_f Th Frenkel /eV	11.0	9.9	-
E_f O Frenkel /eV	3.6	3.0	4.9
E_f Schottky /eV	5.5	4.0	6.7

By forming defect clusters a sizeable reduction in energy is apparent, however formation energies are still slightly higher than those calculated by Colbourn [170] using gas potentials but lower than the values determined by Yun et al.[22] using quantum mechanical techniques. Similarly to UO_2 the most stable defect type is the oxygen Frenkel defect. The activation energy for oxygen vacancy migration in ThO_2 predicted by the potential derived in this study is very close to the value determined by Colbourn et al. [170] but smaller than the value predicted using ab initio methods. No experimental data are available for comparison.

3.3.3 Surfaces

3.3.3.1 UO_2

Low Miller index surfaces were generated and minimised using the METADISE code [123]. A detailed description of the generation of these structures can be found in chapter 2. Relaxed surfaces were generated for the Morl Potential, Arima, and Morelon and the calculated energies were compared to Quantum Mechanical data by Abramowski [66]. These can be seen in table 3.7.

Table 3.7: Surface energies of UO_2 calculated using both shell and partial charge potential models compared with DFT values.

Surface	DFT [66]	Morl	Morelon [40]	Arima [157]	Catlow [38]	Grimes [169]
(111) /Jm^{-2}	0.46	1.33	0.91	0.92	0.92	1.47
(110) /Jm^{-2}	0.85	1.95	1.50	1.61	1.28	2.24
(100) /Jm^{-2}	1.19	2.69	1.77	2.14	1.53	3.01

All five potentials agreed with the quantum mechanical data regarding the relative order of stability. Significant variation is seen in predicted values for the different potentials, all of which overestimate energy values to some degree. Energies calculated using the Morl and Grimes potential were however higher and further from those determined quantum mechanically when compared to the results predicted by other potentials.

Morphologies were generated using the surface energies. For the morl potential both equilibrium and growth morphologies were generated and are displayed in figure 3.1.

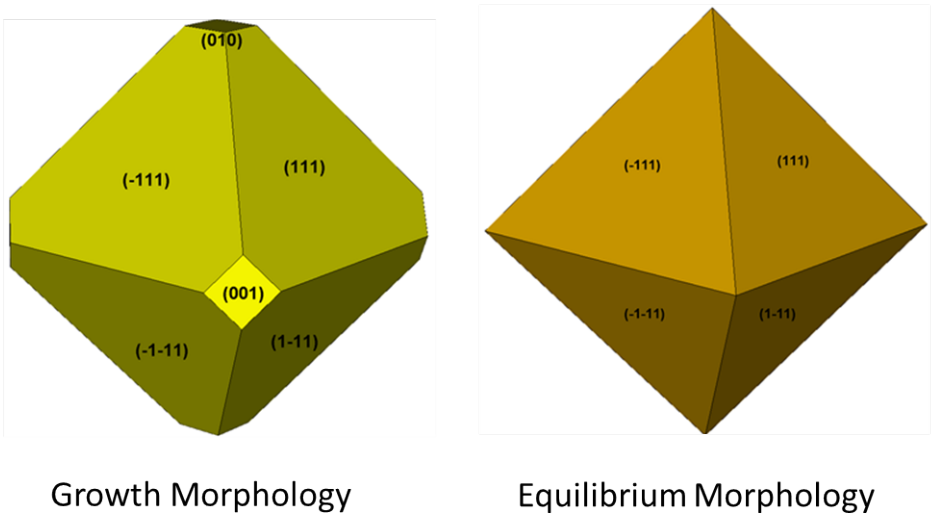

Figure 3.1: UO_2 morphologies generated using the morl potential

As would be expected morphologies generated using surfaces energies calculated by the morl potential predict an equilibrium morphology of an (111) terminated octahedron. This is in agreement with quantum mechanical simulations by Abramowski [66] who also predicted a (111) terminated octahedron. Using the Morl potential the growth morphology also produced a (111) terminated octahedron however unlike the equilibrium morphology the corners consisted of (100) facets. Abramowski also predicted that growth morphologies would take the form of a truncated octahedron consisting of (111) faces with (200) facet which as (100) and (200) surfaces are identical for fluorite structured materials shows good agreement with the partial charge potential.

3.3.3.2 ThO_2

The energies of the low Miller index surfaces in ThO_2 were calculated in the same way as for UO_2 and are listed in table 3.8 alongside surface energies obtained using quantum mechanical simulations by Skomurski et al. [68] for comparison.

Table 3.8: Surface energies of ThO_2 calculated using the morl ThO_2 potential model and compared to quantum mechanical data

Surface	QM / (J m^{-2}) [68]	Morl / (J m^{-2})
(111)	0.68	1.12
(110)	1.27	1.69
(100)	1.71	2.44

Results predicted the (111) surface to be the most stable, the (100) to be the least stable and the (110) to have a surface energy in-between the other two. The relative stabilities predicted using the partial charge potential agree with the quantum mechanical results but the energies calculated using potential methods were generally higher. This overall order of stability is in line with what was seen for UO_2 and is likely similar for most if not all fluorite type structures.

The equilibrium morphology consists of an octahedron terminated with (111) surfaces while the growth morphology consists of a truncated octahedron with (111) surfaces and (100) facets occupying the corners. No experimental morphologies exist for comparison but these structures mirror what was seen for UO_2 and as both exist as fluorite structures we can assume their morphologies will be similar. Morphologies for UO_2 are shown in figure 3.1.

3.3.3.3 α-U_3O_8

The stability of the low Miller index surfaces of U_3O_8 were investigated. Not all Miller index surfaces are shown as some possessed very large dipole moments.

Table 3.9: U_3O_8 low Miller index surface energies calculated using the morl α-U_3O_8 potential model

Surface	Morl / (J m^{-2})
(011)	1.67
(010)	1.67
(100)	2.30
(110)	2.32
(111)	2.56

The lowest energy surfaces are the (011) and (010) surfaces, both of which only display a slight relaxation. The (100), (110) and (111) surfaces are less stable and also exhibit

much greater relaxation. No experimental or quantum mechanical data are available for comparison.

3.3.4 Bulk Oxygen Transport

3.3.4.1 UO_2

Bulk systems were generated using METADISE [123] and were composed of a 4x4x4 UO_2 block of unit cells consisting of 768 atoms. Molecular dynamics simulations were run on stoichiometric bulk UO_2 and defective simulation cells containing 0% - 2% stoichiometric vacancies. Systems were initially heated using the NPT ensemble and from the resultant structure the final simulations were run using NVT. Each system was run with temperatures ranging from 2000 K-3900 K, at intervals of 100 K with each simulation running for a total of 2.1 ns made up of a 100 ps equilibration time and then 2ns time period over which diffusion data was calculated. Bulk diffusion data obtained for stoichiometric and defective bulk systems is compared with experimental data from Auskern [95], Marin [99], Hadari [167] and Sabioni [168] in figure 3.2.

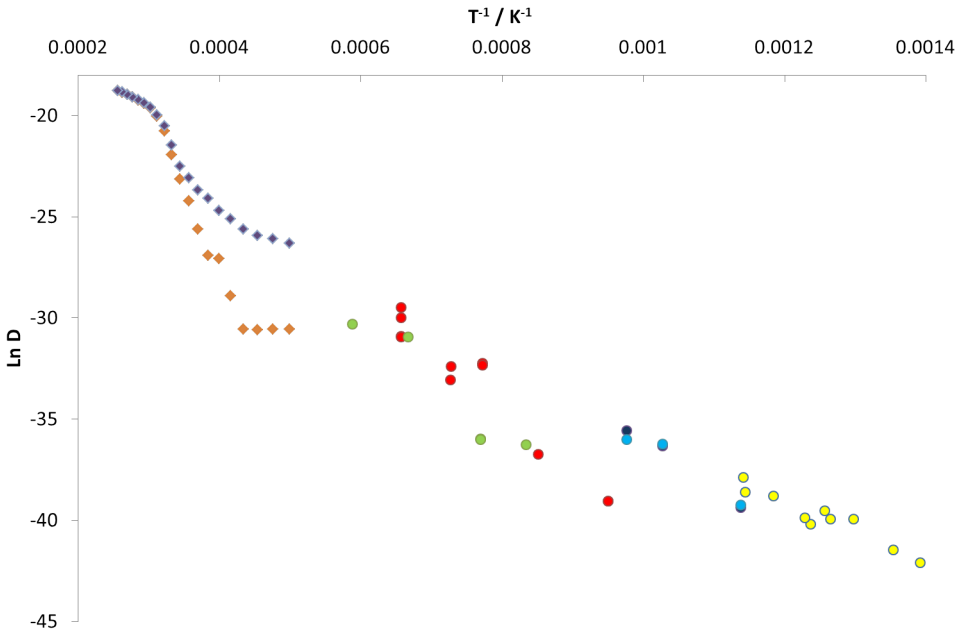

Figure 3.2: Diffusion data predicted using the UO_2 morl potential containing ◆ one Schottky defect and ◆ zero Schottky defects compared to experimental results by ● Sabioni [168], ● Auskern [95], ● Marin [99], ● Hadari [167] and ● Sabioni Polycrystalline [168].

The experimental studies show a general trend of increasing oxygen diffusion rates with temperature which is in line with the predicted results from the Morl potential. A direct comparison between calculated and experimental results is difficult as experiments were carried out at lower temperatures. However, due to the small time frame in which molecular dynamics is run, it is necessary for us to run simulations at high temperatures which enable us to gain sufficient data in a reasonable time frame and obtain meaningful statistics.

Figure 3.3 details the diffusion data using the new Morl potential derived for this investigation. Diffusion coefficients were calculated for systems with different numbers of vacancies ranging from 0% to 2% in order to determine the effect on diffusion. The system was kept charge neutral by removing both oxygen and uranium ions.

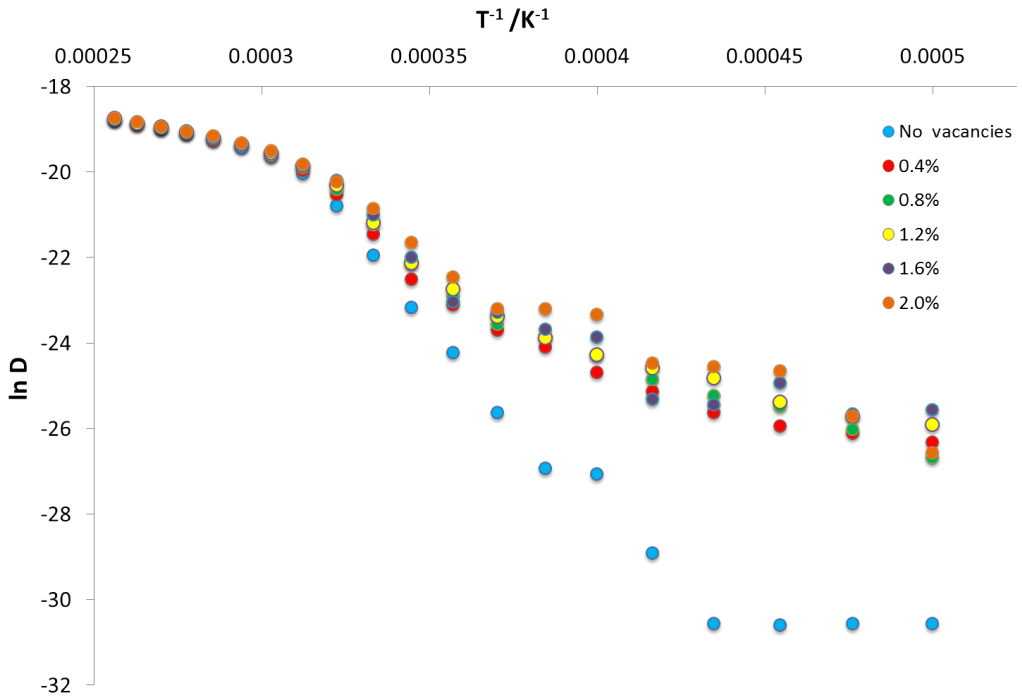

Figure 3.3: Diffusion data predicted for UO_2 using the morl potential for systems containing 0.0% - 2.0% vacancies.

At lower temperatures between 2000-2300 K a flat line is observed with a very low diffusion coefficient for the system containing no vacancies. Over the same temperature range only a gradual increase in diffusion is seen. In the temperature range of 2400-3100 K diffusion increases more rapidly and a steeper line is observed for all systems, however it can be seen that in the system without any vacancies, the diffusion rate increases more rapidly than in the systems containing vacancies. This is true until temperatures above 3100 K at which

point all systems gave nearly identical diffusion rates with a much shallower gradient than between 2400-3100 K.

The three temperature regions observed in figure 3.3 are as a result of diffusion in each being dependent on a different mechanism in a similar way to what was observed by Arima et al. in their simulations [157]. The vacancy diffusion region (below 2300 K) is where oxygen diffusion in the lattice is controlled by the formation of oxygen vacancies. This can be clearly seen as the bulk system containing no vacancies displays no diffusion. In this region the movement in the simulation times seen for the bulk system containing no vacancies correspond to vibrations. The lattice diffusion region (2400-3100 K) is dominated by the formation of oxygen Frenkel defects and is observed at higher temperatures than the vacancy region due to the energy required to form these defects. The third region observed was the fast ionic region where the oxygen sub lattice breaks down and behaves in a liquid-like manner, this is seen at temperatures above 3100 K. The fact that all 6 systems showed nearly identical behaviour in this region suggests that fast ionic behaviour is independent of defect concentration or that the concentration of defects is very high in all cases.

$$Ea = \frac{1}{2}\triangle G_{FO} + \triangle H^{M}_{O,V} \tag{3.4}$$

$$K = A\exp\left(-\frac{E_A}{RT}\right) \tag{3.5}$$

Table 3.3.4.1 displays the experimental and calculated activation energies of oxygen migration in the lattice and superionic diffusion regimes. The activation energy of lattice diffusion can be determined in two ways. The first utilises equation 3.4 which was used by Matzke [91] where $\triangle G_{FO}$ refers to the Gibbs free energy of formation of an oxygen Frenkel defect and $\triangle H^{M}_{O.V}$ is the enthalpy of oxygen vacancy migration to calculate the activation energy indirectly excluding any entropic effects. The second method calculates the activation energy directly from diffusion data using equation 3.5.

Table 3.10: Activation energies of oxygen diffusion determined from dynamical simulations compared with experimental values

Property /eV	Exp [16, 101]	Morl	Arima [157]	Morelon [40]
Lattice Diffusion (Dir)	2.60	3.12	5.70	2.94
Lattice Diffusion (Ind)	-	3.96	5.20	1.92
Superionic Diffusion	-	1.76	2.40	-

The lattice diffusion activation energies calculated using the direct method for both the Morelon and the Morl potentials show good agreement with the experimental Arrhenius values. Energies determined using the indirect method proved to be less accurate. Using both methods Arima predicts the lattice diffusion activation energy to be significantly higher than experiment. Comparing the activation energies of superionic diffusion, we predict a significantly lower value than for the lattice diffusion in agreement with Arima. However the lack of experimental diffusion data at a similar temperature makes the comparison quite difficult.

3.4 Summary

In this chapter we have outlined a robust, new computationally inexpensive potential model for UO_2 intended for use in the study of structural and transport properties of grain boundaries using both energy minimisation and molecular dynamics. Potential models were also derived for ThO_2 and U_3O_8 utilising the same anion-anion interaction used for UO_2. Predicted properties were compared to those obtained experimentally and using existing potential models.

The morl potential was fitted to experimental structure and elastic constants and accurately reproduces these properties. Elastic constants are related to heat transport and the effect of stress on the crystal, two properties which are important as we intend to use the morl potential to model grain boundary structures at high temperatures. Whilst defect energies were overall slightly higher than experimental values, the anion Frenkel defect energies were similar to experimental values and correctly predicted to be the most favourable defect. Predicted surface energies were also higher than experimental values but the order of stability matched literature studies. The morl potential excels in its representation of the

activation energy of oxygen vacancy migration and was the most accurate of the potential models studied. A disadvantage of the morl potential lies in the fact that the overall predicted defect energies are higher than experimental values. Oxygen Frenkel energies are only slightly higher than experiment but the uranium Frenkel defect energy in particular is significantly higher and as a result this model is unsuitable for the investigation of uranium transport.

Molecular dynamics studies of oxygen diffusion in UO_2 highlighted the existence of three different temperature regions each characterised by a distinct diffusion mechanism, an observation that is in line with previous potential based studies by Arima [101]. The three regions are the vacancy region, lattice diffusion region and superionic region. While the lack of high temperature data for UO_2 makes direct comparison with experimental diffusion coefficients difficult, the activation energy for lattice diffusion is in a similar range to experimental values.

Chapter 4

Tilt Grain Boundaries

In this chapter we describe the investigation of structure and diffusion of oxygen along six tilt grain boundaries in uranium dioxide. We initially discuss the procedure required to build these grain boundaries. As described in Chapter 2, we begin by using energy minimisation techniques to evaluate the formation and cleavage energies and so obtain the relative stability. The effect of temperature on the stability and structure of these interfaces is then investigated using molecular dynamics both to ascertain the importance of annealing as well as the dependence of oxygen diffusion on grain boundary structure.

The tilt grain boundaries studied are $\Sigma 3(111)$, $\Sigma 3(221)$, $\Sigma 5(210)$, $\Sigma 5(310)$, $\Sigma 11(311)$ and $\Sigma 19(331)$. These six tilt boundaries were selected for investigation because they have been studied in UO_2 or another fluorite structured material [77, 78]. A discussion of the relevant literature on tilt boundary systems is presented in Chapter 1. Whilst it has been previously suggested that grain boundaries enhance oxygen diffusion [100, 101] in UO_2 it is not known if all grain boundaries will similarly enhance diffusion and what effect, if any, grain boundary structure has on this property. By looking at six different grain boundaries we are significantly expanding the range of tilt boundaries investigated.

4.1 Generating Tilt Grain Boundaries and Static Lattice Simulations

A detailed description of how to build tilt grain boundaries using METADISE [123] can be found in Chapter 2. Galmarini et al. [172] has previously used this code to model similar interfaces in Y-doped alumina. The grain boundaries constructed are the $\Sigma 3(111)/[001]2\theta = 71°$, $\Sigma 3(221)/[001]2\theta = 39°$, $\Sigma 5(210)/[001]2\theta = 53°$, $\Sigma 5(310)/[001]2\theta = 36°$, $\Sigma 11(311)$-$/[001]2\theta$=129°, $\Sigma 19(331)/[001]2\theta$=52° tilt boundary systems. The misorientation angle or 2θ represents the angle between the [001] directions in each of the constituent grains. In the rest of this chapter each boundary will only be referred to by its Σ value and constituent surface.

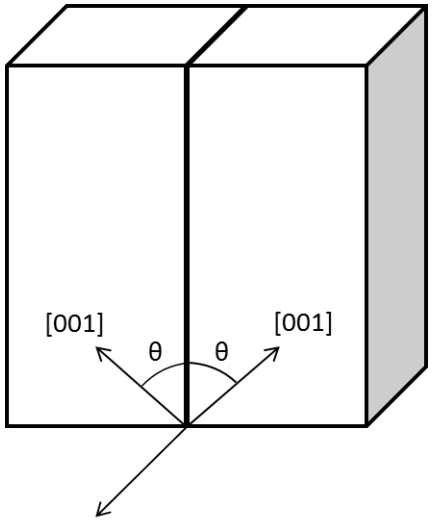

Figure 4.1: Illustration of a tilt grain boundary showing the misorientation angle(2θ)

The boundary is generated by reflecting the surface to generate a mirror image and performing a scan, which involves 'scanning' one surface over the other and at each point calculating the energy in order to find the most stable configuration. The scan involves constructing a virtual mesh parallel to the boundary plane. At each point of the mesh the structure is relaxed to its energy minimum thereby producing an energy surface with minima and maxima representing the most stable and unstable grain boundary structures. The energy surfaces for the tilt boundaries described in this study are shown in figure 4.2. The *x* axis on each energy surface corresponds to the displacement in the z direction and the *y* axis corresponds

to the displacement in the Y direction of the grain boundary. This YZ plane is the plane parallel to the grain direction. Different areas in the energy plots are coloured according to the the energy of the structures at that particular displacement.

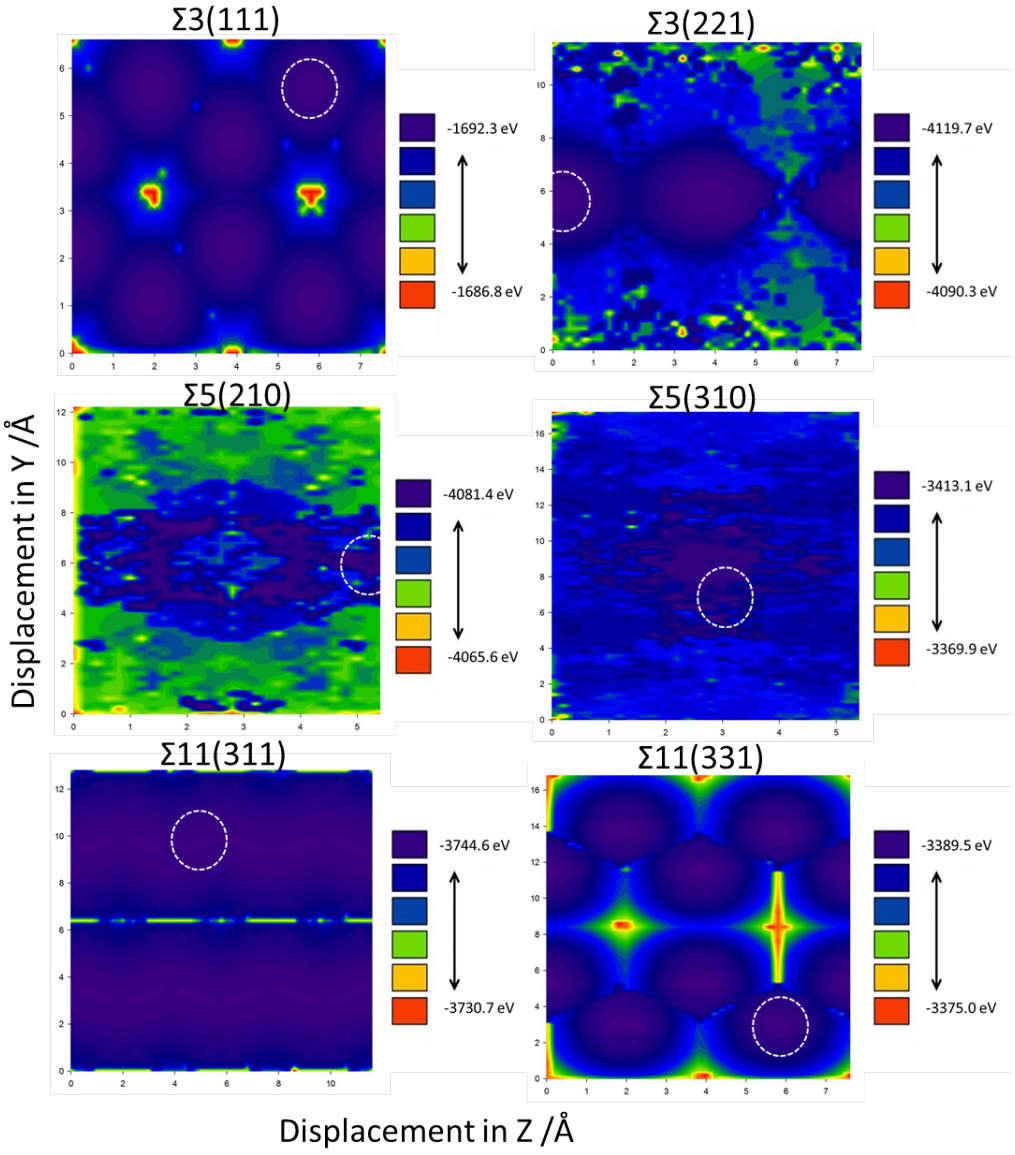

Figure 4.2: Energy surfaces calculated from the scan process for the six tilt grain boundaries using a step length of 0.2 Å. The structures were minimised at each step, the location of the energy minimum is indicated by a white circle on each plot.

The most stable configuration for each grain boundary corresponds to an energy minimum on the energy surface plots. Energy minima are represented by purple areas on the energy

surfaces (Figure 4.2) and it is from these points that the grain boundary can be generated. All six boundaries produced noticeably different energy surfaces from each other. All are highly symmetric showing a number of energy minima which indicate that using any of these minimum energy positions will generate identical grain boundaries. The grain boundary structures after energy minimisation are shown in figure 4.3. All structures are displayed with oxygen atoms removed for clarity. As part of the scan procedure each configuration generated was minimised, and these minimisations were performed using only BFGS as large numbers of calculations were needed to produce an energy surface. Once the relative displacement of the two surfaces that corresponds to the most stable configuration has been determined a more detailed energy minimisation calculation is performed using both BFGS and Newton-Raphson to produce a relaxed grain boundary structure.

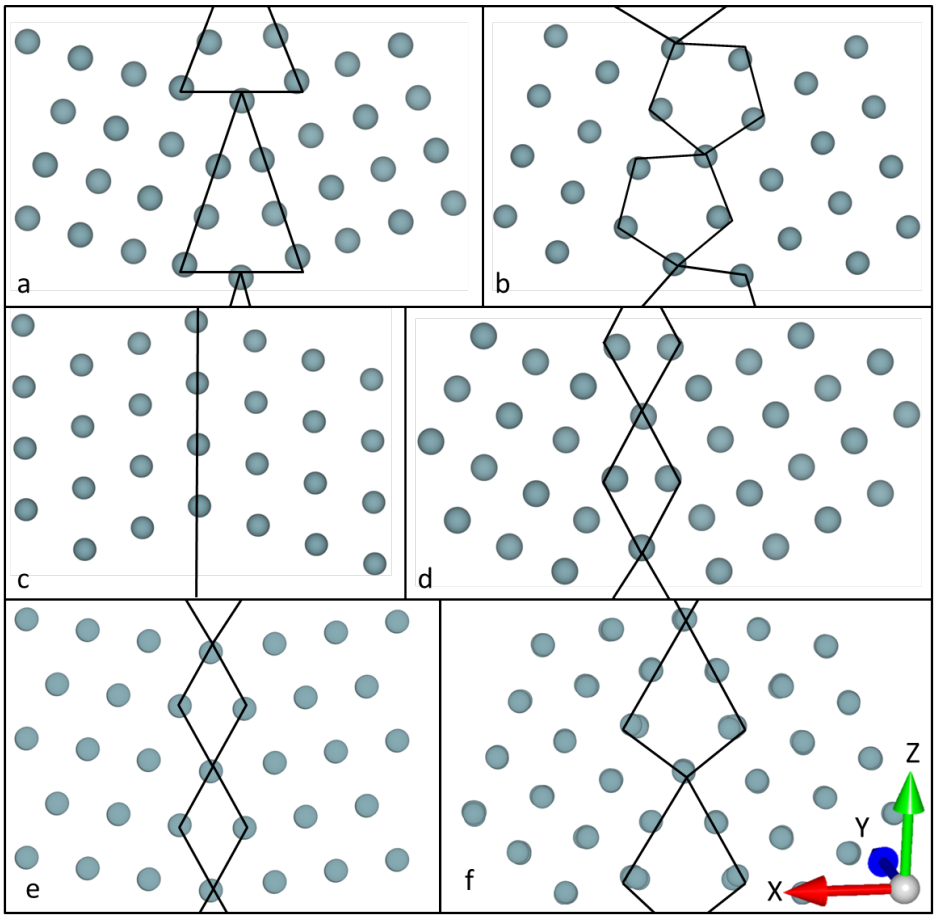

Figure 4.3: Relaxed structures produced for grain boundaries (a) $\Sigma5(310)$, (b) $\Sigma3(221)$, (c) $\Sigma3(111)$, (d) $\Sigma5(210)$, (e) $\Sigma11(311)$ and (f) $\Sigma19(331)$ showing only the uranium positions. The closest uranium positions at the boundary are highlighted to show the boundary geometry.

Of the six grain boundaries all are structurally different even though the corner sharing diamond pattern observed for the $\Sigma5(210)$ is similar to the structure of the $\Sigma11(311)$. Three of the structures the $\Sigma5(310)$, $\Sigma3(221)$ and $\Sigma19(331)$ contain pipes running in the Y direction parallel to the interface. Pipes provide a less restricted path through the structure in a particular direction, possibly facilitating movement of oxygen in the same direction. The $\Sigma5(310)$ structure predicted by METADISE [123] consists of linked highly symmetric triangles similar to one of the structures discussed by Dickey [74]. The $\Sigma3(111)$, $\Sigma5(210)$ and $\Sigma11(311)$ systems strongly resemble the experimental structures seen for ceria [77, 78] and zirconia [82]. The strong resemblance with experimentally observed structures gives

further confidence in the validity of the model and while no similar images exist to compare the other three boundaries we can be confident our model is providing an accurate representation.

Table 4.1 shows the formation (E_f) and cleavage (E_c) energies for the boundaries along with the corresponding surface energy (E_{surf}) and relaxation width either side of the interface. The calculated formation and cleavage energies and the corresponding boundary width determined from relaxation for each of the grain boundaries as well as misorientation angles are also displayed. The grain boundary width represents the distance at which the grain boundary causes the material to behave differently to the bulk and can be defined in a number of ways. Relaxation width refers to the distance from the boundary interface in which the interatomic distances do not match to 2 decimal places those of bulk UO_2 as calculated using the same potential model.

Table 4.1: Grain boundary formation (E_f) and cleavage energies (E_c) alongside the corresponding surface energies (E_{surf}), grain boundary width and misorientation angle (2θ).

Boundary	E_f /eV	E_c /eV	E_{surf} /Jm^{-2}	Width /Å	Misorientation Angle /°
$\Sigma3(111)$	0.30	0.52	1.33	6.5	71
$\Sigma3(221)$	0.48	0.49	1.65	13.0	39
$\Sigma5(210)$	1.10	0.51	3.36	12.5	53
$\Sigma5(310)$	0.76	0.64	3.30	18.0	36
$\Sigma11(311)$	1.37	4.52	2.94	10.0	129
$\Sigma19(331)$	1.97	1.55	1.76	6.5	52

The $\Sigma19(331)$ and $\Sigma3(111)$ boundaries have the smallest grain boundary widths while the $\Sigma5(310)$ boundary had by far the largest. There is no obvious correlation between width and formation energy, cleavage energy or misorientation angle. It appears that there is a general link between the formation energy of the grain boundaries and the value of Σ. It can be seen that higher Σ values give rise to higher formation energies although both $\Sigma5$ systems are seen to give different values. Also noticeable is a link between the formation energy and the energy of the corresponding free surface. However no such link is identifiable with respect to cleavage energies which appear to be completely independent of width, formation energy and surface energies. The $\Sigma3$ systems require less energy to form than the $\Sigma5$ boundaries which is likely as a result of the low energies of the corresponding surfaces. However, little variation in cleavage energies is seen between the different systems. The literature misorientation angles available for $\Sigma5(310)$ [74], $\Sigma3(111)$, $\Sigma3(221)$ and $\Sigma11(311)$ [82]

closely match those calculated from the models in this study providing further proof of the structural accuracy of our grain boundary systems.

4.2 Dynamical Studies

The most stable grain boundary configurations generated using energy minimisation, were simulated using molecular dynamics simulations as implemented in the DL_POLY code [173] where the forces between atoms consisted of long-range Coulombic and short-range terms. The electrostatic interactions of the system were evaluated using the Ewald method to a precision of 10^{-5} and the potential cut-off was 8.0 Å. All simulations were run with a timestep of 1 fs and with the Nosé-Hoover thermostat/barostat. The simulation cells of grain boundary configurations comprised two boundaries running in opposite directions equally spaced by a bulk region so that the effect of the relaxation of one boundary due to the mismatch is negligible on the other boundary and on the middle of the bulk region.

All systems were equilibrated at 300 K in the NPT ensemble for 1ns until fluctuations of the configurational energy were negligible. Annealing at high temperatures was performed for each configuration and the stability of each boundary with respect to temperature is discussed later in this chapter. The temperature was increased up to 3000 K and decreased back to 300 K in the NPT ensemble for up to 1ns in order to reach stable grain boundary structures. Grain boundaries were then heated to temperatures between 2000 K and 3000 K every 100 K in the NPT ensemble for 1.1ns until the fluctuations in the volume and the configurational energy at that temperature were negligible. Not all of the systems discussed in this investigation were stable at 3000 K and the boundary was seen to diffuse. As a result some were annealed at slightly lower temperatures.

Different grain boundaries are stable in different temperature ranges with instability displayed through structural changes and boundary movement. The annealing process was therefore essential to ensure that the grain boundary adopts the most stable configuration and that it can then be investigated in the wider range of temperatures. The annealed structures for each grain boundary are displayed in each sub-chapter along with the corresponding density plot.

Grain boundary diffusion data were collected using the NVT ensemble over a time of 1ns

(following 100 ps equilibration). Diffusion coefficients in each of the grain boundaries were determined at temperatures of 2000 K to 3000 K except where boundaries were seen to diffuse at higher temperatures. In such cases diffusion coefficients were calculated up to the highest temperatures at which the boundaries remained stable. Oxygen diffusion cannot be calculated as an average over the whole system as large areas of bulk surrounding the interface would likely mask any contribution by the grain boundary. In order to evaluate oxygen diffusion behaviour in the grain boundary region the simulation cell was divided into segments or bins parallel to the grain boundary plane. A description of the method of determining diffusion rates is detailed in chapter 2. The width of each segment was equal to the U-U interatomic distances in the X direction (figure 4.4) and the correlation time used was 25 ps. In each segment the 3 components (*Dx*, *Dy* and *Dz*) of the diffusion were calculated and normalized to the bulk values to give an indication of any relative increase or decrease in the diffusion. Bulk values were determined from the bulk regions in each of the grain boundary simulations. Bulk oxygen diffusion coefficients range from 5.4×10^{-14} m^2 s^{-1} at 2000 K to 2.93×10^{-10} m^2 s^{-1} at 3000 K. Atomic densities were also calculated by dividing up the cell perpendicular to the boundary using segments of 0.1 Å in width. Density profiles are displayed for each system along with the boundary structure at the same temperature. The uranium density peaks are aligned to the corresponding atoms in the structural pictures. For each system density and diffusion widths are identified. Density width refers to the distance from the interface in which the peaks of the density profile are seen to differ from bulk behaviour. Similarly diffusion width refers to the distance from the interface in which oxygen diffusion is seen to behave in a different manner to the bulk values.

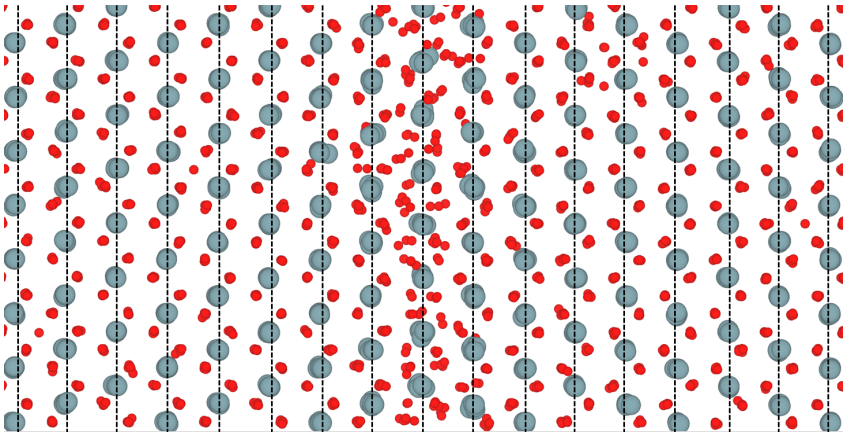

Figure 4.4: $\Sigma 3(111)$ grain boundary showing segments used to calculate *Dx*, *Dy* and *Dz*. Uranium atoms are displayed in blue and oxygen in red.

For each of the boundaries, graphs showing oxygen diffusion in the grain boundary region are shown. Diffusion was determined in three dimensions where X corresponds to the direction perpendicular to the grain boundary, Y is the direction of the pipes and Z is the direction perpendicular to the pipe and parallel to the grain boundary plane. The grain boundary plane is at the origin while the positive and negative labels signify 2 sides of the interface which are usually symmetric. Whilst diffusion data was gathered at many temperatures, only diffusion at significant temperatures is shown. These significant temperatures correspond to the three regions of oxygen diffusion identified in chapter 3 and where possible a plot showing diffusion at a temperature in each of these regions is shown. As previously mentioned each simulation cell contains two boundaries, one in the middle of the cell and one that occupies the cell edge. These interfaces are identical and as a result only the boundary at the centre of the cell is shown.

4.2.1 $\Sigma 3(111)$

4.2.1.1 Structure and Stability

Figure 4.5 displays the annealed structures of $\Sigma 3(111)$ at 2000 K and 3000 K with the corresponding z-density profile. In line with earlier grain boundary structures systems are shown with the oxygen atoms removed.

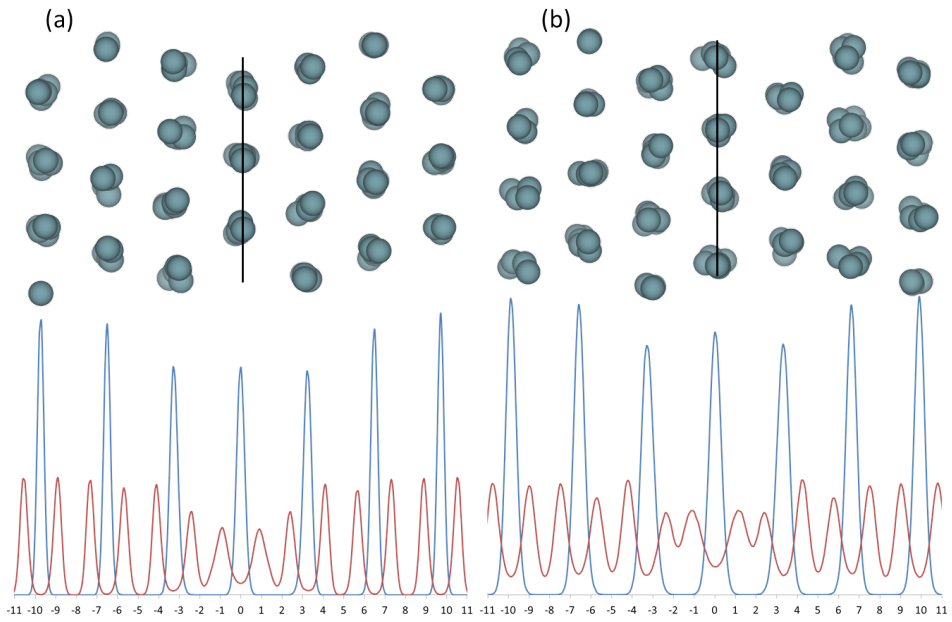

Figure 4.5: Structures and density plots of the annealed $\Sigma 3(111)$ grain boundary. Uranium density is shown in blue with oxygen density in red. Structures are shown at (a) 2000 K and (b) 3000 K.

The annealed structures of $\Sigma 3(111)$ are identical to those predicted by energy minimisation calculations and no difference can be seen over any of the temperatures in this study. The $\Sigma 3(111)$ was stable over the entire range of 2000 K to 3000 K. The density width of this system is about 10 Å which is slightly higher than that predicted by relaxation.

4.2.1.2 Transport Properties

Normalised diffusion coefficients for the grain boundary region is shown in figure 4.6 at three different temperatures corresponding to diffusion in the vacancy, lattice and fast ion regions respectively. Diffusion plots at all three temperatures shows oxygen diffuses more rapidly in all directions at the boundary and in the 6 Å of bulk either side of the interface. This is the diffusion width at 2000 K and is less than the width predicted from the density data but closely resembles the width of relaxation. With increasing temperature the diffusion width is seen to increase. At 2000 K diffusion is isotropic with diffusion at the interface 20 times faster than bulk values. As the temperature increases diffusion becomes more anisotropic and diffusion in the Y and Z directions becomes more prominent indicating that at higher temperatures (above 2600 K) oxygen will diffuse more freely parallel to the

boundary plane. Interfacial diffusion in Y and Z directions at 2600 K is still about 20 times faster than the bulk, however the diffusion in the X direction is only 17 times faster. The reduction in normalised diffusion coefficient in X indicates reduced diffusion across the interface between the two grains. At temperatures close to 3000 K the bulk region tends toward fast ion behaviour greatly reducing normalised diffusion rates. As a result diffusion at the interface is only about twice as fast as the bulk. The range of calculated bulk diffusion coefficients are listed in Section 4.2.

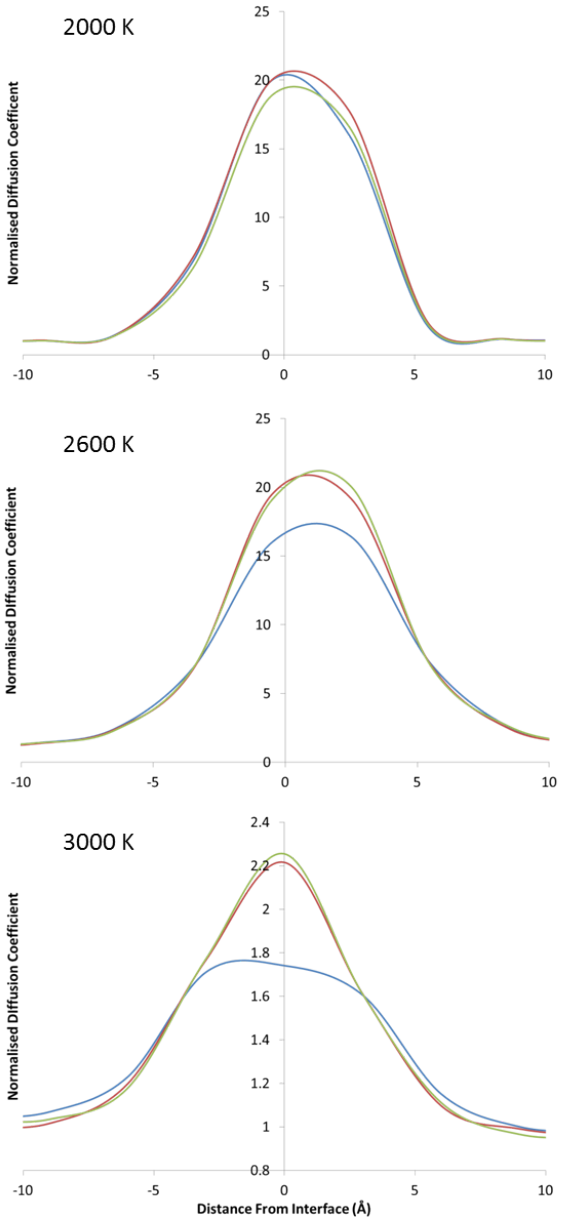

Figure 4.6: Normalised oxygen diffusion profiles for the $\Sigma 3(111)$ grain boundary. The X component of diffusion is shown in blue, the Y component in red and the Z component in green. The normalised value of X corresponds to the diffusion coefficient in the X direction (Dx) divided by the bulk diffusion coefficient (D_B).

4.2.2 $\Sigma 5(210)$

4.2.2.1 Structure and Stability

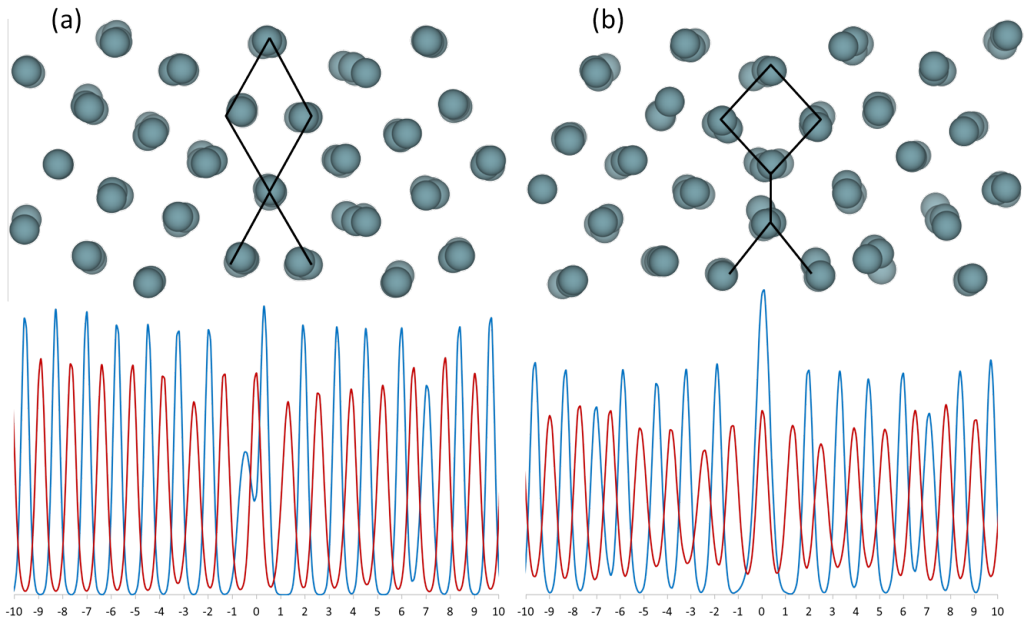

Figure 4.7: Structures and density plots of the annealed $\Sigma 5(210)$ grain boundary. Uranium density is shown in blue with oxygen density in red. Structures are shown at (a) 2000 K and (b) 2900 K.

Figure 4.7 displays the annealed structures of $\Sigma 5(210)$ at 2000 K and 2500 K with z-density profiles. At temperatures below 2400 K the $\Sigma 5(210)$ boundary structure is similar to the structure seen in the energy minimisation calculations, however above 2400 K a structural change is observed with the boundary now showing shortened diamond shapes arranged end on end. This change is also visible in the density plots as the split central uranium peak becomes a large single peak as a result of there being enough energy in the system to move the uranium ions in to a new configuration. This new structure persists until temperatures exceed 2900 K at which point the boundary becomes mobile and hence no density or diffusion data could be obtained at 3000 K. When the system is cooled the high temperature structure returns the original low temperature configuration. From the density plots the width of the grain boundary is predicted to be 10.5 Å which is slightly higher than the width of relaxation seen for the same system.

4.2.2.2 Transport Properties

Diffusion data for the $\Sigma5(210)$ boundary at three different temperatures is shown in figure 4.8.

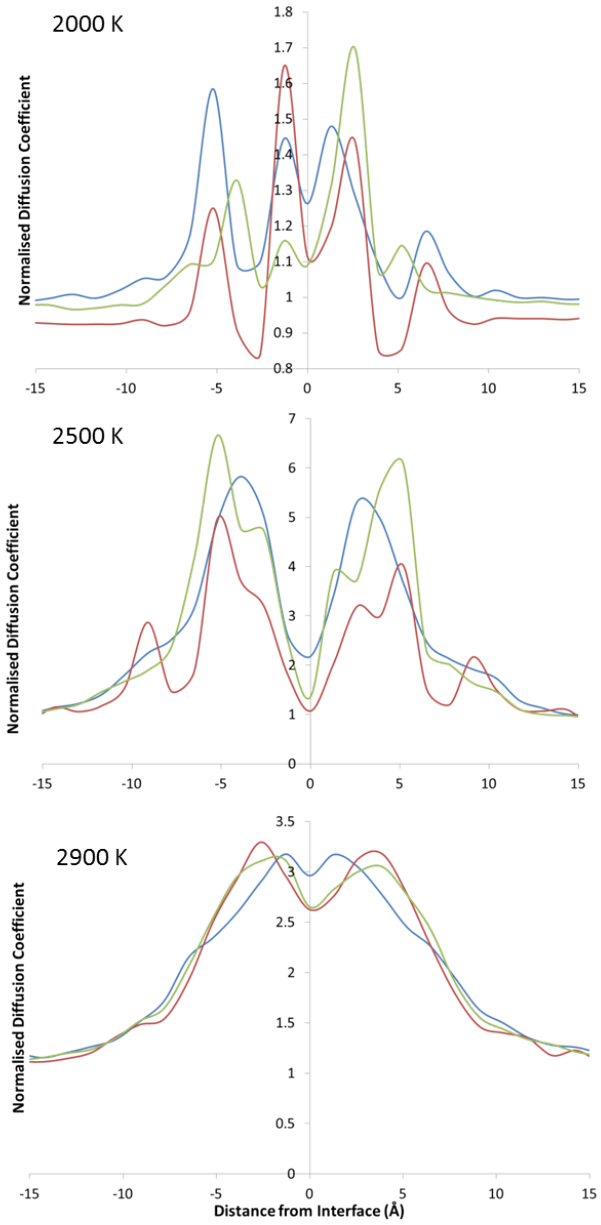

Figure 4.8: Normalised oxygen diffusion profiles for the $\Sigma5(210)$ grain boundary. The X component of diffusion is shown in blue, the Y component in red and the Z component in green. The normalised value of X corresponds to the diffusion coefficient in the X direction (Dx) divided by the bulk diffusion coefficient (D_B).

Diffusion behaviour differs markedly from the $\Sigma3(111)$ at 2000 K, as it was anisotropic with 4 major peaks of enhanced diffusion in each direction. The relative heights of these

peaks vary significantly and even the highest peaks showed normalised diffusion rates only 1.7 times faster than the bulk, which suggests the boundary is displaying only slight enhancement of oxygen transport at these temperatures. Oxygen diffusion at this temperature was enhanced over a width of 13 Å which is higher than the density width but similar to the width of relaxation, this distance increased with increasing temperature. Normalised diffusion rates are seen to change between 2400 K and 2500 K where there is a sudden increase either side of the interface, at this temperature diffusion is about 6 times faster than the bulk in peaks either side of the interface. The centre of the interfacial region however shows very little increase in diffusion rate over bulk values. This sudden increase in diffusion at this temperature coincides with the phase change that occurred at this temperature and this change in structure appears to facilitate enhanced diffusion rates although not at the centre of the interface. Normalised diffusion rates remain fairly constant with increasing temperature until they reach 2900 K. At this temperature the bulk region is starting to show fast ion diffusion behaviour causing a reduction in the intensity of normalised diffusion in the boundary region. In addition there is a sudden increase in diffusion at the interface with the onset of fast ion behaviour to the point where diffusion fairly is isotropic. The rate is about 3 times as fast as the bulk at two peaks either side of the interface with a slight trough between them. Between 2000-2900 K the normalised diffusion rates are vastly lower than those seen in the $\Sigma 3(111)$ grain boundary.

4.2.3 $\Sigma 3(221)$

4.2.3.1 Structure and Stability

Figure 4.9 displays the annealed structures of $\Sigma 3(221)$ at 2000 K and 2500 K alongside plots of z-density at the same temperatures. This grain boundary system was only stable to temperatures of 2500 K as at temperatures exceeding this the boundary was seen to diffuse meaning it wasn't possible to determine accurate diffusion coefficients or density data. Boundary movement might be a mechanism of growth of grains in polycrystalline structures as the least stable boundaries will move and eventually merge when exposed to high temperatures.

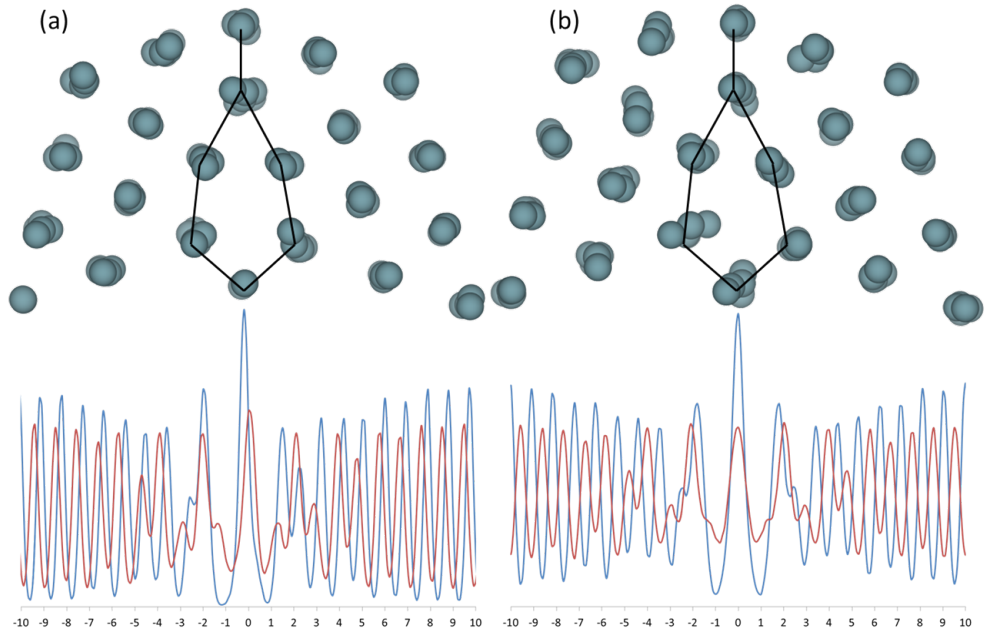

Figure 4.9: Structures and density plots of the annealed $\Sigma 3(221)$ grain boundary. Uranium density is shown in blue with oxygen density in red. Structures are shown at (a) 2000 K and (b) 2500 K.

The structure of the $\Sigma 3(221)$ grain boundary is seen to change once annealed. After energy minimisation it consisted of pentagons linked by the corners. After the annealing process the boundary is more symmetrical and triangular in nature. Structural change causes a reduction in the free volume at the interface. The density width of 8 Å is significantly lower than the relaxation width, but it is possible that the change of structure will have had an impact on this.

4.2.3.2 Transport Properties

Diffusion data for the $\Sigma 3(221)$ boundary is shown in figure 4.10. At the lowest temperature studied (2000 K) the diffusion profile shows diffusion to be enhanced at a distance of about 8 Å from the interface. From this distance the intensity of the peaks gradually increases to a maximum about 2 Å from the interface where at the interface itself a trough is seen. Diffusion in this system is highly anisotropic and the intensity of normalised diffusion coefficients depends quite heavily on the direction of study. At 2000 K oxygen diffuses most rapidly in the Y direction and at its maximum rate is about 27 times faster than in the bulk. The same trend was visible at higher temperatures with very similar behaviour seen at 2500

K. Oxygen diffusion is similarly fastest in the Y direction with normalised diffusion rates 38 times faster than the bulk in the peaks surrounding the boundary interface. At this increased temperature the width of diffusion is also seen to increase. Enhanced diffusion in the Y direction corresponds with diffusion in the same direction as pipes that run parallel to the boundary.

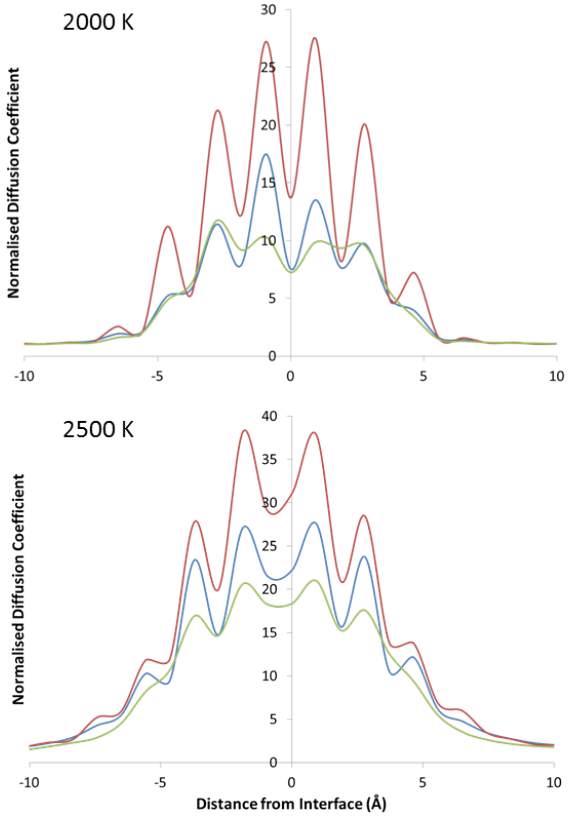

Figure 4.10: Normalised oxygen diffusion profiles for the $\Sigma 3(221)$ grain boundary. The X component of diffusion is shown in blue, the Y component in red and the Z component in green. The normalised value of X corresponds to the diffusion coefficient in the X direction (Dx) divided by the bulk diffusion coefficient (D_B).

4.2.4 $\Sigma 5(310)$

4.2.4.1 Structure and Stability

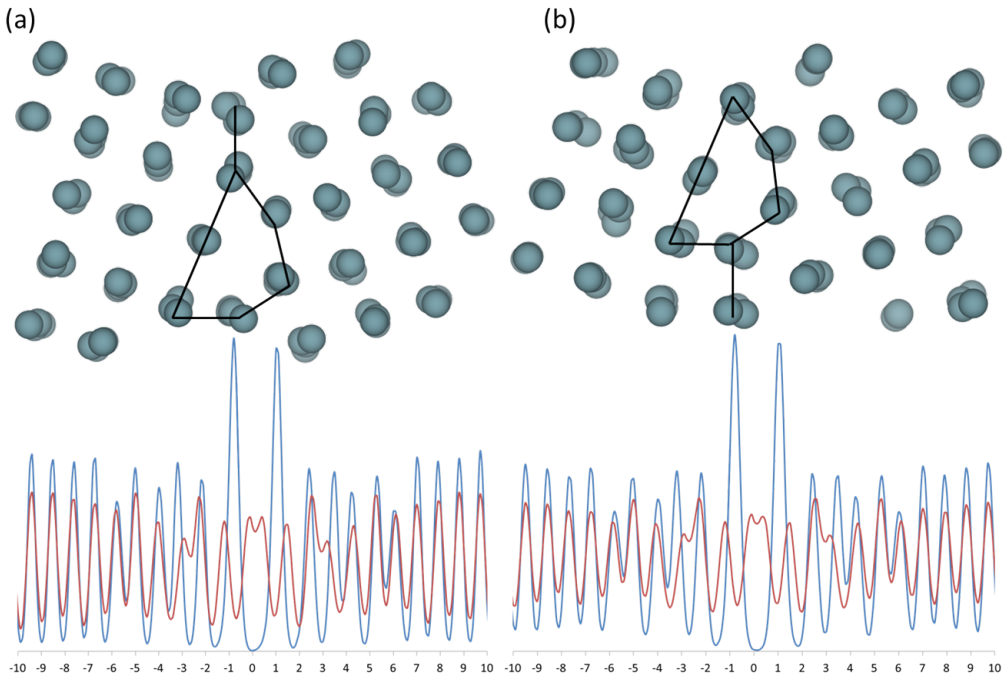

Figure 4.11: Structures and density plots of the annealed $\Sigma 5(310)$ grain boundary. Uranium density is shown in blue with oxygen density in red. Structures are shown at (a) 2000 K and (b) 2600 K.

The annealed structure (Figure 4.11) of the $\Sigma 5(310)$ boundary differs from the structure predicted using energy minimisation. The large highly symmetric triangle shapes predicted by energy minimisation calculations are replaced with a smaller, more distorted triangular pattern. However, it is metastable and if this high temperature structure is cooled it reverts back to the structure seen in the energy minimisation study. This structural change may account for the large difference between the relaxation width and density width of 20 Å. The high temperature structures seen for the $\Sigma 5(310)$ boundary bear some resemblance to those of Dickey et al. [74] in yttria-stabilised cubic zirconia. However it was observed without the need to reduce cation crowding, likely accounting for the distorted nature of the triangles. At temperatures of 2600 K and above the grain boundary was seen to diffuse making the determination of structural and diffusion data impossible.

4.2.4.2 Transport Properties

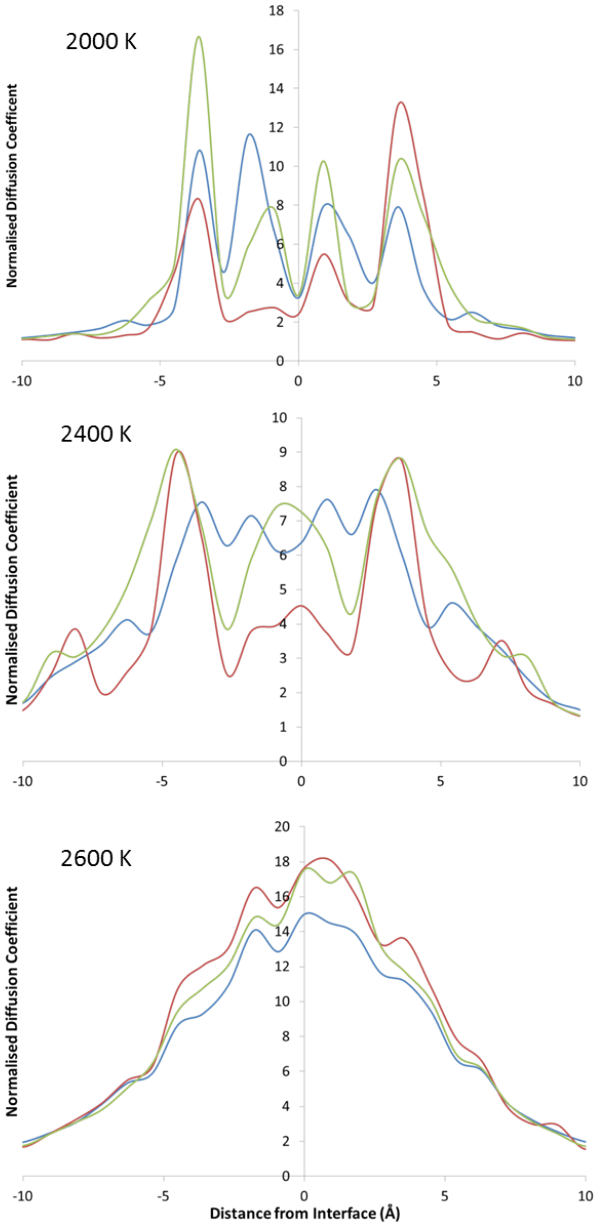

Figure 4.12: Normalised oxygen diffusion profiles for the $\Sigma 5(310)$ grain boundary. The X component of diffusion is shown in blue, the Y component in red and the Z component in green. The normalised value of X corresponds to the diffusion coefficient in the X direction (Dx) divided by the bulk diffusion coefficient (D_B).

Figure 4.12 illustrates the diffusion data seen in the $\Sigma 5(310)$ boundary system. At 2000 K the diffusion profile showed that oxygen diffusion was enhanced at a distance of up to 10 Å from the interface which is identical to the density width at the same temperature. The main component of this was 2 peaks of enhanced diffusion either side of the interface where the

largest enhancement is seen. The most significant increase in oxygen diffusion coeficients is observed to be 16 times faster than bulk diffusion. While the four peaks are observed in all directions the heights vary significantly with the direction of study. Apart from these peaks only a small enhancement is seen, including the interface. With increased temperature (2400 K) the diffusion profile shows anisotropic behaviour and the four peaks seen along all axes at lower temperatures are replaced by a more complex pattern. Normalised diffusion at the interface increases in all axes, particularly in the Z direction but is still less significant than diffusion in some of the surrounding material. The diffusion profile at this temperature is also significantly more symmetrical, but there has been a reduction in the maximum normalised diffusion rate compared to 2000 K. At 2600 K this trend is reversed as diffusion becomes more isotropic, and is up to 18 times faster than the bulk which is even higher than at 2000 K. The interface also becomes the location of fastest diffusion and a steady decrease in normalised diffusion rates is seen moving away from this point. This significant change of behaviour may be the result of the two surfaces sliding along each other in a direction parallel with the grain boundary plane which is observed at this temperature.

4.2.5 $\Sigma 11(311)$

4.2.5.1 Structure and Stability

The annealed structures of the $\Sigma 11(311)$ grain boundary which are displayed in figure 4.13 show no change in structure when compared with the results predicted using energy minimisation although the density plot at 2700 K does look different there does not appear to be any obvious structural changes. This structure was not stable over the entire range of temperatures and was seen to move at temperatures above 2700 K. Boundary width determined from the density profiles is 6 Å which is significantly shorter than the width of relaxation.

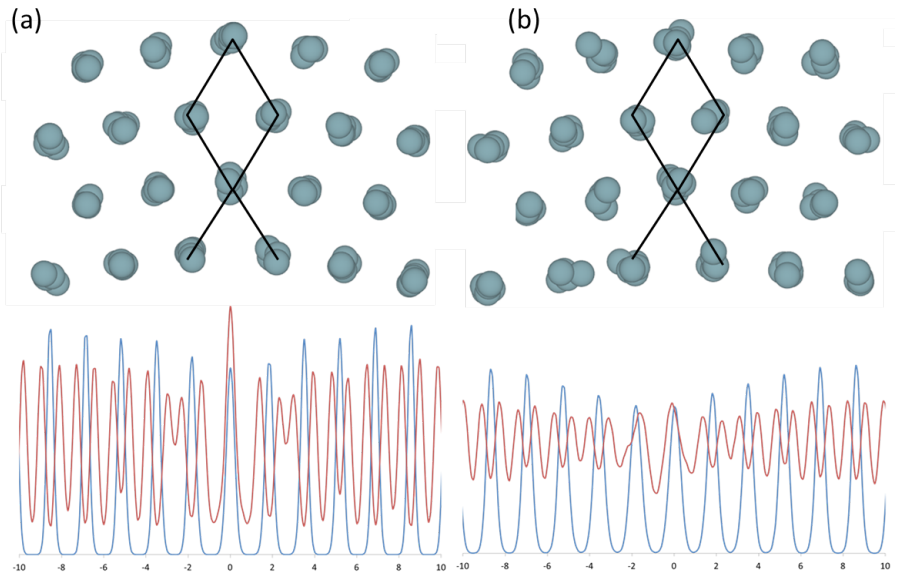

Figure 4.13: Structures and density plots of the annealed $\Sigma 11(311)$ grain boundary. Uranium density is shown in blue with oxygen density in red. Structures are shown at (a) 2000 K and (b) 2700 K.

4.2.5.2 Transport Properties

Diffusion data for the $\Sigma 11(311)$ grain boundary is displayed in figure 4.14. Across the range of temperatures studied the diffusion system displayed only a single peak centred over the grain boundary interface, with enhanced diffusion seen at distances of up to 5 Å with a steady decrease in diffusion rates until this point. This distance is significantly shorter than the relaxation width and similar to the width of the interface as predicted by the z-density plots. This diffusion width increased with temperature. At 2000 K diffusion is fairly isotropic with only small variations in normalised diffusion rates depending on the direction of study. However higher temperatures see diffusion in the X axis, which corresponds to inter-granular diffusion to be less significant at higher temperatures. Normalised diffusion rates initially increase with temperature but are seen to decrease towards higher temperatures from a maximum of diffusion 20 times faster than the bulk at 2000 K to 32 times faster than the bulk at 2400 K and then down to as low as 19 times faster at 2700 K. At the lowest temperatures studied diffusion between the grains is almost comparable to diffusion parallel to the boundary interface. However as temperature increases diffusion across the interface becomes less significant.

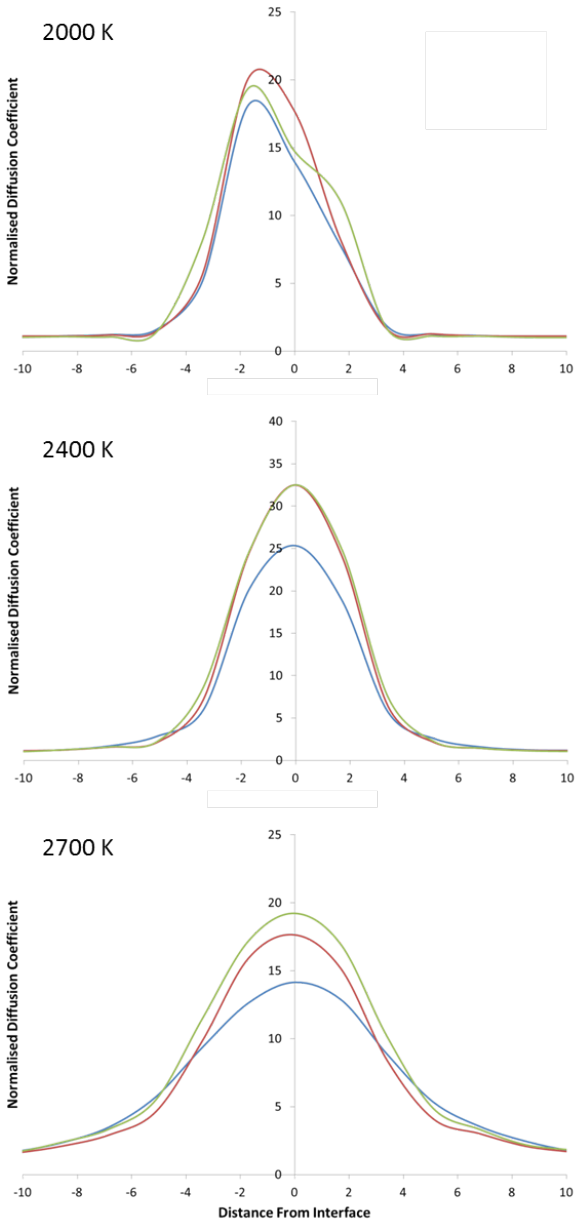

Figure 4.14: Normalised oxygen diffusion profiles for the $\Sigma 11(311)$ grain boundary. The X component of diffusion is shown in blue, the Y component in red and the Z component in green. The normalised value of X corresponds to the diffusion coefficient in the X direction (Dx) divided by the bulk diffusion coefficient (D_B).

4.2.6 Σ19(331)

4.2.6.1 Structure and Stability

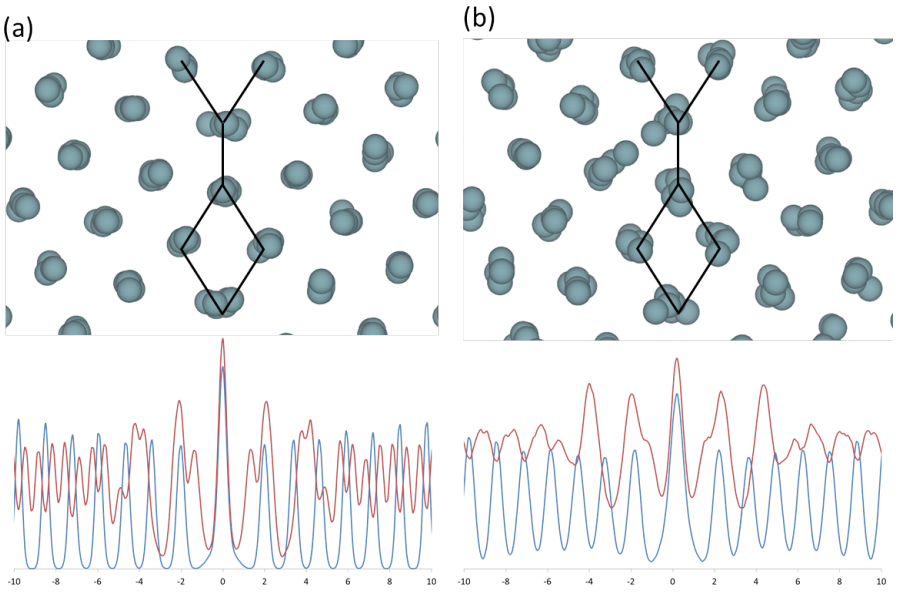

Figure 4.15: Structures and density plots of the annealed Σ19(331) grain boundary. Uranium density is shown in blue with oxygen density in red. Structures are shown at (a) 2000 K and (b) 3000 K.

Structural data from the Σ19(331) annealed grain boundaries can be seen in figure 4.15. The structure produced by the annealing process is different from the that determined using energy minimisation calculations. Previously the boundary had been triangular with large voids running the length of the boundary in the Y direction, the structure after the annealing process consists of linked diamonds that have formed as a result of moving one of the uranium arrays into the voids. These diamond shapes resemble the high temperature structure seen for the Σ5(210) boundary although unlike that system the new structure for this boundary is stable at all temperatures. From the density graphs the width of the boundary is predicted to be 8 Å which is very similar to the width predicted by relaxation. The annealed structures of the Σ19(331) boundary were stable over the entire range of temperatures in this study and are remarkably different from those observed from energy minimisation simulations.

4.2.6.2 Transport Properties

Oxygen diffusion in the $\Sigma19(331)$ grain boundary is shown in figure 4.16. Diffusion behaviour at 2000 K is anisotropic with enhanced normalised diffusion rates seen at a distance of 7 Å from the interface. Diffusion is fastest in the Y direction at the interface where normalised diffusion rates are 42 times faster than in the bulk region. Diffusion in the X and Z directions consists of broad shallow peaks of significantly lower intensities than those produced for diffusion in the Y direction. A similar trend is observed at 2400 K although the profile at this temperature is more symmetrical than at lower temperatures. The Y component of diffusion measured at the interface is still seeing the fastest diffusion rates although the normalised rate is now only 30 which is quite dramatically reduced compared to the value at lower temperatures. Again at 3000 K diffusion in the Y direction is faster than in either the X or Z. This time however, the normalised diffusion coefficient is only just under twice as fast as the bulk. A dramatic reduction in this value arises due to the onset of the fast ionic region of diffusion in the bulk and is consistent with observations in all other grain boundary systems that are stable at this temperature. At 3000 K the shape of the diffusion profile resembles that seen at a similar temperature for the $\Sigma5(210)$ boundary with diffusion in each direction consisting of a broad peak but instead of the tip of the peak sitting at the interface there is a slight trough meaning that twin peaks are observed either side of the interface. The fact that this resembles the shape of the diffusion profile of $\Sigma5(210)$ at similar temperatures is probably due to the similarity in structures of the two systems. The fact that oxygen was consistently seen to diffuse faster at the interface suggests that the presence of a pipe running the length of the boundary in the Y direction is significantly enhancing oxygen transport. In common with the other tilt grain boundaries the diffusion width of this boundary is seen to increase with the increasing temperature of the simulations.

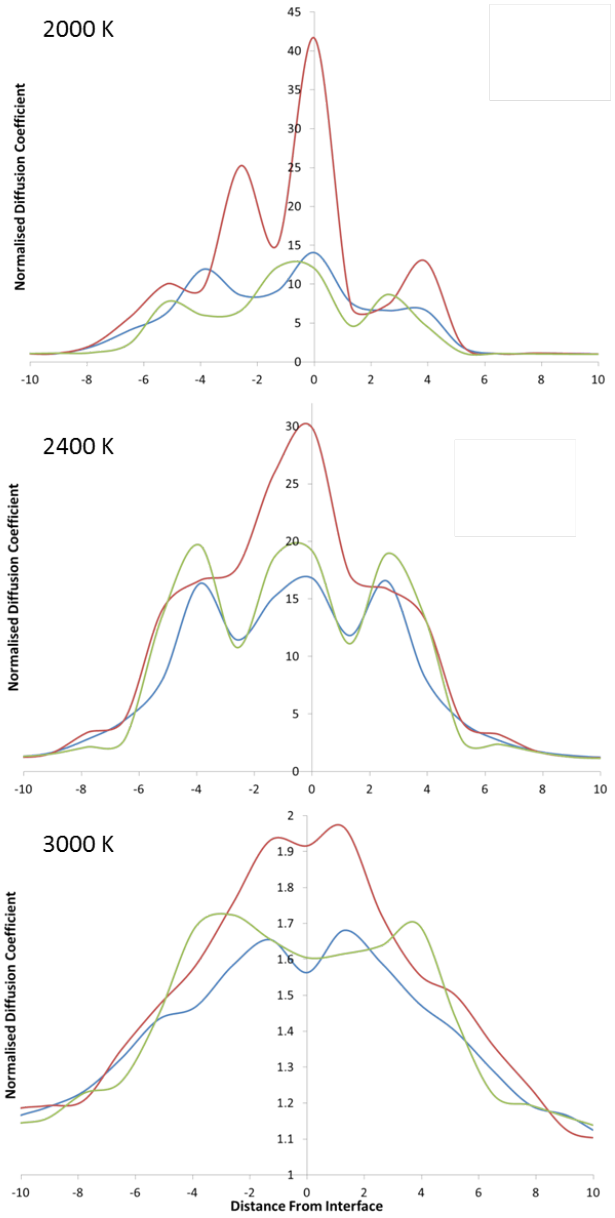

Figure 4.16: Normalised diffusion profiles for the $\Sigma 19(331)$ grain boundary. The X component of diffusion is shown in blue, the Y component in red and the Z component in green. The normalised value of X corresponds to the diffusion coefficient in the X direction (Dx) divided by the bulk diffusion coefficient (D_B).

4.2.7 Tilt Boundary Comparison

Grain boundary widths determined from diffusion results at 2000 K are consistently lower than those calculated from atomic densities, the only exception to this being the $\Sigma 5(210)$ which has a diffusion width 5 Å larger (see Table 4.2). This different result is likely due to the fact that even though the densities suggest the system turns to bulk 10 Å from the

boundary, the varying density in the boundary region may have an effect on any layers below. All six grain boundary systems predicted the diffusion widths to increase with temperature which in some instances caused the diffusion width to exceed the relaxation width. Interestingly the density widths showed little if any changed at increased temperatures.

Table 4.2: Comparison of grain boundary widths, relating to the distance at which the interatomic distances, atomic density and oxygen diffusion are altered by the grain boundary.

Boundary	Relaxation Width /Å	Density Width /Å	Diffusion Width /Å
$\Sigma3(111)$	6.5	10	6
$\Sigma3(221)$	13.0	8	7.5
$\Sigma5(210)$	12.5	10.5	13
$\Sigma5(310)$	18.0	10	10
$\Sigma11(311)$	10	10	5
$\Sigma19(331)$	6.5	8.5	7

The diffusion profiles of all six grain boundaries show enhanced normalised diffusion rates over temperatures of 2000 K to 3000 K. This observation that grain boundaries are indeed fast diffusion pathways is in line with observations from previous computational studies [100, 101]. The increase in oxygen diffusion rates facilitated by the presence of grain boundaries was not limited to just the grain boundary interface but in all instances the region of bulk material surrounding the interface also witnessed faster diffusion rates. The width of this region of increased diffusion varied for each boundary with significant variation also observed in the relative intensities of normalised diffusion at different distances from the interface within this region.

All the grain boundaries studied showed oxygen transport to display some degree of anisotropic behaviour with some systems showing greater directional dependence than others. This is particularly obvious in the case of the $\Sigma19(331)$ boundary which particularly at low temperatures displayed enormous variation in diffusion behaviour depending on the direction it is determined in. The $\Sigma3(111)$ and $\Sigma11(311)$ boundaries on the other hand displayed by far the lowest directional dependence and at low temperatures (2000 K) diffusion in these systems was isotropic.

The large variation in diffusion between the different boundaries would appear to be as a result of the variations in structure seen in the different systems. There are a number of examples that illustrate this structural influence first and foremost of which is the reconstruction observed for the $\Sigma5(210)$ system at 2400 K. This major structural rearrangement

of the grain boundary coincides with a marked change in diffusion behaviour in this system. The same grain boundary can provide further evidence of this when compared with the $\Sigma 19(331)$ tilt boundary. At high temperatures both systems have a similar grain boundary structure and normalised diffusion graphs of these systems at 2900 K and 3000 K respectively look remarkably similar. This is also evidenced by the $\Sigma 3(111)$ and $\Sigma 11(311)$ systems, both are constructed from flat surfaces, have the highest misorientation angles of all of the six boundaries studied and produce diffusion profiles of a very similar shape. The similarities are not limited to the shape as the diffusion widths of both boundaries are also similar and the most isotropic behaviour. This similarity in diffusion behaviour may be because both of these systems do not possess pipes.

While all rates of oxygen diffusion increase with temperature the normalised diffusion rates at the interface and in the area around the boundary can vary particularly significantly with changing temperature. However one consistency observed across all systems at temperatures nearing 3000 K was that normalised diffusion at the boundary decrease sharply. At this temperature the bulk system is near superionic behaviour and as was observed in chapter 3 the presence of defects had no obvious impact on diffusion rates in this region. The result of this is that there is a large increase in bulk diffusion rates resulting causing the normalised diffusion rates at the boundary to drop. Another consequence of high temperatures was that the diffusion at these temperatures was often more isotropic.

A difficulty exists in comparing values of normalised diffusion between the boundaries as each one has a different width. However if the total boundary diffusion in each system is divided by the diffusion width we can calculate the average contribution of each grain boundary.

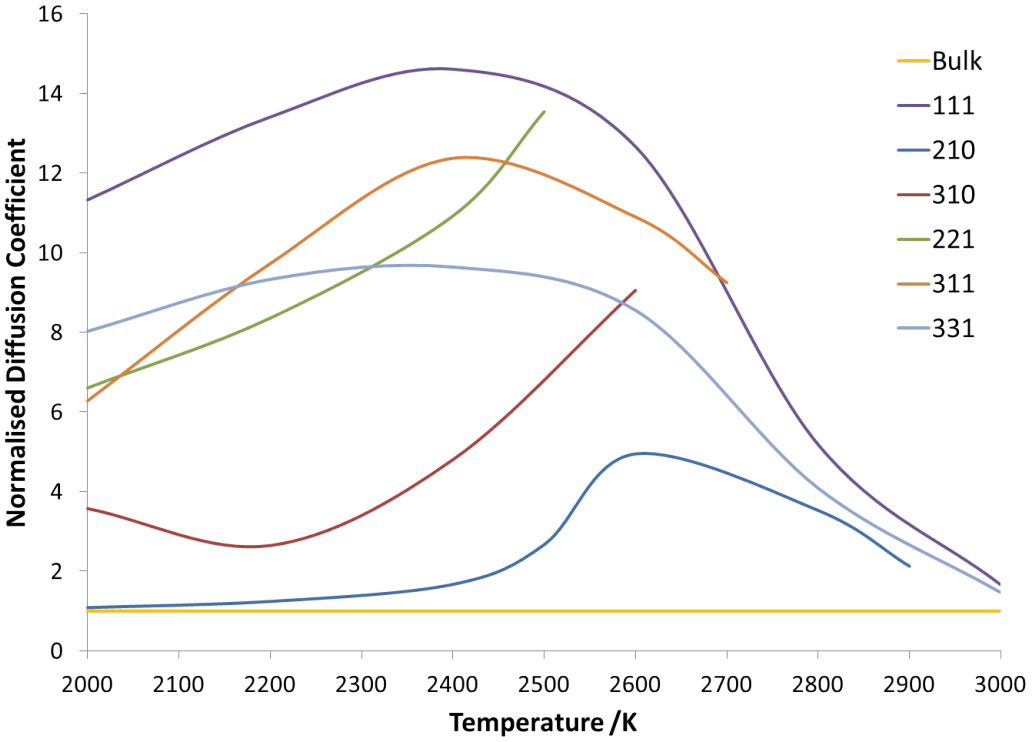

Figure 4.17: Average contribution of tilt grain boundaries to normalised diffusion

Figure 4.17 shows the average contribution to diffusion of each grain boundary studied. A line representing bulk diffusion rates is included for clarity. Diffusion data in this plot was only collected at temperatures where the systems were deemed to be stable with respect to grain boundary diffusion. All grain boundaries predicted diffusion rates to increase with temperature but between 2400 K and 2600 K all systems showed a reduction in normalised diffusion coefficients with convergence to bulk values predicted to occur at temperatures just over 3000 K, assuming the boundaries could be stabilised at this temperature. This was a result of the increasing amounts of fast ionic diffusion taking place at both the boundary and in the bulk. It was suggested in chapter 3 that fast ionic diffusion rates may be independent of defect concentration, if so it might be assumed that the same mechanism applies for large extended defects. All boundaries are seen to have varying effects on the normalised diffusion coefficient with the greatest effect coming from the $\Sigma 3(111)$ system which also happens to have the lowest energy of the boundaries and generally the smallest boundary width. The lowest boundary diffusion was seen in the $\Sigma 5(210)$ boundary which showed virtually no increase in diffusion rate when compared to the bulk until 2500 K where the effect of the structural change can clearly be seen on the diffusion plot as a sudden sharp

increase.

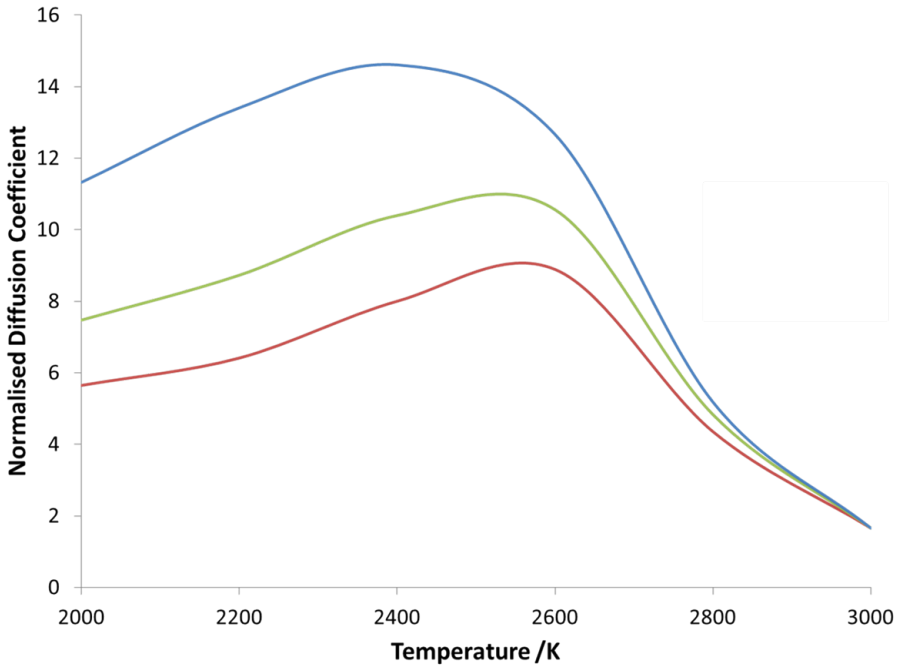

Figure 4.18: Total normalised diffusion as a function of temperature when the polycrystalline sample is cooled quickly (red), at moderate rate (green) and slowly (blue).

We can also infer the effect of grain boundaries on transport in polycrystalline samples. This can be achieved by considering three possible scenarios as shown in Figure 4.18. In the first case we assume that the system is cooled quickly after annealing; in this instance the system consists of largely spherical grains with equal numbers of all boundaries. In the second, the system is cooled in a way that the grains are formed with shapes that are related to the formation energy of each boundary. In the third case the system cooled slowly after annealing and thus the polycrystalline system is dominated entirely by the most stable grain boundary, the $\Sigma 3(111)$. The results suggest that when the system is cooled quickly it may have a lower normalized diffusion ratio than a system which is cooled slowly. Whilst these models do not allow for any variation in grain sizes, we have already demonstrated that boundary diffusion is enhanced when compared to the bulk and as a result the smaller the grain the larger the predicted effect.

4.3 Summary

In this chapter we describe the investigation of the effect of different grain boundaries and grain boundary structure on oxygen diffusion in UO_2. In doing so we generated six different tilt grain boundaries, significantly expanding the range of tilt boundaries studied compared to any previous work and investigated the structure and stability of these interfaces in UO_2. Molecular dynamics was also used to determine the effect of these interfaces on oxygen diffusion. Structural investigations using energy minimisation predicted higher Σ tilt boundaries to be less stable than lower Σ boundaries however, in practice all grain boundaries were stable at the temperatures studied with no cleavage or reforming of bulk observed. Boundary instability was observed in some cases in the form of boundary movement but was only detected at higher temperatures for certain boundaries. The only real implication of this boundary movement was to make the determination of oxygen diffusion in these systems impossible. As part of the investigation tilt boundaries were annealed. This process resulted in structural changes to two of the six grain boundaries and indicates that when investigating these systems the structures predicted by energy minimisation cannot be whole relied upon as the lowest energy grain boundary structure.

At temperatures between 2000 K-3000 K all tilt grain boundaries studied significantly enhance the diffusion of oxygen in UO_2. Oxygen diffusion was not only enhanced at the grain boundary but the presence of these interfaces caused an enhancement of diffusion rates in the bulk region surrounding the interface. However the effect of each different tilt boundary on oxygen diffusion varies substantially depending on the structure of the system being studied. Variations in diffusion behaviour manifest as variations in diffusion width, relative intensity and the shape of diffusion profiles. The dependence of structure on diffusion is illustrated by the $\Sigma 5(210)$ boundary which undergoes a phase change to a metastable state at 2400 K. At temperatures below this very little enhancement of diffusion is observed however the change of phase facilitates an increase in normalised diffusion rates. The influence of structure means that in a polycrystalline system, not only will the oxidation of the fuel be dependent on grain size but also on grain type.

Temperature also has a significant effect on diffusion behaviour as the general trend for all boundaries was for the average normalised diffusion to increase until temperatures around 2600 K where the relative enhancement of diffusion in the grain boundaries gradually de-

creases. This decrease is a result of increased diffusion in the bulk reducing the normalised diffusion rates so at high temperatures the contribution of grain boundaries to diffusion in polycrystalline systems is less significant. It is likely that if grain boundaries were studied at temperatures where the entire system is experiencing fast ion diffusion then the difference in diffusion rates between the bulk and boundary would be negligible.

The directional dependence of oxygen diffusion also varied greatly with structure and temperature. Some systems displayed mainly isotropic behaviour while others were heavily anisotropic. This varying degree of directional dependence also varied with temperature with the only constant being at the highest temperatures where the system is tending towards fast ion diffusion. At this point oxygen moves almost freely throughout the system and behaviour is generally isotropic.

Chapter 5

Twist Grain Boundaries

As crystals grow there is an increasing chance that grain boundaries will come together at different angles, forming twist grain boundaries. As a result these boundaries may be more representative of real grain boundaries and afford more insight into oxygen transport processes in UO_2. To date little work has been done on twist boundaries (see Chapter 1) and virtually all atomistic simulations of grain boundaries have focused on tilt boundaries. Part of the problem is that as yet there is no robust protocol for generating such boundaries.

This chapter describes our approach for generating twist grain boundaries in UO_2 in addition to their potential as diffusion pathways for oxygen migration. Discussion centres on the $\Sigma 3(111)$ and $\Sigma 11(311)$ systems with the initial focus on the process involved in generating the configurations, looking at different methods of constructing the boundaries utilising varying rotation angles and surface terminations in order to simulate both stoichiometric and reduced density systems. In each case energy minimisation and molecular dynamics was used to determine the stability of the systems with respect to temperature. Finally oxygen diffusion along these twist boundaries is then compared with similar investigations for tilt grain boundaries.

5.1 Coincident Site Lattice Theory

Coincident site lattice theory describes the degree of coincidence (given by Σ) between the structures of two differently orientated crystals. To generate twist grain boundaries two

surfaces are brought together with one surface rotating with respect to the other around the axis perpendicular to the plane of the surfaces. Twist boundaries built from identical surfaces can be considered as a pair of 2D square lattices. It is desirable to find twist boundaries with angles that give good coincidence, as this ensures the two surfaces match and there will be minimal strain. The coincidence is given by

$$\left(\frac{a_1}{a_2}\right) = \frac{k^2+l^2}{m^2+n^2} \tag{5.1}$$

where a_1 and a_2 are the lattice parameters of grain 1 and grain 2 respectively. k, l, m and n are integers. The angle of rotation (θ) for this coincidence is given by

$$\theta = \theta_1 \pm \theta_2 = \tan^{-1}\left(\frac{l}{k}\right) \pm \tan^{-1}\left(\frac{n}{m}\right) \tag{5.2}$$

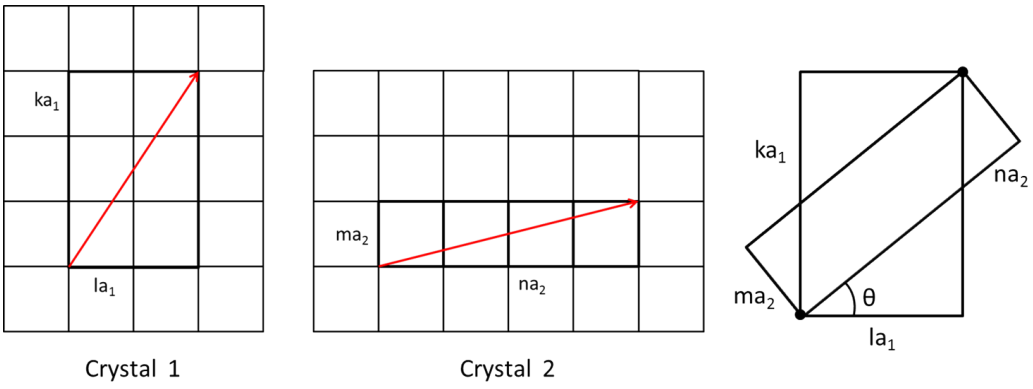

Figure 5.1: A schematic showing how a coincident site boundary of angle θ can be formed by two crystals with the lattice parameters a_2 and a_1

For 2D square coincident site lattices two angles will be seen for each set of l, k, m, n. If the lattices have some degree of rotational symmetry equivalent interfaces are described by both negative and positive values of θ. The inverse density of coincidence (Σ^p) for grain 1 and grain 2 is given by

$$\Sigma_1^P = m^2+n^2 \tag{5.3}$$

$$\Sigma_2^P = k^2 + l^2 \tag{5.4}$$

where Σ^P indicates a 2D planar coincidence as opposed to a 3D planar coincidence [174]. The fractional number of ions that are coincident between the grains is given by $1/\Sigma^P$. Exact coincidence can only be achieved if equation 5.1 is completely satisfied. Clearly it is possible to consider performing this operation and there being some residual strain, i.e. equation 5.1 is not entirely satisfied. Thus the first step is to identify the constants (m, n, k, l) that give the least strain.

5.2 Generating Twist Grain Boundaries

METADISE [123] has now been modified by Professor Steve Parker to generate twist grain boundaries. For each boundary a list of potential rotational angles are produced in order from the lowest to highest strain. When selecting a particular angle for study the strain is important as it hints at the likely stability of the boundary. Another important factor in selecting an angle is the area of that particular boundary. Boundaries with large surface areas are problematic as in order to stabilise these structures when used in molecular dynamics simulations at high temperatures we require a large amount of bulk to separate boundaries in the same cell. As a result a large interfacial area means the system will be excessively large and very expensive in computer time.

When a crystal is rotated and attached to a surface one of the main issues that needs to be addressed is how to deal with close, repulsive ion interactions at the grain boundary interface. There are two main ways to resolve this. The first is to perform a scan of one surface relative to another using the same methodology described in chapter 4 for tilt boundaries. The second method is to consider reducing the density at the grain boundary which can be achieved by using different terminations of the same surface.

The two grain boundaries $\Sigma 3(111)$ and $\Sigma 11(311)$ were selected for study as both are type 2 surfaces and as a result are suitable for studying oxygen deficiency in grain boundaries. Additionally both are relatively flat surfaces so that after rotation there is an increased chance of matching the surfaces. In order to investigate the structures of both the $\Sigma 3(111)$ and

$\Sigma 11(311)$ twist grain boundaries there are a number of factors that must be accounted for. Firstly the effect of the angle of rotation was investigated by generating different rotations of the same grain boundary. Two were generated for $\Sigma 3(111)$ and three for $\Sigma 11(311)$. These rotations produced low strain twist boundaries with sufficiently small surface areas. For the $\Sigma 3(111)$ boundary we also investigated the effect of reduced oxygen density by generating the boundary using both oxygen and uranium terminated surfaces.

5.3 Static Lattice Studies

Once the required surfaces had been generated, energy minimisation calculations were performed to determine formation and cleavage energies of the twist boundaries using the methodology described in chapter 2.

Table 5.1: Formation (E_f) and cleavage (E_c) energies for all rotations of the full density $\Sigma 3(111)$ and $\Sigma 11(311)$ twist grain boundaries, also included are similar energy values for the corresponding tilt boundaries.

Grain Boundary	Rotational angle θ /°	E_f /eV	E_c /eV
$\Sigma 3(111)$	21	2.10	0.56
$\Sigma 3(111)$	28	1.90	0.75
$\Sigma 11(311)$	67	3.11	2.78
$\Sigma 11(311)$	95	3.04	2.85
$\Sigma 11(311)$	146	2.58	3.31
$\Sigma 3(111)$	0	0.30	0.52
$\Sigma 11(311)$	0	1.37	4.52

The lowest formation energies were displayed by the full density $\Sigma 3(111)$ twist boundaries with both the 21° and 28° rotations having similar formation energies. The formation energies of the three $\Sigma 11(311)$ twist boundaries were all higher than the full density $\Sigma 3(111)$ boundaries. Of the three the 67° and 95° rotations produced very similar values, however the 146° rotation was predicted to have a lower formation energy than the other two $\Sigma 11(311)$ boundaries. The energies of the tilt grain boundaries were determined in chapter 4. When compared with the corresponding tilt systems the twist boundaries all have significantly higher formation energies suggesting that tilt boundaries would be formed in preference to twist boundaries. Cleavage energies give insight into the potential stability of a grain boundary. Interestingly, the cleavage energies of the tilt and full density twist $\Sigma 3(111)$ boundaries are almost identical whereas the $\Sigma 11(311)$ twist boundaries have higher formation energies

than the $\Sigma 11(311)$ tilt boundaries but the cleavage energy is also lower. This suggests that the $\Sigma 11(311)$ tilt boundaries will be the most stable of all the systems.

The radial distribution functions of all full density systems were calculated to try and identify any significant close like-ion interactions arising as a result of the formation of these twist boundaries to look for a link with cleavage energies. No significant close like-ion distances were found that could explain the trends in cleavage energies.

Table 5.2: Formation (E_f) and cleavage (E_c) energies of the reduced density $\Sigma 3(111)$ twist grain boundaries including the relative change in energy of reduced density systems.

Grain Boundary	Rotational angle /°	E_f/eV	E_c/eV	δE_f /eV	δE_c /eV
$\Sigma 3(111)$	21	3.65	1.34	+1.68	+0.65
$\Sigma 3(111)$	28	3.58	1.41	+1.55	+0.78

Both reduced density boundaries showed very similar formation and cleavage energies with the formation energies of these systems higher than any of the other twist boundaries. The cleavage energies were higher than the full density $\Sigma 3(111)$ grain boundaries but lower than the $\Sigma 11(311)$ twists suggesting they will fall between the two in the order of stability. While cleavage and formation energies are higher than full density systems the relative increase in energy is similar for both 21° and 28° rotations. The most stable $\Sigma 3(111)$ and $\Sigma 11(311)$ surfaces are both oxygen terminated. However the uranium terminated $\Sigma 3(111)$ surface was also used to produce the reduced density boundaries. This surface is higher in energy than the oxygen terminated surface and when energy minimisation is used on the uranium terminated $\Sigma 3(111)$ surface oxygen migrates to the surface as part of the relaxation process.

The relaxed structures of each of the four different $\Sigma 3(111)$ twist grain boundary systems are displayed. Each is shown with the left grain at the same orientation across all the structures to make comparison easier.

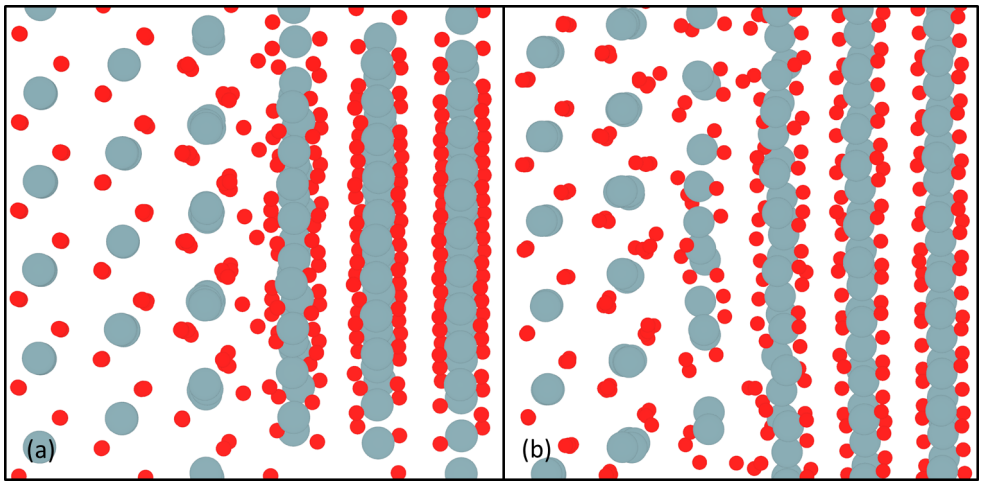

Figure 5.2: 21° grain boundary showing both the full density(a) and reduced density(b) structures. The blue/grey spheres represent uranium ions and red represent oxygen.

In figure 5.2 the full density twist boundary for the $\Sigma 3(111)21°$ is displayed. In a similar manner to the $\Sigma 3(111)$ tilt boundary, very little relaxation is seen particularly among uranium ions. More significant relaxation is seen for the reduced density system however, which shows obvious relaxation two layers away from the interface including more significant deviation of uranium atoms. The structure of this system is seen to broadly resemble the full density boundary with the original structure being adopted as much as possible around the interface but with a reduced density boundary layer between. The interface layer remains low in density after relaxation and no oxygen migrates to new positions in this central layer.

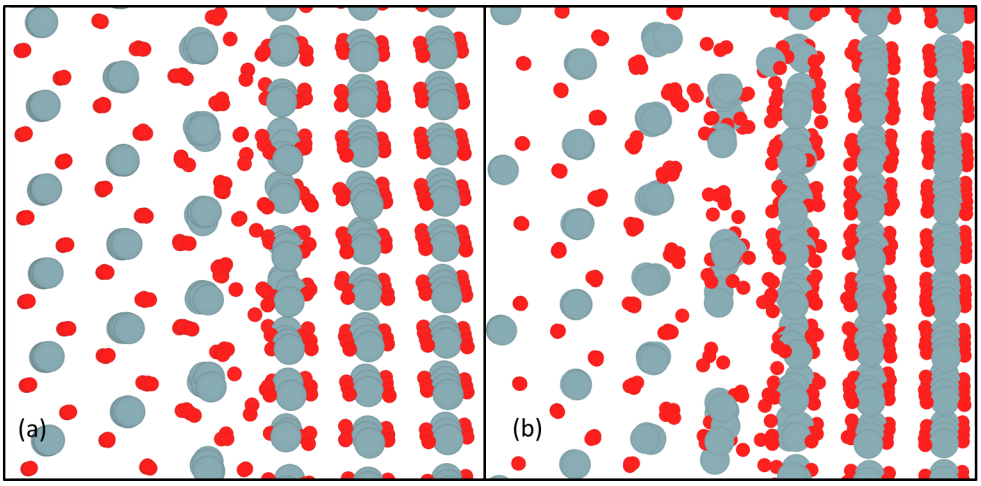

Figure 5.3: $\Sigma 3(111)28°$ grain boundary showing both the full density(a) and reduced density(b) structures. The blue/grey spheres represent uranium ions and red represent oxygen.

Figure 5.3 displays the grain boundary structures for both the full and reduced density $\Sigma 3(111)28°$ systems. The full density structure has a similar structure to the 21° rotation with atomic relaxation only seen at the interface and in the adjacent layers. Greater relaxation is seen for the oxygen atoms than for the uranium atoms. In the reduced density structure either side of the interface the atoms occupy positions broadly resembling those occupied in the full density system with a thin reduced density layer between them that includes a number of voids. The appearance of voids is similar to that found in the 21° reduced density system and suggests that it is energetically favourable for the vacancies to cluster at the interface rather than be distributed throughout the rest of the system.

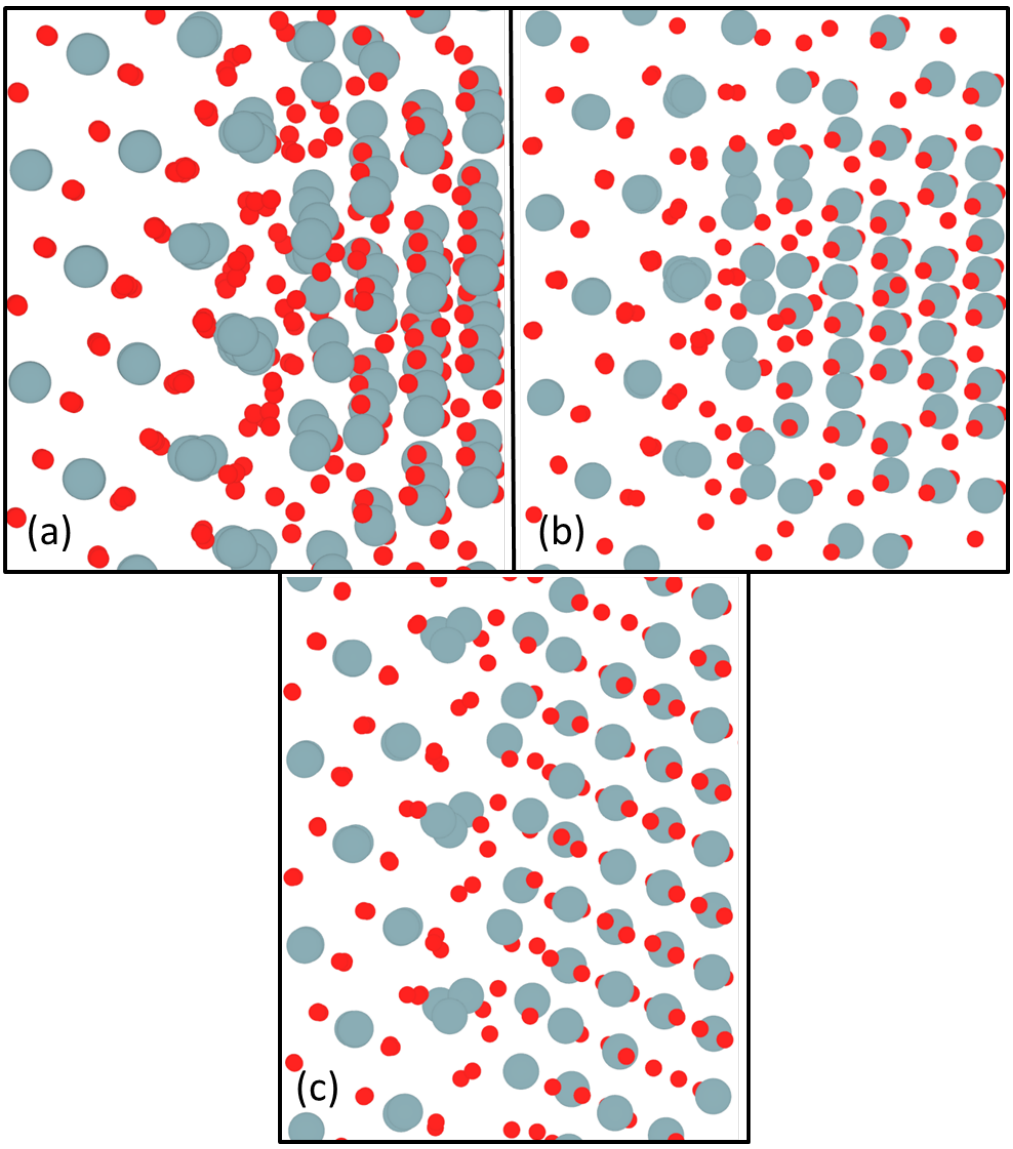

Figure 5.4: Twist grain boundary structures for 67°(a) 95°(b) 146°(c). The blue/grey spheres represent uranium ions and red represent oxygen.

The grain boundaries displayed in figure 5.4 are the three different systems generated for the $\Sigma 11(311)$ twist boundary. Due to the orientation of the two crystals, the structures of the $\Sigma 11(311)$ twist boundaries are not as clear as those seen for the $\Sigma 3(111)$. Each system is shown at an orientation where the left grain is in the same position across all the structures to make it easier to see the different rotations.

Table 5.3: Grain boundary width of relaxation for all rotations of the full density $\Sigma 3(111)$ and $\Sigma 11(311)$ twist boundaries

Grain Boundary	Rotational angle θ /°	Width /Å
$\Sigma 3(111)$	0	6.5
$\Sigma 3(111)$	21	10
$\Sigma 3(111)$	28	10
$\Sigma 11(311)$	0	10
$\Sigma 11(311)$	67	11
$\Sigma 11(311)$	95	11
$\Sigma 11(311)$	146	13

Table 5.3 shows the relaxation widths of each of the twist boundaries discussed in this chapter. The grain boundary width represents the distance at which the grain boundary is altering the properties of the material and can be defined in a number of ways. Relaxation width refers to the distance from the boundary in which the interatomic distances differ by two decimal places from those of bulk UO_2. Both the 21° and 28° rotations of the $\Sigma 3(111)$ twist boundary have boundary widths of 10 Å . This is the shortest width of any of the twist grain boundaries. The corresponding tilt boundary (see Chapter 4) showed relaxation over a distance of only 6.5 Å suggesting why the twist boundaries might be less stable. The reduced density systems and in particular the 28° reduced density system showed significantly more relaxation than the full density systems. Of the $\Sigma 11(311)$ twist boundaries all three showed similar amounts of relaxation although the 146° rotation did cause slightly more distortion of the structure than the other two boundaries nevertheless, all three were slightly wider than the $\Sigma 11(311)$ tilt. As no reduced density boundaries were studied for the $\Sigma 11(311)$ twist boundary it is not possible to compare with the reduced density $\Sigma 3(111)$ boundaries. However very little difference was seen in relaxation widths between the full density $\Sigma 3(111)$ and $\Sigma 11(311)$ grain boundaries. There is a broad correlation between the width of each grain boundary and the formation energies described in table 5.1 with the only exception being the $\Sigma 11(311)146°$. Generally the lower the formation energy of the grain boundary the shorter the grain boundary width will be. The likely reasoning for this correl-

ation is that higher energy grain boundaries will cause greater relaxation in the surrounding bulk region in order to stabilise the grain boundary.

Table 5.4: Grain boundary width of relaxation for all rotations of the reduced density $\Sigma 3(111)$ twist boundaries

Grain Boundary	Rotational angle θ /°	Width /Å
$\Sigma 3(111)$	21	13.0
$\Sigma 3(111)$	28	18.0

5.4 Molecular Dynamics Studies

The molecular dynamics code DL_POLY [173] was used to anneal the boundaries to determine the stability and then calculate the transport properties of oxygen at the twist boundaries. In a similar way to the tilt boundaries discussed in chapter 4 the electrostatic interactions of the system were evaluated using the Ewald method to a precision of 10^{-5} and the potential cut-off was 15 Å. All simulations were run with a timestep of 1 fs and with the Nosé-Hoover thermostat/barostat. The simulation cells of grain boundary configurations comprised two boundaries running in opposite directions equally spaced by a bulk region so that the effect of the relaxation of one boundary due to the mismatch is negligible on the other boundary and on the middle of the bulk region.

All systems were equilibrated at 300 K in the NPT ensemble for 1ns until fluctuations of the configurational energy were negligible. Annealing at high temperatures was performed for each configuration and the stability of each boundary with respect to temperature will be discussed in the results section. The temperature was increased up to 3000 K and decreased back to 300 K in the NST ensemble for up to 1ns in a series of stepped runs in order to reach stable grain boundary structures in the temperature range of interest. These most stable configurations were then run at temperatures ranging between 2000 K and 3000 K every 100 K in the NST ensemble for 1.1 ns until the fluctuations in the volume and energy at that temperature were negligible. Following this each structure was run again at the same temperature however, this time utilising the NVT ensemble to obtain oxygen diffusion data.

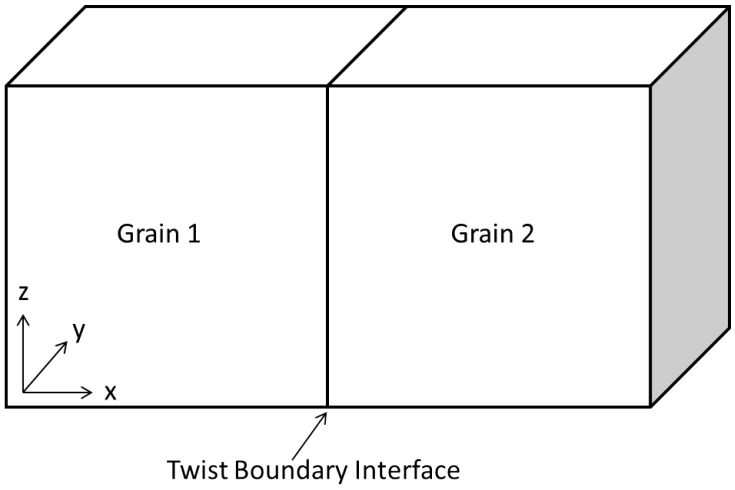

Figure 5.5: Schematic of twist grain boundary MD simulation cell showing directionality

Grain boundary diffusion data was collected using the NVT ensemble over a time of 1 ns (following 100 ps equilibration) for the twist boundary systems. In order to determine oxygen diffusion behaviour at the grain boundary the simulation cell was divided into slices or bins parallel to the grain boundary plane with the width of each bin equal to the U-U interatomic distances in the X direction in the same way as for tilt grain boundaries (see chapter 4). In each slice the 3 components (D_x, D_y and D_z) of the diffusion were calculated and normalized to the bulk values to give an indication of any relative increase/decrease in the diffusion. Bulk oxygen diffusion coefficients range from $5.4\text{x}10^{-14}$ m^2 s^{-1} at 2000 K to $2.93\text{x}10^{-10}$ m^2 s^{-1} at 3000 K. Atomic densities were also calculated by dividing up the cell perpendicular to the boundary with slices 0.1 Å in width.

During the discussion of bulk diffusion results in chapter 3 it was found that oxygen diffusion at high temperatures proceeds via 3 different mechanisms depending on the temperature of study. When investigating oxygen transport in grain boundaries diffusion data will be displayed as diffusion profiles that correspond to diffusion behaviour in each of these regions for each boundary. If a system is not stable at the highest temperatures with respect to grain boundary diffusion then only the diffusion regions in which it is stable will be shown.

5.4.1 $\Sigma 3(111)$

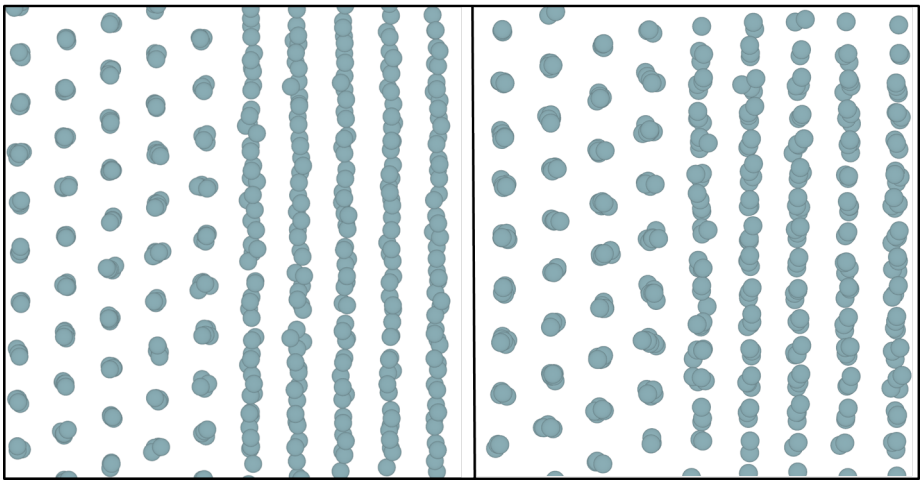

Figure 5.6: Annealed structures of the full density $\Sigma 3(111)$ grain boundaries at (a) 21° and (b) 28° showing only uranium ions.

In the previous section (5.2) four variations on the $\Sigma 3(111)$ twist grain boundary were discussed. The annealed structures of the two full density $\Sigma 3(111)$ boundaries are displayed in figure 5.6 with oxygen atoms removed. In both cases there appears to be little if any difference between the annealed and relaxed structures of these grain boundaries. This implies that energy minimisation represents a sensible tool for generating starting configurations.

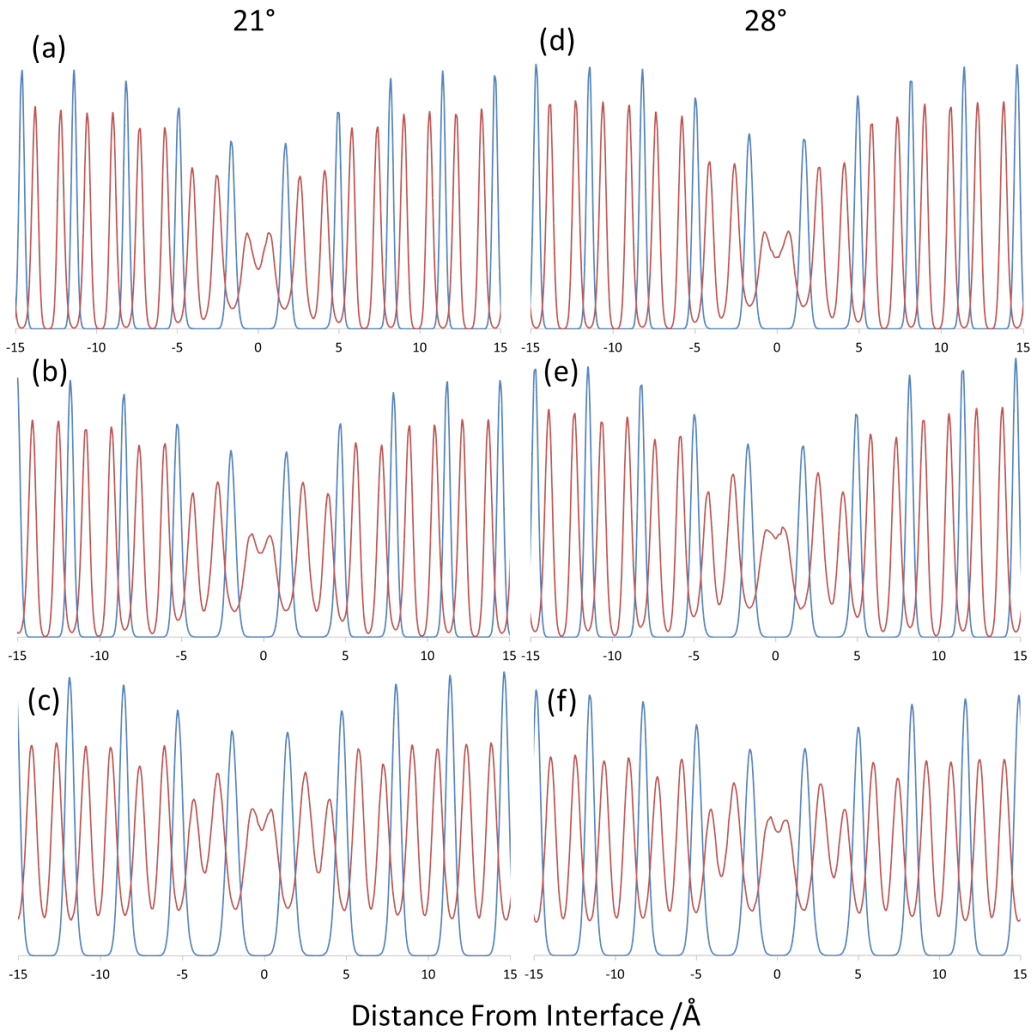

Figure 5.7: Normalised density plots for 21° rotations of the $\Sigma 3(111)$ twist boundary at (a) 2000 K, (b) 2600 K, and (c) 3000 K alongside the 28° rotation of the $\Sigma 3(111)$ twist boundary at (d) 2000 K, (e) 2600 K, and (f) 3000 K. Uranium density is described by the blue peaks and oxygen by the red.

Normalised density plots for the $\Sigma 3(111)$ twist boundaries are shown in figure 5.7. In general the density profiles of the two twist boundaries appear almost identical and this combined with the similar boundary energies described in section 5.2 suggest that both boundaries will exhibit very similar behaviour. In each case no structural changes are observed as the system temperature increases and the only visible change in the density profiles is a slight broadening of the peaks associated with increased movement of the atoms in the configuration which is to be expected at higher temperatures. The presence of sharp uranium peaks over this temperature range indicates that this system was stable over the full range

of temperatures with respect to grain boundary diffusion. The boundary width determined from the density plots suggest that the boundary is having an influence on a region up to 8 Å from the interface which is slightly lower than the value of 10 Å obtained from the static lattice simulations.

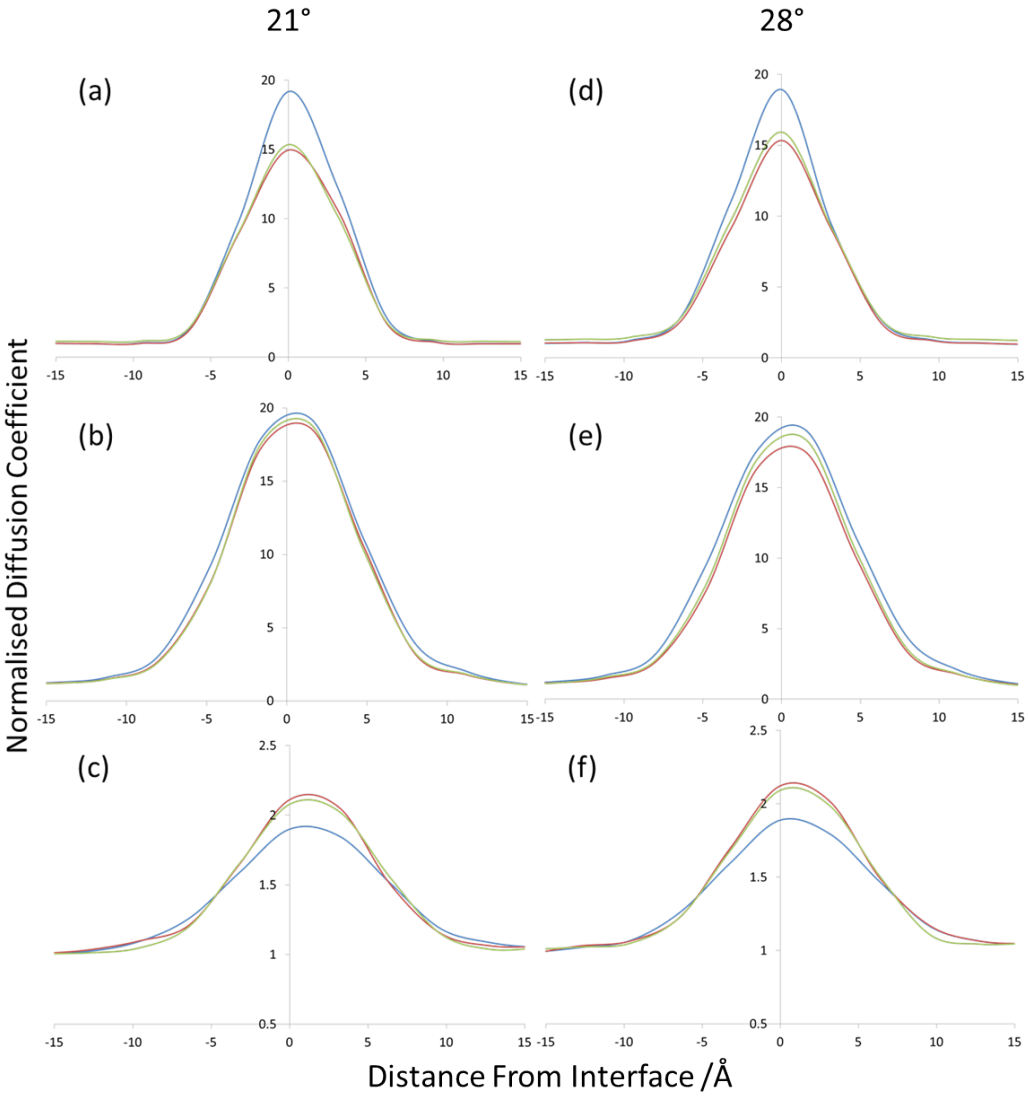

Figure 5.8: Normalised diffusion profiles for 21° rotations of the $\Sigma 3(111)$ twist boundary at (a) 2000 K, (b) 2600 K, and (c) 3000 K alongside the 28° rotation of the $\Sigma 3(111)$ twist boundary at (d) 2000 K, (e) 2600 K, and (f) 3000 K. The X component of diffusion is shown in blue, the Y component in red and the Z component in green.

In a similar manner to density results, diffusion behaviour in the both boundaries follow a very similar pattern. At 2000 K the mobility of oxygen at the grain boundary interface is greatly enhanced at distances of up to 9 Å on either side of the interface. This value is

slightly higher than that determined from the density calculations but also slightly lower than the value predicted by relaxation. In both cases oxygen diffusion is highest directly at the interface and gradually decreases with distance. Normalised diffusion is in each case anisotropic with the largest diffusion coefficients in the X direction, which corresponds to diffusion that crosses the grains and is up to 19 times faster than in the bulk. Diffusion in the Y and Z directions represents diffusion along the grain boundary plane was lower at about 15 times faster than the bulk. At 2600 K the magnitude of normalised diffusion was higher in the boundary plane at about 19 times faster than the bulk but in this case was isotropic. Additionally at this increased temperature oxygen diffusion was enhanced at a greater distance from the boundary. At 3000 K a dramatic reduction is seen in the normalised diffusion coefficient in all directions. This is a result of enhanced diffusion seen in the bulk regions as the system nears fast ion diffusion behaviour. At this temperature both twist boundaries experience diffusion at the interface which is twice as fast as the bulk. At this temperature normalised diffusion perpendicular to the interface was in fact slightly slower than diffusivity in the boundary plane. The range of calculated bulk diffusion coefficients are listed in Section 5.4.

When heated the reduced density $\Sigma 3(111)$ systems appeared to relax into a configuration that was as similar as possible to the system with full density twist boundaries. However in doing this a severe deficiency of atoms remained at the interface and manifested itself in the formation of bubbles. The fact that the reduced density boundaries formed a configuration as similar to the full density systems as was possible suggests that this is the most stable configuration for this system. The reduced density 21° system showing voids or bubbles is displayed in figure 5.9. A consequence of bubble formation at the grain boundary interface in the reduced density systems was that the resulting uneven distribution of ions made the determination of oxygen transport properties unreliable.

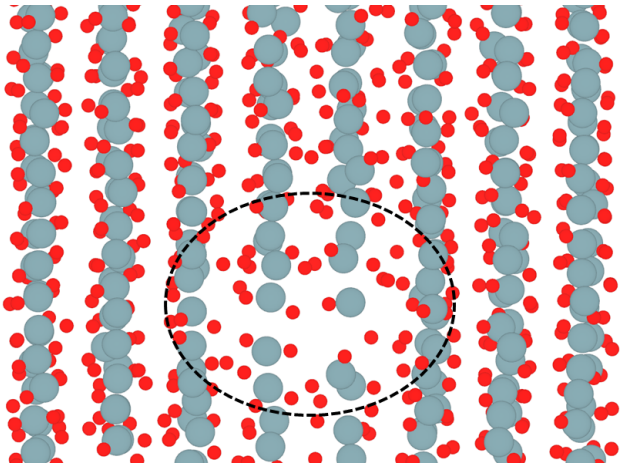

Figure 5.9: Reduced density 21° rotation of the Σ3(111) twist grain boundary showing bubble formation

5.4.2 Σ11(311)

We had generated three different grain boundaries for the Σ11(311) system with rotational angles of 67°, 95° and 146° using energy minimisation.

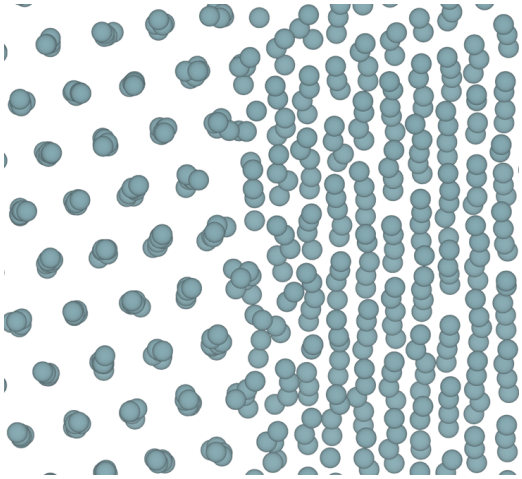

Figure 5.10: Annealed structures of the full density Σ11(311) grain boundary at 67° showing only uranium atoms.

Figure 5.10 shows the annealed structure of the Σ11(311) twist grain boundary at 67°. No annealed structures are shown for the 95° and 146° rotations of the Σ11(311) as they proved to be unstable at the temperatures used in this study. Above 2000 K the grain boundaries diffuse in the X direction i.e. perpendicular to the boundary plane and as a result could not be annealed. However, the 67° rotation was stable over the full range of temperatures.

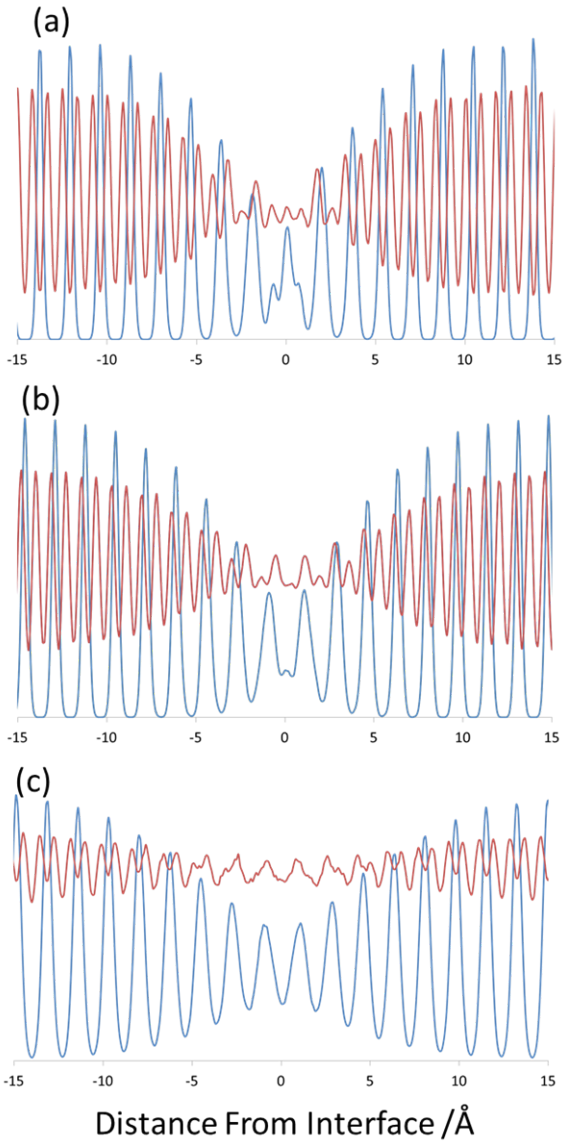

Figure 5.11: Normalised density plots of the $\Sigma 11(311)$ 67° twist boundary system at (a) 2000 K, (b) 2600 K, and (c) 3000 K. Uranium density is described by the blue peaks and oxygen by the red.

The $\Sigma 11(311)$ 67° grain boundary produced sharp uranium peaks over the entire temperature range in this study indicating that this boundary is stable over this range and no grain boundary movement is observed. However the profile of the uranium peaks at the interface do show some slight structural rearrangement. This structural rearrangement corresponds to increased temperature allowing uranium atoms to occupy positions that are unfavourable at lower temperatures. With increasing temperature the intensity of the oxygen peaks is dramatically reduced while troughs are equally increased, implying much more disorder at the interface. At 2000 K a regular ordered density profile showing oxygen peaks cor-

responding to the positions of uranium peaks at the interface is seen but at 3000 K these are replaced with irregular peaks which indicate that oxygen is occupying a large range of different positions.

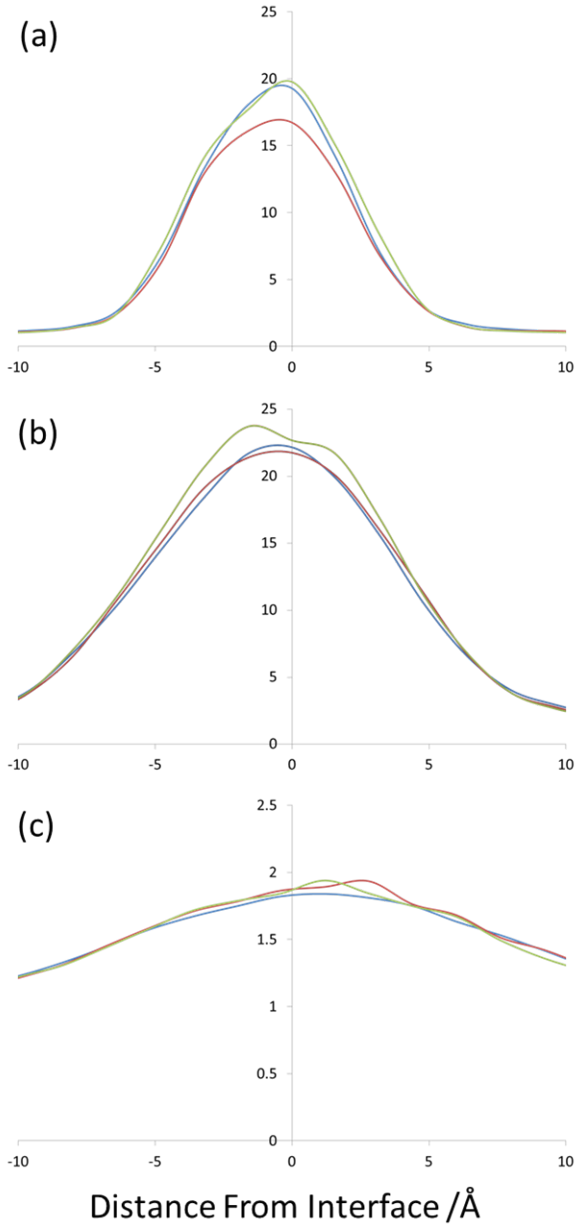

Figure 5.12: Normalised diffusion profiles at (a) 2000 K, (b) 2600 K, and (c) 3000 K for the $\Sigma 11(311)$ 67° twist boundary system. The X component of diffusion is shown in blue, the Y component in red and the Z component in green.

At the lowest temperature studied the $\Sigma 11(311)$ 67° twist boundary exhibits oxygen diffusion rates at the interface up to 20 times faster than in the bulk region. Diffusion is fastest and almost identical in the X and Z directions however the oxygen conductivity in this sys-

tem is slightly anisotropic with a diffusion at the interface in the Y direction being about 17 times faster than the bulk. From the interface the normalised diffusion rate drops gradually to 1 at a distance of 8 Å from the interface. At 2600 K an increase in the normalised diffusion coefficient is seen at the interface with fairly anisotropic behaviour. Diffusion in the Z direction is only slightly higher than X and Y with a value of 23 or 24 times faster than the bulk compared to diffusion about 22 times faster in the X and Y directions. At 3000 K the normalised diffusion profile is anisotropic. A reduction in normalised diffusion rates occurs so that diffusion in the boundary is only slightly higher than in the bulk and a broadening of the area affected by the grain boundary are seen.

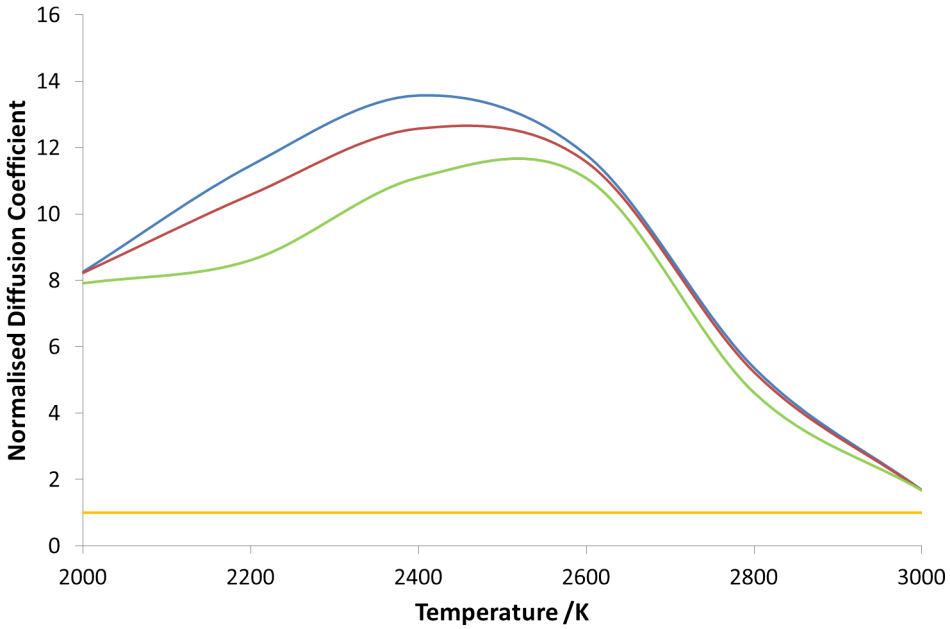

Figure 5.13: Average normalised diffusion of oxygen in twist grain boundary systems. The $\Sigma3(111)21°$ twist boundary is shown in blue, the $\Sigma3(111)28°$ in red, the $\Sigma11(311)$ 67° in green and the bulk in yellow.

The average normalised diffusion coefficient is defined as the sum of all diffusion coefficients calculated in segments relative to the x axis that correspond to diffusion in the grain boundary divided by the grain boundary width. Average normalised diffusion for the two $\Sigma3(111)$ twist boundaries is almost identical as would probably be expected considering the similarities of the two set of diffusion profiles. The $\Sigma11(311)$ 67° twist boundary has a consistently lower average normalised diffusion rate than either of the $\Sigma3(111)$ twist boundaries however, some convergence is seen at 3000 K. All three boundaries show a similar trend of increasing normalised diffusion with temperature followed by a steep decrease at higher

temperatures.

5.4.3 Comparison of Tilt/Twist

The behaviour of both twist boundaries with respect to temperature is similar to simulations of the $\Sigma3(111)$ tilt boundary discussed in chapter 4, which was also stable over this temperature range. Both the tilt and twist boundaries do however display quite different density plots emphasising that they do have different structures.

Diffusion profiles seen for $\Sigma3(111)$ twist grain boundaries are similar in appearance to those seen for the $\Sigma3(111)$ tilt boundary. While the shape of the diffusion profile is similar for the tilt and twist boundaries, as a general rule the normalised diffusion rates in the tilt boundary are slightly higher at the interface over the entire temperature range and the tilt boundary also has a shorter diffusion width causing a smaller region around the boundary to show enhanced diffusion. There are also some differences regarding the directional dependence of the grain boundary diffusion. At 2000 K normalised diffusion in the twist boundaries is anisotropic with fastest rates observed in the X direction corresponding to diffusion across the interface whereas isotropic diffusion is recorded in the tilt system. As the temperature increases diffusion in the tilt system become more anisotropic with diffusion more enhanced in the grain boundary plane (Y and Z directions) while in the twist systems diffusion is isotropic. At 3000 K all three grain boundaries behave similarly with greater enhancement of diffusion in the grain boundary plane as opposed to between the grains. $\Sigma3(111)$ twist systems enhance the oxygen diffusion over a greater area than the tilt boundary.

Average normalised diffusion is shown against temperature for the twist and tilt $\Sigma3(111)$ boundaries in figure 5.14. Unsurprisingly as both twist boundaries produced such similar diffusion profiles, very little difference is noticeable between the average normalised diffusion coefficients. although the boundary with the 21° rotation is predicted to have slightly higher values between 2100 K and 2600 K. Indeed between 2000 K and 2600 K values for the tilt boundary are significantly higher than those for either of the twist systems, although as temperatures increase the lines do start to converge until above 2700 K where the average normalised diffusion is almost identical in all three $\Sigma3(111)$ systems.

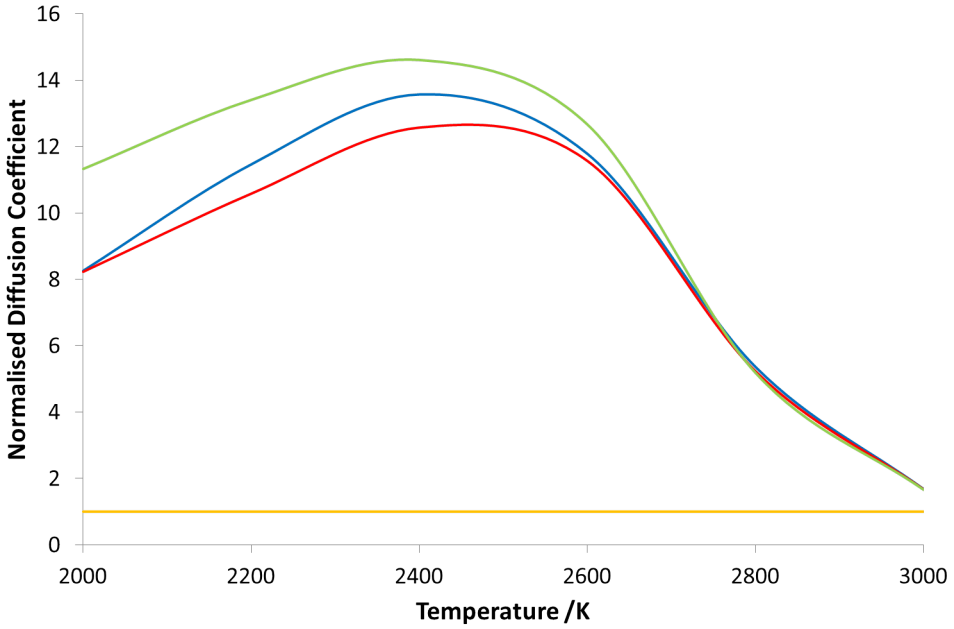

Figure 5.14: Average normalised diffusion of oxygen in tilt and twist $\Sigma 3(111)$ systems. The $\Sigma 3(111)21°$ twist boundary is shown in blue, the $\Sigma 3(111)28°$ in red, the $\Sigma 3(111)$ tilt in green and bulk in yellow.

While the $\Sigma 3(111)$ tilt and twist boundaries showed many similarities in behaviour the same cannot be said for the $\Sigma 11(311)$ tilt and twist boundaries. While it was impossible to anneal the 95° and 146° rotations of this boundary the 67° $\Sigma 11(311)$ twist boundary was stable at temperatures of 3000 K, which is higher than the thermal stability of the $\Sigma 11(311)$ tilt. Increased thermal stability was likely as a result of the very different annealed structures of the two boundaries which could be seen from the normalised density data. The differences between these two boundaries are not limited to structure and stability as the diffusion width of the twist is longer than the 5 Å than is seen in the corresponding tilt boundary at this temperature. The values of the normalised diffusion coefficients for the $\Sigma 11(311)$ 67° twist are in a similar range to those for the tilt boundary, but the tilt system is predicted to enhance diffusion most in the Y direction which is in contrast to the twist boundary. At 2600 K the tilt grain boundary shows faster and more anisotropic diffusion than the twist with oxygen transport in the grain boundary plane 32 times faster than in the bulk whereas diffusion across the interface was only 25 times faster. At 3000 K we cannot compare with the twist and tilt boundary results as the tilt was unstable above 2700 K.

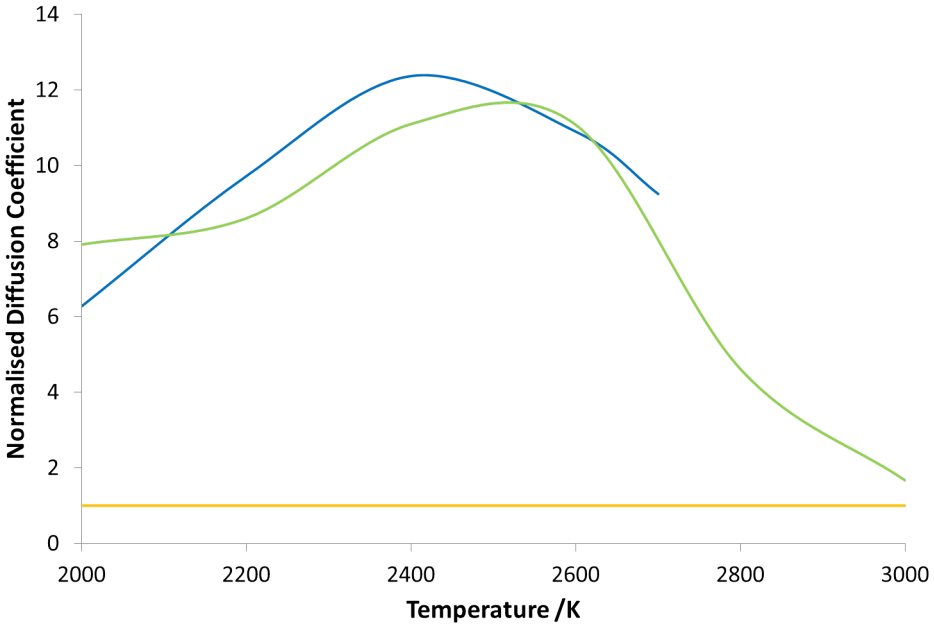

Figure 5.15: Average normalised diffusion of oxygen in tilt and twist $\Sigma 11(311)$ systems. The $\Sigma 11(311)$ tilt boundary is shown in blue, the $\Sigma 11(311) 67°$ twist in green and bulk in yellow.

Average normalised diffusion for the $\Sigma 11(311)$ 67° twist boundary is compared to the $\Sigma 11(311)$ tilt boundary in Figure 5.15. Of particular interest is the comparison with the corresponding tilt grain boundary which is displayed in figure 5.15. At 2000 K the twist boundary's average contribution to normalised diffusion is more significant but this changes at 2100 K where contributions are similar. Above this temperature average diffusion proceeds at a faster rate in the tilt system. This trend continues until 2500 K where once again contributions are similar, no diffusion data was obtained for the tilt system above this temperature due to the diffusion of the grain boundary.

5.5 Summary

A robust methodology has been developed to generate twist grain boundaries using CSL theory. To reduce any like-ion interactions at the interface two different methods were implemented. The first involved scanning the rotated surfaces relative to one another in order to find the lowest energy configuration. Using this method 5 twist boundary structures were developed with 2 based on the $\Sigma 3(111)$ and 3 on the $\Sigma 11(311)$. The second method centred on using a combination of oxygen and uranium terminated surface to reduce the atomic density at the interface. Using this second method two reduced density twist boundaries were generated based on the $\Sigma 3(111)$.

All seven twist grain boundaries survive energy minimisation and in most cases the different rotations of the same structures behaved similarly. Formation energies suggested that the most favourable and therefore the most likely to form were the 21° and 28° rotation of the $\Sigma 3(111)$ twist boundary while the cleavage energies indicated that these two boundaries would be the least stable and the three rotations of the $\Sigma 11(311)$ would be the most stable.

Scanning and minimising the boundaries appears to have removed any significant close range like-ion interactions from all full density boundaries. Reduced density systems adopted a similar structure to the full density boundaries even though there is a significant reduction of oxygen density resulting in a larger volume of free space at the interface. These reduced density systems also have no like-ion interactions at the interface.

The only three grain boundaries that survived annealing using molecular dynamics were the 21° and 28° rotation of the $\Sigma 3(111)$ and 65° rotation of $\Sigma 11(311)$ twist boundary. The other two rotations of the $\Sigma 11(311)$ twist boundary experienced boundary diffusion in the direction perpendicular to the boundary plane at temperatures exceeding 2000 K. The fact that different rotations of the same boundary have different thermal stability shows that we cannot assume investigating one rotation of each boundary is sufficient to describe its behaviour. The reduced density boundaries could not be annealed and in trying to do so voids/bubbles were formed at the interface. We can conclude that the process of scanning twist boundaries is a better method of producing stable interfaces than creating reduced density boundaries using differently terminated surfaces, even though a smaller reduction in density using a more systematic method of removing conflicting atoms would also produce

stable twist boundaries. From annealing simulations we can also conclude that while cleavage energy might predict the energy to produce two free surfaces from a grain boundary it does not allow us to accurately predict which boundaries remain stable at high temperatures.

Density profiles show the $\Sigma3(111)$ twist boundaries have a different structure from the $\Sigma3(111)$ tilt. However this appears to have little effect on the thermal stability as the twist boundaries are stable over the same temperature range as the tilt. While the 67° rotation of the $\Sigma11(311)$ boundary was found to be stable at higher temperatures than the $\Sigma11(311)$ tilt.

Diffusion results for all three stable twist boundaries show that they are fast diffusion pathways for oxygen. In each case normalised diffusion rates increased with temperature and then after reaching a maximum a sharp decrease was seen as diffusion rates in the bulk increased. This decrease was observed up to 3000 K. This behaviour is in line with similar observations for tilt grain boundaries and in fact when compared very little difference was observed between tilt and twist boundaries. Tilt and twist boundaries showed little variation in terms of their relative effect on diffusion rates or on the directional dependence of diffusion. This leads us to conclude that in terms of investigating the effects of grain boundaries on oxygen diffusion in polycrystalline systems it is much simpler to investigate tilt grain boundaries. These are easier to generate, have a similar range of stability and show very little difference in terms of their effect on oxygen diffusion compared to twist grain boundaries.

Chapter 6

Helium Segregation and Transport at Interfaces

Helium is produced throughout the life cycle of nuclear fuels through the α-decay of actinides [175]. The solubility of helium in nuclear fuels is low and can result in some potentially serious consequences including fuel swelling, degradation of thermal and mechanical properties [176] and radionuclide release. In this chapter we present an investigation of the behaviour of helium in UO_2, with particular focus on the role of tilt grain boundaries on the segregation and transport.

The chapter initially considers the development of a robust potential model through the modification of existing potentials. Having established a suitable potential model, the bulk diffusion and defect energies are calculated and compared with available literature values. The segregation and transport of helium in grain boundaries is then investigated. The final part of this chapter reports simulations of helium diffusion at the interface where a grain boundary meets the external grain surface, and thus this requires investigating ways of generating this entirely new type of interface.

6.1 Potential Model

Despite the importance of understanding helium transport in polycrystalline UO_2 relatively few potential models have been derived to model its behaviour. Grimes [177] used embedded quantum cluster calculations to derive a helium potential using the Lennard-Jones functional form and then used it to calculate the solution and migration energies of helium in UO_2. More recently a potential was developed by Yakub et al [109] using the Buckingham form that was used to model helium diffusion as well as its solubility [178].

The problem with the helium potential developed by Yakub et al [109] is that the Buckingham potential becomes unphysical at small distances and hence fails in molecular dynamics simulations at high temperatures. However, as the statically calculated helium solution energies and activation energies of diffusion are reasonable, it is clearly reliable at distances found under ambient conditions. Thus we chose to simply replace it with a Morse curve, by fitting the energies and forces at typical distances found in the lattice.

Table 6.1: Helium potential parameters

Ion Pair	A	ρ	C
$U^{2.4}$ - He	177.8	0.3	0.0
He - He	169.0	0.257	0.58
	D / eV	B / Å	r_0/ Å
$O^{-1.2}$ - He	0.005832832002	1.579521861	3.277878381

By using a Morse curve the chances of unphysically attractive interactions occurring at very close range as a result of helium migrating through the oxide lattice are significantly reduced. Figure 6.1 illustrates both of these curves alongside the Lennard-Jones type potential used by Grimes [177].

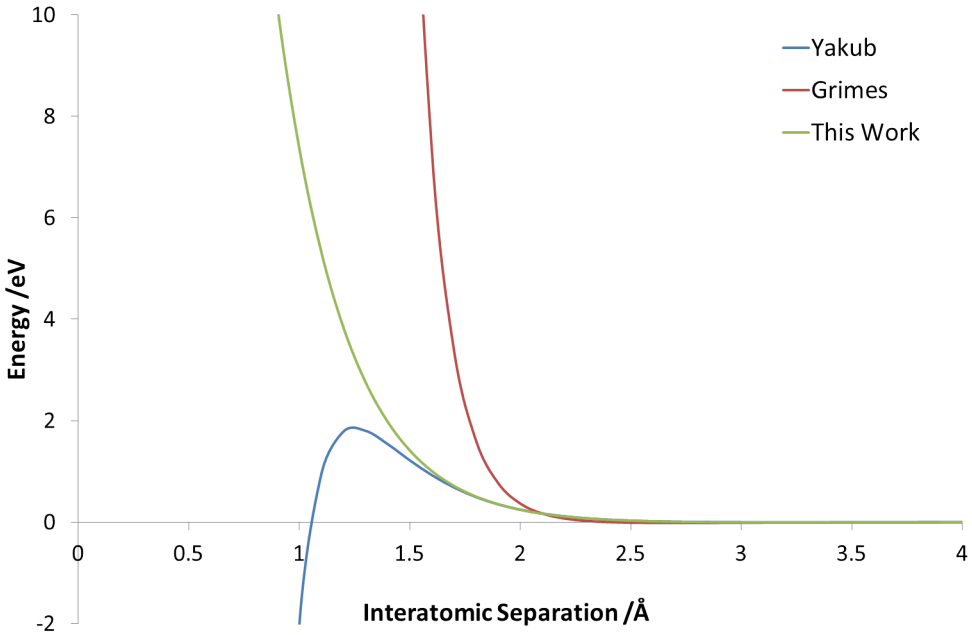

Figure 6.1: Comparison of helium-oxygen potential curves

6.2 Bulk Diffusion Properties

We began using METADISE [123] to evaluate both solution and migration energies for helium in UO_2. These values were calculated using the morl potential for UO_2 developed in Chapter 3, with the helium potential described above are displayed in table 6.2 and compared to those given in the literature. The incorporation energy of helium refers to the energy associated with the addition of a helium atom to an interstitial site. Two different migration energies are listed, the first refers to migration of a helium atom in the [110] direction between two octahedral interstitial sites. This is the most likely migration path in stoichiometric UO_2. The second migration energy represents diffusion in the [111] direction between two octahedral interstitial sites via an oxygen vacancy. This second migration path requires the presence of oxygen vacancies and as a result should have a minimal effect on diffusion in stoichiometric material, however it gives an important guide as to how helium diffusion might be affected by the increased free volume areas produced by stoichiometric defects such as grain boundaries.

Table 6.2: Helium defect and migration energies in UO_2 calculated statically using potential models compared to experimental and DFT values.

Property /eV	Exp	This Work	Grimes [177]	Yakub [109]
Solution Energy	-	0.49	-0.11	0.45
Ea_{Mig}[111] Direction	2.6 [110]	2.6	3.8	2.6
Ea_{Mig}[110] Direction	0.41 [179]	0.39	0.38	0.54

The helium potential in combination with the Morl UO_2 shows very good agreement with experimental values for the activation energy of migration between interstitial sites in the [110] direction. The value predicted is also very similar to the Yakub potential which is not overly surprising as the new helium potential was fitted to the same curve. The Yakub potential however is slightly closer to the activation energy of helium migration via the vacancy assisted mechanism. While both the Grimes potential and the newly derived potential both give very similar values that are marginally lower than experiment. It can clearly be seen from these results that helium diffusion between interstitial sites is greatly enhanced by the presence of oxygen vacancies.

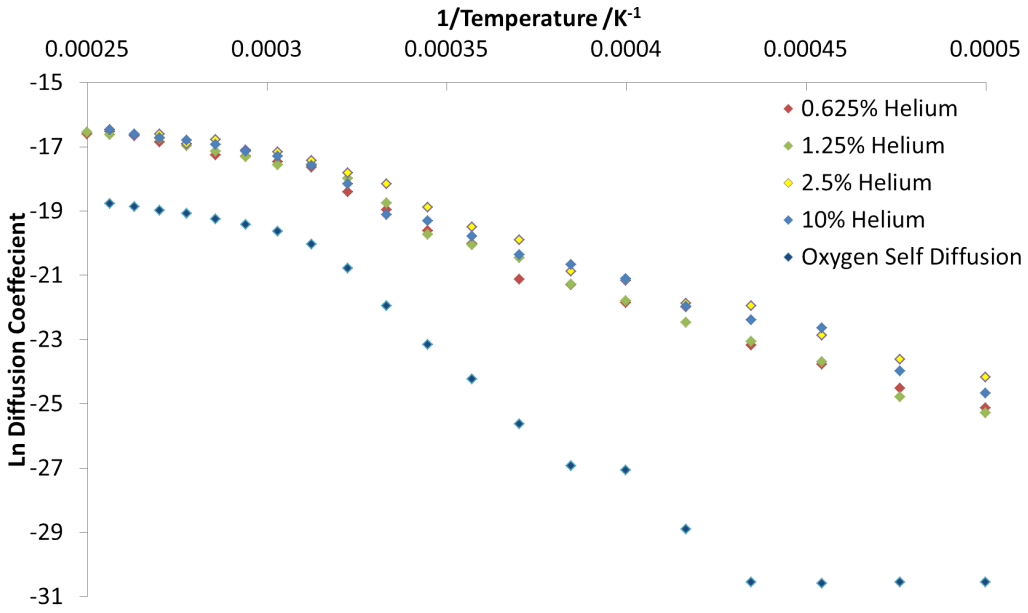

Figure 6.2: Diffusion of helium in bulk UO_2 at concentrations of between 0.625%-10% compared with oxygen diffusion.

The diffusion of helium in bulk UO_2 was calculated using molecular dynamics applying the same procedure to that used for oxygen diffusion (chapter 3). Bulk UO_2 systems were set consisting of a block of 4x4x4 UO_2 unit cells containing 768 atoms. These were initially

run at different temperatures using the NPT ensemble and helium atoms were added to the final structures randomly at percentages between 0.625% and 10%. Diffusion results were obtained from runs in the NVT ensemble over a temperature range of 2000 K-3900 K. In this range simulation temperatures were at intervals of 100 K for each of the different bulk systems. Each simulation consisted of a 100 ps equilibration time followed by a 2ns time period where diffusion data was recorded.

Helium bulk diffusion data is shown in Figure 6.2. Also included is the diffusion behaviour of stoichiometric oxygen which is discussed in depth in chapter 3. Four different helium concentrations were considered as it was expected that by using a higher concentration we should be able to obtain better statistics however, little difference is observed in the results. From this point onwards all molecular dynamics simulations of helium diffusion will be run with a helium interstitial concentration of 10%. Experimental values of helium diffusion constants were recorded as 1.5×10^{-17} m^2 s^{-1} at 1200 K [106], 6×10^{-17} m^2 s^{-1} at 1100 K [111] and 1.2×10^{-18} m^2 s^{-1} at 1100 K [107].

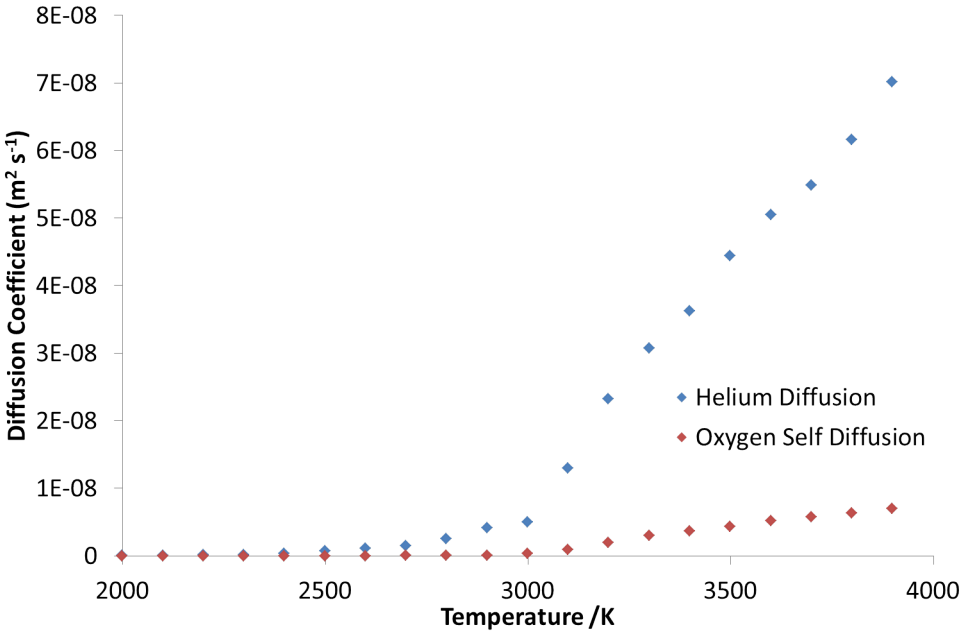

Figure 6.3: Helium and oxygen diffusion showing the effect of superionic transition.

In contrast to oxygen which displays a three region diffusion regime in this temperature range, helium appears to show two region behaviour. In the high temperature region the slope and hence activation energy matches that of oxygen diffusion. This can be seen clearly

in Figure 6.3 and it appears that the high oxygen diffusion rates as a result of fast ionic behaviour cause an increase in the slope of helium diffusion at 3100 K. This is unsurprising as in table 6.2 it has already been demonstrated that the presence of defects will have an enhancing effect on helium diffusion by reducing the activation barrier of diffusion.

6.3 Helium in Grain Boundaries

In chapter 4 we described simulations on six tilt grain boundaries, and now we investigate helium solubility and transport in all six different systems.

6.3.1 Boundary Defects

We began by using METADISE [123] to investigate helium segregation at the grain boundaries. In order to do this we developed a script to locate all voids in the grain boundary systems of 1.7 Å and record their atomic coordinates. The value of 1.7Å was chosen as in system trials it identified correctly interstital sites as well as larger voids at the grain boundary. Helium atoms were systematically placed into the interstitial sites in each of the tilt grain boundaries discussed previously. Energy minimisation calculations were run on each defect position in each boundary to determine the energy of each defect. Energies of defects at the boundary are given relative to the energy of a bulk helium interstitial atom and are displayed in relation to their position perpendicular to the grain boundary.

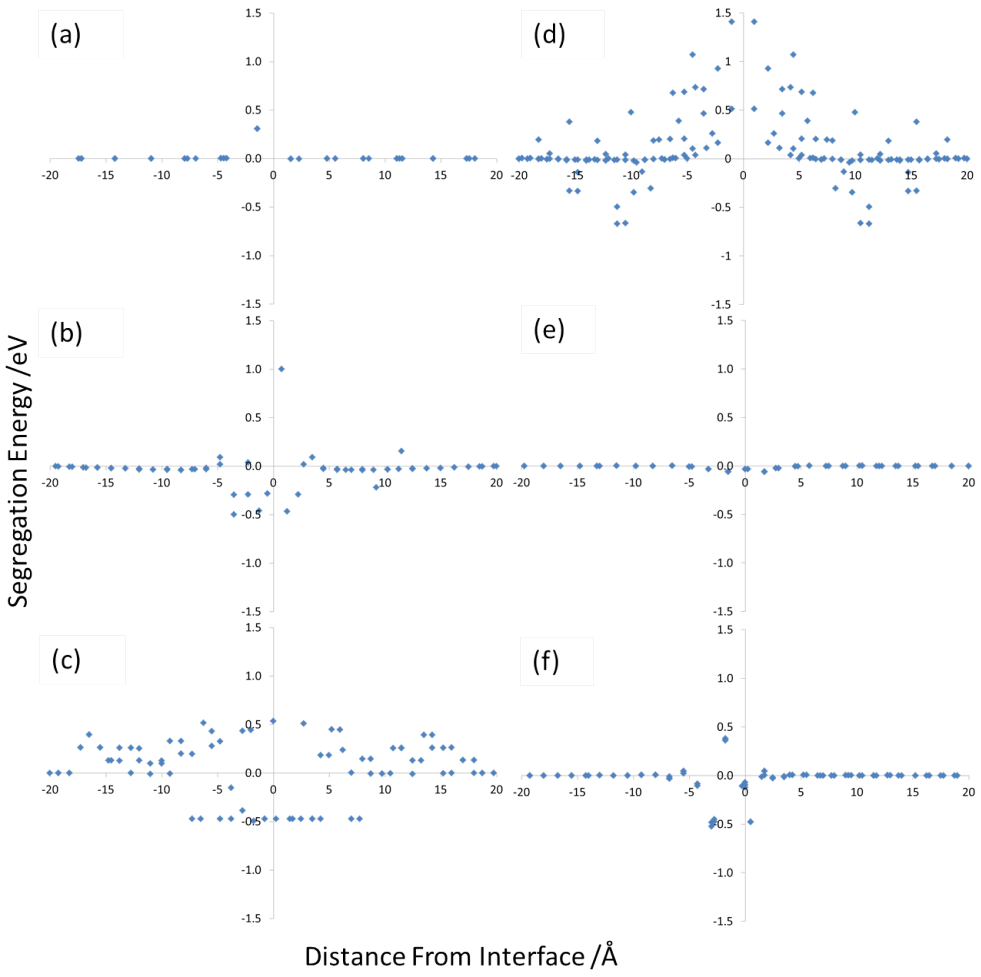

Figure 6.4: Segregation energies of helium interstitial defects in grain boundary systems. (a)$\Sigma3(111)$, (b)$\Sigma5(210)$, (c) $\Sigma3(221)$, (d) $\Sigma5(310)$, (e) $\Sigma11(311)$, (f) $\Sigma19(331)$.

Of the six tilt grain boundaries for which helium interstitial energies were determined four show quite significant variation of defect energy in the vicinity of the grain boundary. It is worth noting that these four systems all showed some stabilisation and some destabilisation of defects with respect to the energies of the defects in the bulk. The $\Sigma3(111)$ and $\Sigma11(311)$ show the least variation in segregation energies in the grain boundary region. The largest destabilisation of any of the defects is seen in the $\Sigma5(310)$ boundary with interstitials up to five times the energy in the bulk and this system also displays a strong degree of asymmetry. This system along with the $\Sigma3(221)$ boundary altered the defect energies over quite a large distance from the boundary and showed, on the whole that the segregation of helium interstitial atoms to the boundary was unfavourable. Whilst defects stabilised with respect to bulk defect energies were observed for all systems except the $\Sigma3(111)$ tilt boundary, the

most consistent stabilisation of helium interstitial atoms was at the $\Sigma5(210)$ and $\Sigma19(331)$ boundaries. In both cases these stabilised defects were located very close to the boundary interface. From these simulations we would expect the $\Sigma5(210)$, $\Sigma3(221)$, $\Sigma5(310)$ and $\Sigma19(331)$ boundaries to show significant segregation.

6.3.2 Boundary Diffusion

Molecular dynamics simulations of helium diffusion in the grain boundaries were performed in a similar manner to the method used to determine oxygen diffusion. Simulations were implemented in the DL_POLY code [173] with electrostatic interactions of the system evaluated using the Ewald method to a precision of 10^{-5} and a potential cut-off of 8.0 Å. A timestep of 1 fs was used with the Nosé-Hoover thermostat/barostat.

The NVT ensemble was used to collect helium diffusion data over a time period of 5ns plus a 10ps equilibration for the grain boundary systems. Diffusion in each of the grain boundaries was determined over slightly different temperature ranges due to the varying thermal stability of different boundaries(as discussed in Chapter 4). The diffusion of helium cannot be calculated as an average over the whole system as large areas of bulk either side of the interface would likely mask any contribution by the grain boundary. So in a similar manner to the method used to determine oxygen diffusion the simulation cell was divided into slices or bins parallel to the grain boundary plane. The width of each bin was equal to the U-U interatomic distances in the X direction i.e. the distance perpendicular to the grain boundary. In each bin the diffusion coefficient was calculated and normalized to the bulk values to give an indication of any relative increase/decrease at the grain boundary. Diffusion constants were determined in three dimensions where, as mentioned above, X corresponds to the perpendicular distance to the grain boundary, Y is the direction of the dislocation pipes and Z is the direction perpendicular to the pipe and parallel to the grain boundary plane. The grain boundary plane is at X = 0 while the positive and negative labels signify 2 sides of the interface which are usually symmetric. Helium diffusion data are displayed for the same temperatures as oxygen diffusion. Bulk helium diffusion coefficients range from $1.92\text{x}10^{-11}$ m^2 s^{-1} at 2000 K to $5.04\text{x}10^{-9}$ m^2 s^{-1} at 3000 K. As previously mentioned each simulation cell contains two boundaries, one in the middle of the cell and one that occupies the cell edge. These interfaces are identical and as result only the boundary at the centre of

the cell is included in the discussion, but clearly a useful way of checking convergence is ensuring that both boundaries display the same properties.

In addition to diffusion data, density profiles are included for each grain boundary to illustrate behaviour. Density data is averaged over the first nanosecond of the simulation. Atomic densities were calculated by dividing up the cell perpendicular to the boundary with slices 0.1 Å in width. In chapter 4 diffusion widths were identified that gave an indication of the distance from the interface in which oxygen diffusion is seen to behave in a different manner to the bulk values. A similar value is determined for each grain boundary relating to the width of helium diffusion.

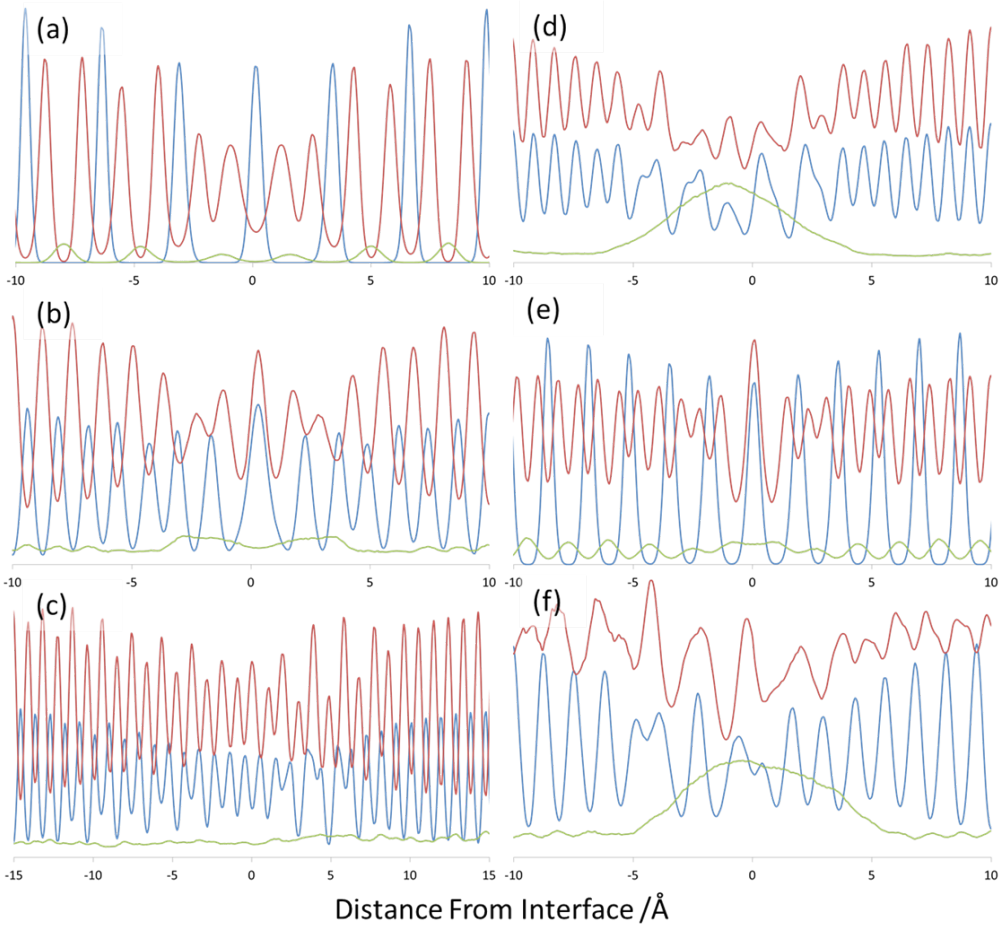

Figure 6.5: Normalised density plots of the tilt boundary systems containing 10% helium at selected temperatures to illustrate unusual behaviour. Uranium density is shown in blue with oxygen density in red, helium density is shown in green. (a) $\Sigma3(111)$ boundary at 2500 K, (b) $\Sigma5(210)$ boundary at 2900 K, (c) $\Sigma3(221)$ boundary at 2500 K. (d) $\Sigma5(310)$ boundary at 2600 K, (e) $\Sigma11(311)$ boundary at 2700 K, (f) $\Sigma19(331)$ boundary at 3000 K.

Density profiles show that the presence of helium in the $\Sigma3(111)$ boundary is having no

effect on the structure of this system at any of the temperatures studied. Helium density in this system is concentrated between the uranium peaks. At the boundary these helium peaks are smaller than in the bulk signifying that helium density is lower at the grain boundary. This boundary is the only system where this phenomenon is observed and it is likely due to the fact that in Figure 6.5 it is the only boundary which does not appear to show any helium segregation.

The density profiles for the $\Sigma5(210)$ boundary also show that the structure of this boundary is consistent whether helium is present or not and the two different phases discussed in chapter 4 are still visible at the relevant temperatures. At the highest temperatures small helium bubbles form although with no significant effect on the structure. The same is not true for the $\Sigma3(221)$ tilt boundary. At low temperatures helium appears to have little effect on the structure of this boundary but at 2500 K a heavy distortion is observed when compared to the annealed density profile. While there does not appear to be any significant structural changes and no bubbles have been formed the presence of helium appears to have destabilised the grain boundary which is diffusing causing the distortion visible in the density profile. For the $\Sigma5(310)$ tilt boundary at low temperatures helium has no effect on grain boundary structure but, at 2600 K the structure is heavily distorted and a broad helium peak residing at the grain boundary indicating the presence of a large bubble causing this disruption. In contrast, normalised density plots suggest that the presence of helium in the $\Sigma11(311)$ isn't causing any alteration of the structures over the temperature range being investigated. At high temperatures a fairly even distribution of helium can be observed with peaks being centred between the uranium arrays and no bubble formation is observed similarly to the $\Sigma3(111)$ boundary. The two normalised density plots for the $\Sigma19(331)$ tilt boundary at the lowest temperatures show that the presence of helium in the system is not having a significant effect on the structure. Small bubbles were observed at 2400 K although these are not obvious from the density plots. A large bubble can be clearly seen at 3000 K which has severely altered the boundary structure.

In terms of segregation, density data show us that of the four boundaries predicted to show segregation by static calculations only the $\Sigma5(310)$ and $\Sigma19(331)$ show significant segregation above the bulk level. Some segregation is also observed to the $\Sigma5(210)$ boundary but unlike our predictions no segregation is seen for the $\Sigma3(221)$. While the $\Sigma11(311)$ and the $\Sigma3(111)$ boundaries show no increased stabilisation of helium interstitials compared to the

bulk.

6.3.2.1 $\Sigma 3(111)$

Helium diffusion profiles for the $\Sigma 3(111)$ tilt grain boundary see (figure 6.6) bear strong resemblance to those seen when investigating oxygen diffusion in the same structure (Chapter 4). Diffusion is highest at the interface and decreases with distance from this point until 7 Å from interface at which point diffusion behaviour is bulk like in character. Across the range of temperatures studied helium diffusion in this boundary was more significant in the Y and Z directions which correspond to the direction of the grain boundary plane as opposed to the X direction. At 2000 K diffusion at the interface is up to 25 times faster than in the bulk which is 5 times faster than was seen for oxygen diffusion at the same temperature. The range of calculated bulk helium diffusion coefficients are listed in Section 6.3.2. As the temperature of the simulation increased the relative enhancement of helium diffusion in the vicinity of the boundary compared to in the bulk is reduced and at 3000 K diffusion is only slightly faster. At 3000 K the system is bordering on the superionic region and when looking at oxygen we see diffusion in the bulk attain a similar rate to that of boundary effecting a large reduction in normalised diffusion rates. Therefore a reduction in normalised diffusion rates of helium at this temperature suggests that the onset of superionic behaviour of oxygen is causing a similar effect for helium.

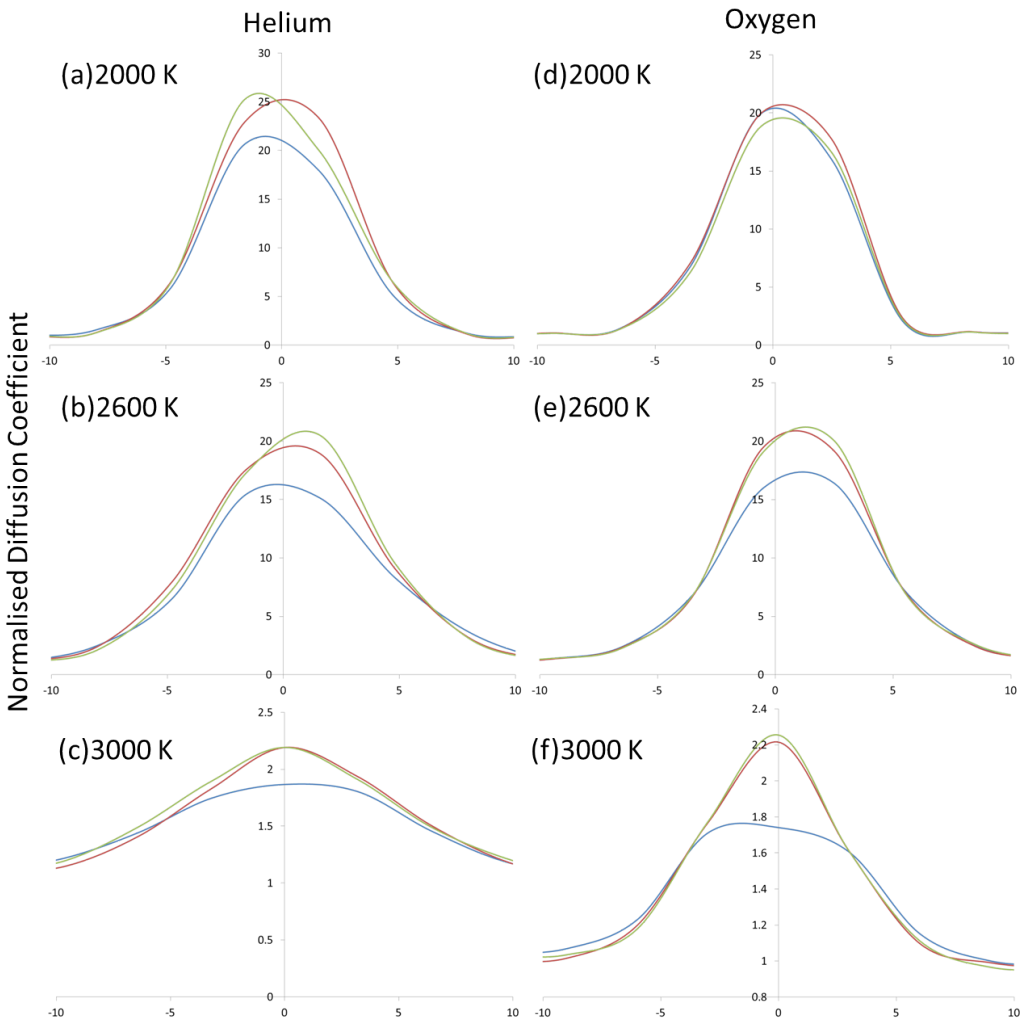

Figure 6.6: Normalised diffusion profiles for the diffusion of helium and oxygen in the $\Sigma3(111)$ grain boundary. The left column shows helium diffusion while the right column shows oxygen diffusion. The X component of diffusion is shown in blue, the Y component in red and the Z component in green

6.3.2.2 $\Sigma3(221)$

At 2000 K the $\Sigma3(221)$ grain boundary shows enhanced diffusion of helium over a distance of 8 Å from the boundary interface which matches 8 Å over which the same boundary enhanced oxygen diffusion. The shape of the diffusion profile bears little resemblance to that of the oxygen diffusion profile until higher temperatures. Unlike the $\Sigma3(111)$ there is much more structure in the diffusion coefficients as a function of distance from the boundary furthermore, whilst both oxygen and helium diffusion are both shown to be fastest in the Y direction the relative rates of diffusion are significantly different (see figure 6.7). Helium

diffusion is as much as 55 times faster at the boundary interface travelling in the direction of dislocation pipes running the length of the boundary. At 2500 K the diffusion profile is disordered and non-symmetric as well as significantly wider. This occurred due to the formation of bubbles at the interface.

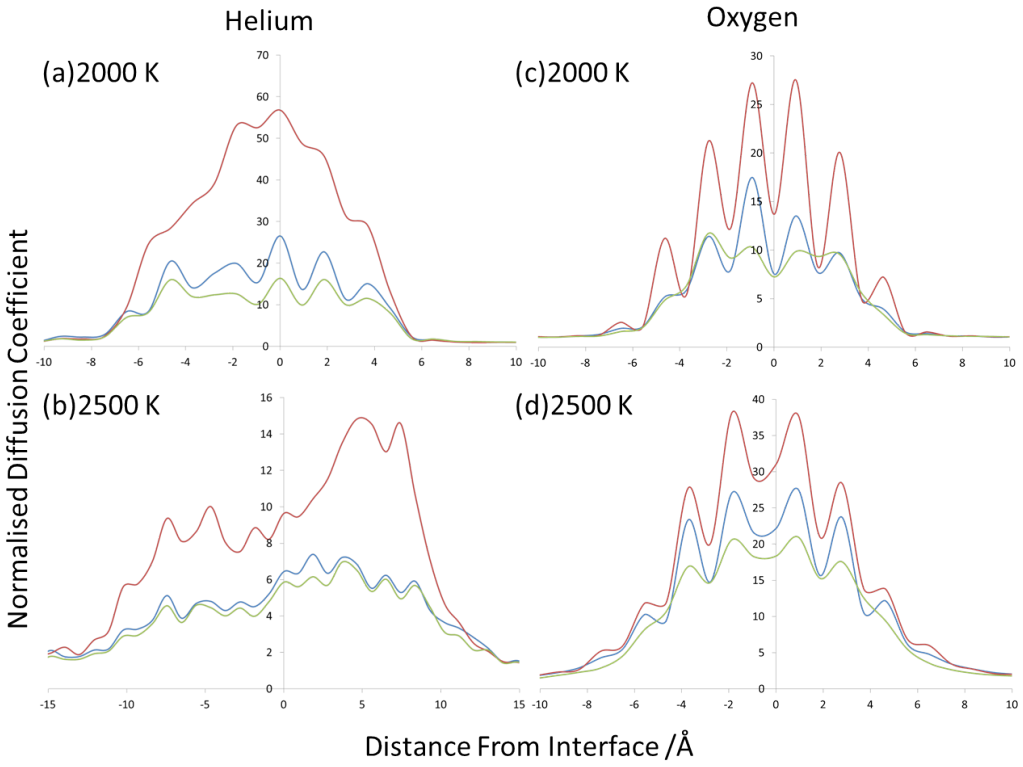

Figure 6.7: Normalised diffusion profiles for the diffusion of helium and oxygen in the $\Sigma 3(221)$ grain boundary. The left column shows helium diffusion while the right column shows oxygen diffusion. The X component of diffusion is shown in blue, the Y component in red and the Z component in green

6.3.2.3 $\Sigma 5(210)$

The normalised helium diffusion profile in the $\Sigma 5(210)$ boundary is highly anisotropic and consists of peaks of variable intensity either side of the boundary interface (figure 6.8). Diffusion along the X direction is over 40 times faster at the boundary than the bulk and diffusion is enhanced in all directions at distances up to 6 Å from the boundary interface. The shape of the profile bears some resemblance to similar studies into oxygen diffusion except for the central peak which is not observed at low temperatures for oxygen. As the temperature increases to 2500 K the relative intensity of the peaks is significantly reduced

relative to that at lower temperatures and whilst diffusion is still most significant in the X direction there is less of a difference between diffusion coefficients in different directions as was seen before. At the highest temperature diffusion behaviour is more isotropic and bears more resemblance to behaviour seen for oxygen diffusion although the relative intensities are higher and diffusion is fastest at the interface and particularly in the Y direction.

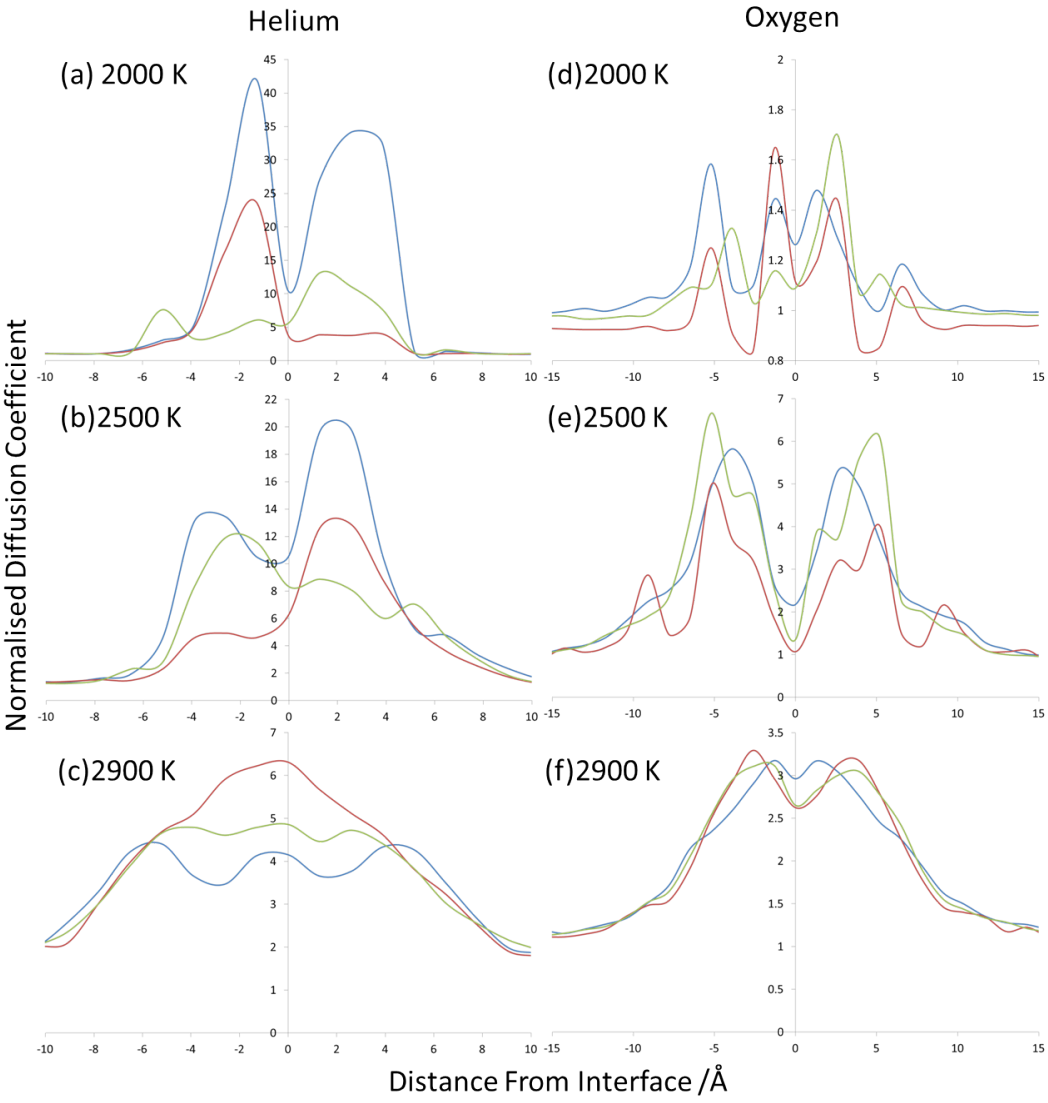

Figure 6.8: Normalised diffusion profiles for the diffusion of helium and oxygen in the $\Sigma5(210)$ grain boundary. The left column shows helium diffusion while the right column shows oxygen diffusion. The X component of diffusion is shown in blue, the Y component in red and the Z component in green

6.3.2.4 Σ5(310)

Helium diffusion in the Σ5(310) grain boundary at 2000 K is displayed in figure 6.9, The shape of the profile bears some resemblance to similar studies into oxygen diffusion except for the central peak which is not observed at low temperatures for oxygen. Helium diffusion is fastest at the boundary interface with the most diffusion seen in the X direction which indicates diffusion between the two grains. In this direction helium diffusion is up to 45 times faster than in the bulk region and enhanced diffusion behaviour is observed at distances up to 9 Å from the interface. At 2600 K the ratio of helium diffusion relative to the bulk is reduced and diffusion is most significant in the z direction although it is difficult to interpret due to the presence of a large bubble.

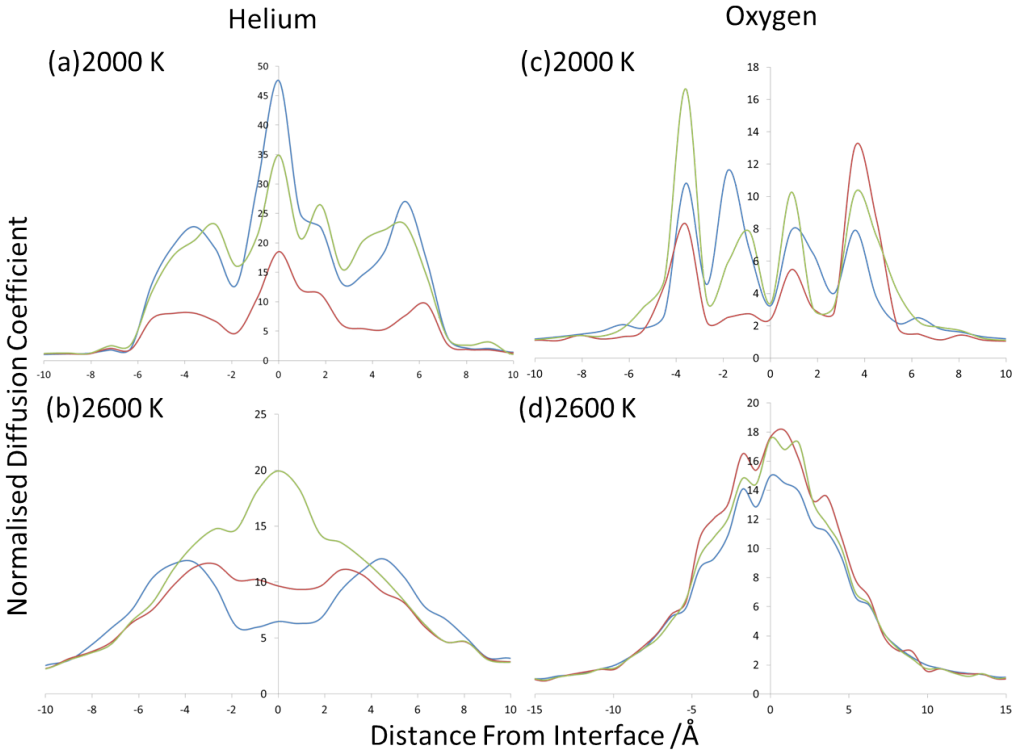

Figure 6.9: Normalised diffusion profiles for the diffusion of helium and oxygen in the Σ5(310) grain boundary. The left column shows helium diffusion while the right column shows oxygen diffusion. The X component of diffusion is shown in blue, the Y component in red and the Z component in green

6.3.2.5 Σ11(311)

Helium diffusion in the Σ11(311) tilt boundary (figure 6.10) at 2000 K is most significant at distances about 2 Å from the interface and in the X direction. At this temperature helium diffusion can be up to 25 times faster than bulk diffusion rates but less than 10 times faster in the Y direction. This is in stark contrast to the isotropic oxygen diffusion seen in the same boundary where normalised rates and diffusion widths are lower. At higher temperatures the normalised rates drop substantially and diffusion in the Y and Z directions more closely resembles oxygen diffusion single peaks centred at the interface while the X component still has the split peak profile seen at lower temperatures.

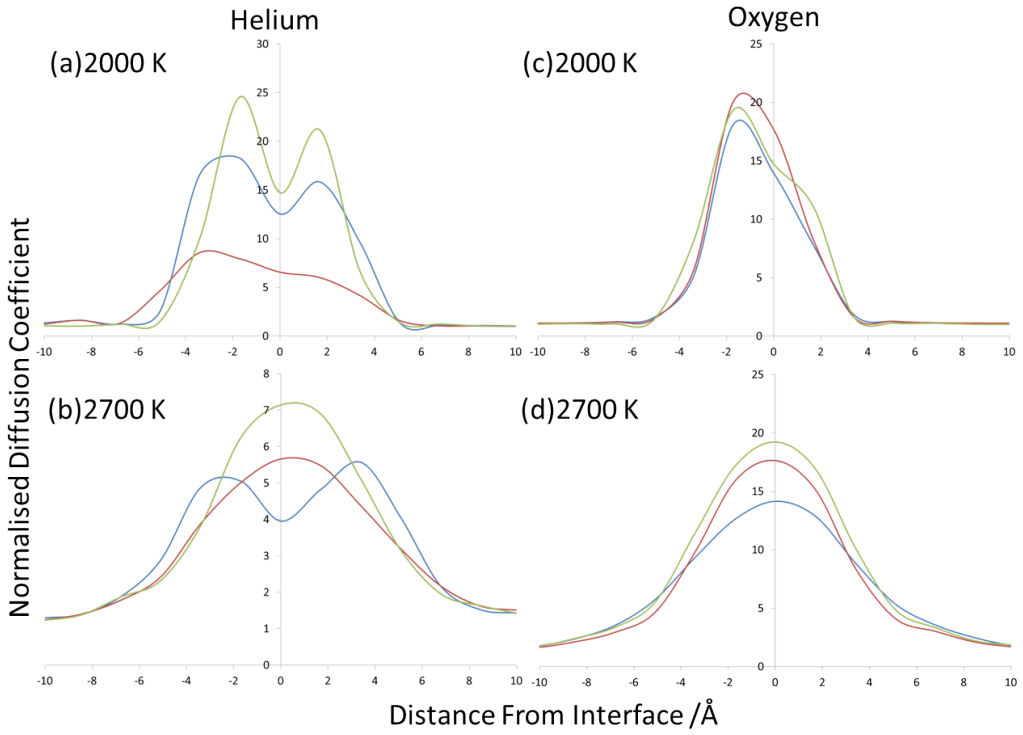

Figure 6.10: Normalised diffusion profiles for the diffusion of helium and oxygen in the Σ11(311) grain boundary. The left column shows helium diffusion while the right column shows oxygen diffusion. The X component of diffusion is shown in blue, the Y component in red and the Z component in green.

6.3.2.6 Σ19(331)

Over the range of temperatures studied we can see from figure 6.11 that helium diffusion in the Σ19(331) grain boundary was consistently faster than oxygen diffusion. Diffusion

of helium, like oxygen was fastest in the Y direction at all temperatures studied. Diffusion rates at 2000 K of 75 times that of the bulk are the fastest seen in any system and correlate well with the very high oxygen diffusion rates also seen in this system. Some similarities can also be seen in the shapes of the helium diffusion profiles to those for oxygen at all temperatures and diffusion widths are similar.

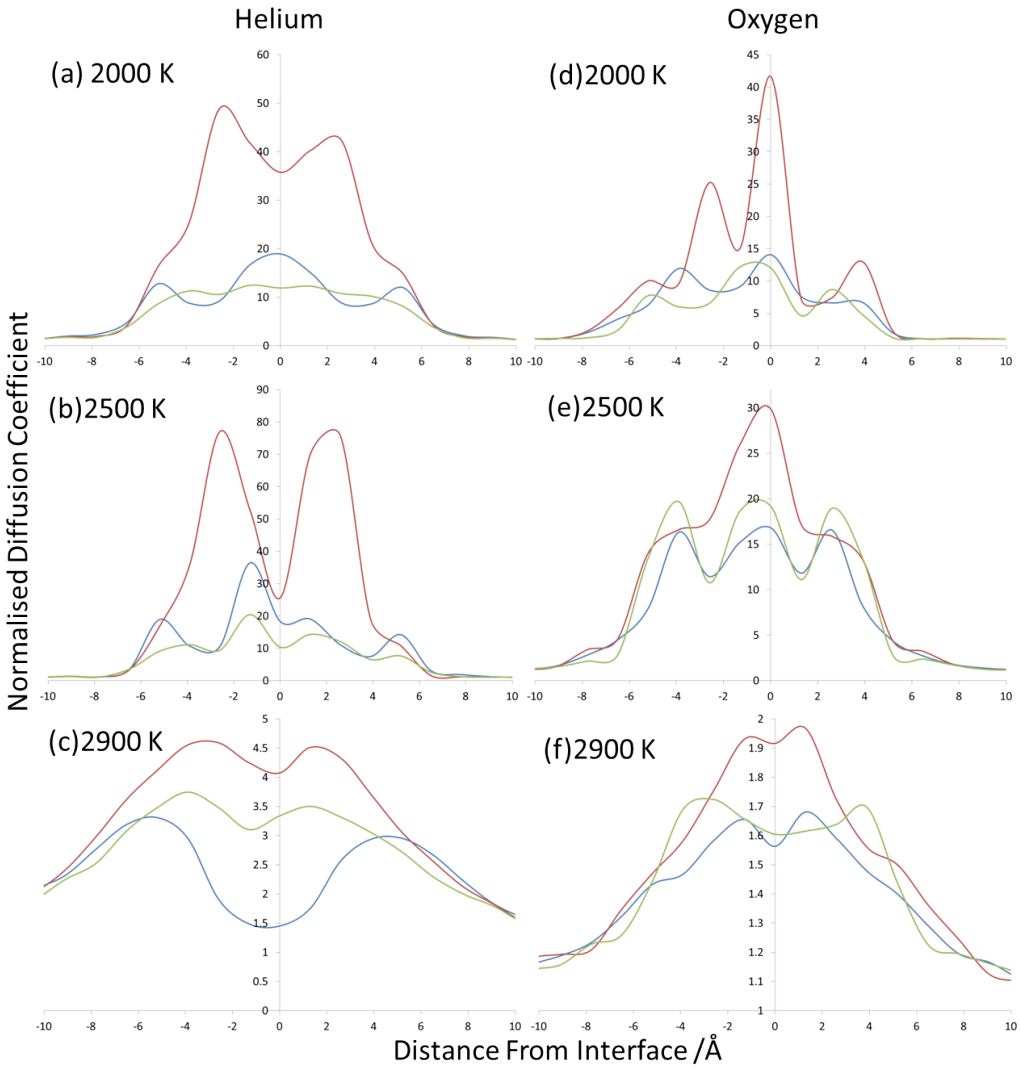

Figure 6.11: Normalised diffusion profiles for the diffusion of helium and oxygen in the $\Sigma 19(331)$ grain boundary. The left column shows helium diffusion while the right column shows oxygen diffusion. The X component of diffusion is shown in blue, the Y component in red and the Z component in green

All boundaries except the $\Sigma 3(111)$ display helium segregation to some degree although variations in behaviour are seen for different grain boundaries. With different systems showing varying degrees of segregation. Density profiles for the $\Sigma 3(111)$ tilt boundary suggest that

the population of helium at the boundary is lower than in the bulk region of the system which suggests that the static calculation of segregation energies give a good indication of how helium will behave in molecular dynamics simulations. At higher temperatures helium bubbles formed at the $\Sigma5(210)$, $\Sigma19(331)$ and $\Sigma5(310)$ grain boundaries during the MD simulations suggesting that there may be a link with segregation energies and even with the free volume at the boundaries. Whilst bubbles only formed at higher temperatures in certain systems it does not necessarily mean they will not form in other boundaries or at lower temperatures as we have studied transport and segregation over fairly short time scales and we do not run simulations for long enough. It is entirely possible that the faster diffusion rates associated with higher temperatures are merely allowing bubbles to form faster.

The segregation of helium to the boundaries does not have an effect on the boundary structure or stability apart from in the $\Sigma3(221)$ boundary where the presence of helium causes boundary diffusion at 2500 K. The other instance where structural damage was seen was due to bubble formation. Particularly in the case of larger bubbles systems where in places the grains were forced apart. It is difficult to discern whether any of the grain boundaries have become saturated with helium as a result over the relatively short time period of these simulations. However it is possible that two of the boundaries that don't form bubbles ($\Sigma3(111)$ and $\Sigma11(311)$) are saturated as both appear to have stable concentrations of helium at the boundary. It would appear that systems which form bubbles are not saturated as they appear to grow quite quickly during the simulations.

Table 6.3: The average normalised diffusion and diffusion width for helium in each tilt boundary determined at 2000 K.

Tilt Boundary	Average Normalised Diffusion	Diffusion Width /Å
$\Sigma3(111)$	9.7	8
$\Sigma5(210)$	9.4	6
$\Sigma3(221)$	14.9	8
$\Sigma5(310)$	11.5	9
$\Sigma11(311)$	9.3	6
$\Sigma19(331)$	16.8	8

In all tilt grain boundaries we see an enhancement of helium diffusion rates in the same manner as was seen for oxygen. Table 6.3 gives average normalised diffusion values as well as diffusion widths at 2000 K for helium diffusion in tilt grain boundaries. From this data we can see that the boundary with the greatest effect on diffusion is likely to be the $\Sigma19(331)$

while the $\Sigma 3(111)$, $\Sigma 5(210)$ and $\Sigma 11(311)$ all have near identical average diffusion rates. However in almost all instances normalised diffusion rates for helium were higher than those seen for oxygen, which considering bulk helium diffusion is faster than bulk oxygen diffusion means that helium in the boundaries is moving significantly faster than oxygen. Moreover, the diffusion profiles of helium did not show any particular resemblance to those produced for oxygen for most boundaries until higher temperatures were reached. This effect is a likely result of higher rates of oxygen diffusion observed at the temperatures in effect creating more oxygen vacancies and assisting the transport of helium.

6.4 Triple-Interfaces

Most of the simulation work carried out on modelling free-surfaces of oxides has focussed on either infinite 2D crystals or occasionally the surfaces of nano particles. Very little work has been directed at simulating the surfaces of polycrystalline materials. This is in spite of the fact that many functional oxides will be polycrystalline. Furthermore the boundaries that terminate at the surfaces of the material are likely to be the fast diffusion path for species to leave and gain entrance to the material. However, as yet there are no routine tools for generating systematically the structure of grain boundaries terminating at the surfaces. In this section, we describe our approach to begin to address this deficiency and in the context of helium diffusion ascertain whether these boundaries do indeed provide the fastest escape route from the oxide layer. These simulation cells that have interfaces between grain boundaries and surfaces we call Triple-interfaces.

The Triple Interfaces (or T-interfaces) we consider here are a development of the tilt grain boundaries which have been discussed in such detail so far. These unique systems enable us to investigate the properties of the interface where surfaces and grain boundaries meet and eventually allow us to explore polycrystalline surface layers. The approach is to simply cut a surface perpendicular to the grain boundary in order to create slabs with grain boundaries running between the two surfaces.

We demonstrate this by taking two grain boundaries; $\Sigma 3(111)$ and $\Sigma 5(210)$. These particular tilt boundaries were selected as they were both stable and when cut perpendicular to the boundary plane produce surfaces that were likely to be the most stable. By selecting these two boundaries we also have one system that has formed helium bubbles in the boundary and one that doesn't. The surfaces created by cutting the system in the (010) direction perpendicular the boundary were the (-211) for the $\Sigma 3(111)$ boundary and (1-20) for the $\Sigma 5(210)$ boundary.

It was initially intended to produce T-interfaces from the annealed tilt grain boundaries discussed in chapter 4, however when cutting a surface perpendicular to the grain boundary plane it was found that annealed structures had a tendency to produce different surfaces on each grain. As a result surfaces were cut into the tilt boundary systems at the pre-relaxation stage. For each of these T-interfaces two different systems possessing similar volumes and

were developed, consisting of either 2 and 4 grains. A schematic of a T-interface is displayed in figure 6.12 showing systems consisting of 4 grains.

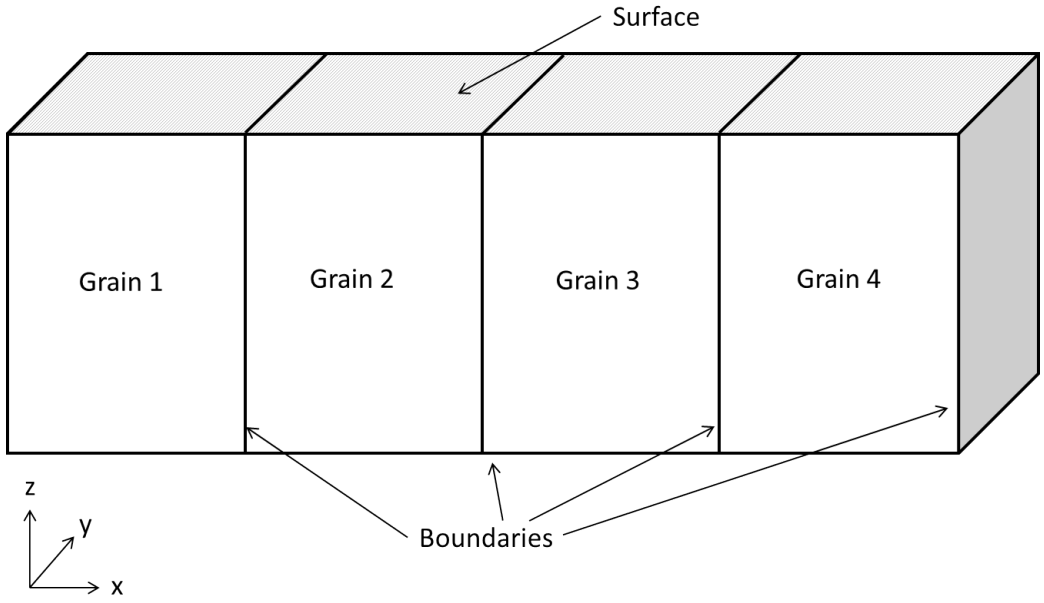

Figure 6.12: Schematic of T-interface containing four grain boundaries

Following the construction process the T-interfaces were then annealed using DL_POLY [173]. The NPT ensemble was used for this purpose and after initially heating the structures for 1 ns at 300 K the systems were annealed for 1ns at 2500 K and 2200 K for the $\Sigma3(111)$ and $\Sigma5(210)$ systems respectively. The resulting structures were run for a further 1 ns at 300 K to complete the annealing process. With this process complete each T-interface was heated again using NPT to the temperature that would be required for the final simulations. For the $\Sigma3(111)$ this was between 1400-2400 K and 1400-2200 K for the $\Sigma5(210)$ at intervals of 200 K. Before helium was added to the system each T-interface was run at each temperature for 1ns using the NVT ensemble. This ensured the systems were fully equilibrated reducing the need for a long equilibration time after helium was added so that better statistics could be obtained.

Helium was added only after the annealing and full equilibration of the systems at the final simulation temperatures in a 5 Å thick band in the centre of the slab running in the X direction parallel with the surfaces. The band in each cell consisted of 200 helium atoms which were inserted in random positions within the band area, but care was take to ensure that helium added to these systems was not positioned in any of the grain boundaries.

Simulations were then run for 5ns following a 10ps equilibration time using the NVT ensemble. For each T-interface the rate of release of helium atoms from the solid to the vacuum gap was calculated. To accomplish this the number of helium atoms residing in the vacuum gap was counted at 50ps intervals and the data displayed as a percentage over the length of the simulation. These data were then used to estimate the rate constants and activation energy for the evolution of helium from the solid to the vacuum gap using equations 6.1 and 6.2. $[He]_0$ refers to the maximum concentration of helium that can be released from the T-interface while $[He]_t$ denotes the fraction of helium released at time t.

$$\ln\left(\frac{[He]_0}{[He]_0 - [He]_t}\right) = kt \tag{6.1}$$

The plots gave straight lines in all cases, confirming the first order integrated rate equation is appropriate.

$$k = A\exp\left(\frac{-Ea}{RT}\right) \tag{6.2}$$

For each T-interface the diffusion path of the helium atoms is determined by looking at the positions of helium atoms during the simulation and displayed in relation to the position of the uranium atoms during the simulations. The isosurfaces were determined at the highest simulation temperature to ensure significant statistics could be obtained.

6.4.1 $\Sigma 3(111)$

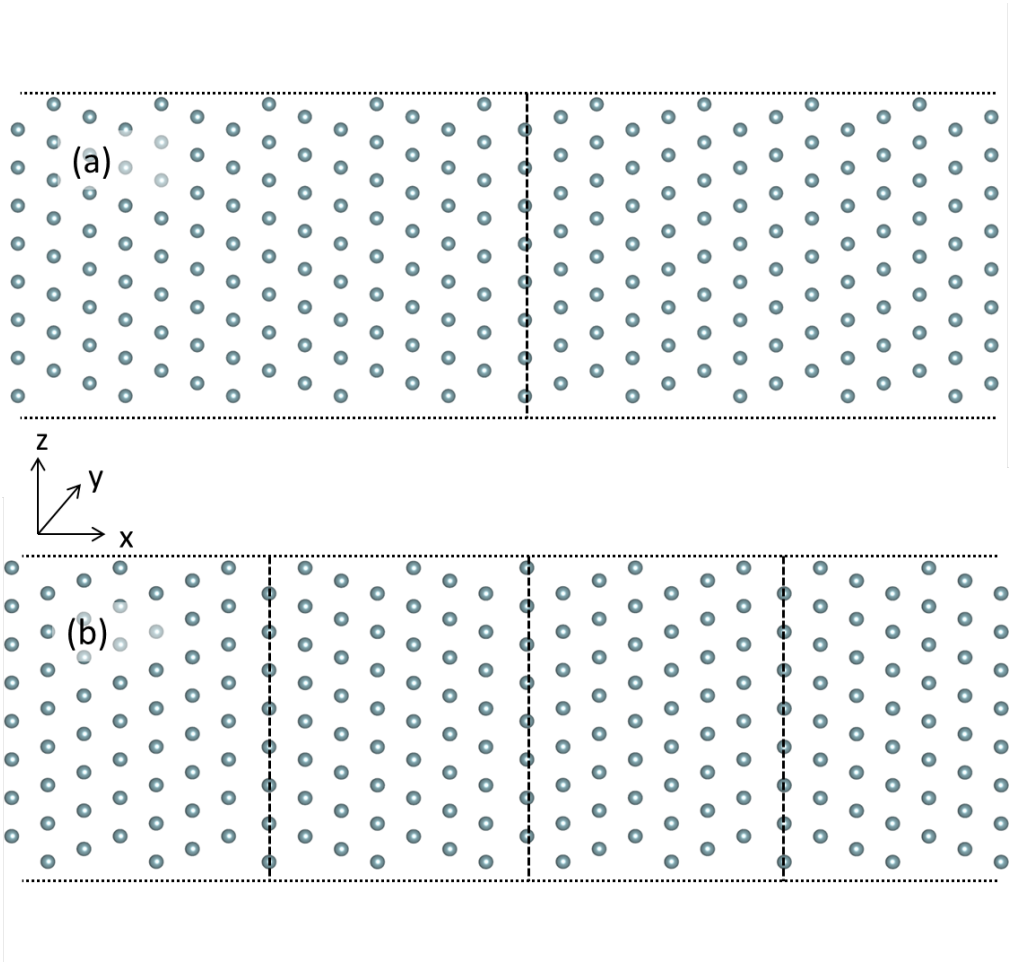

Figure 6.13: Side view of the initial structures of the (111) T-interfaces before annealing, the structure in (a) is made of two grains while structure (b) has 4 constituent grains, the presence of grain boundaries is indicated by dashed lines and surfaces by dotted lines. Only uranium atoms are shown.

The structure of the $\Sigma 3(111)$ T-interfaces before and after annealing are shown in figures 6.13 and 6.14 with oxygen atoms removed. The surface of this T-interface is (-211) and it appears that the process of annealing the T-interfaces has had very little effect on the surface as in both cases it is faceted and very similar in appearance. The only slight difference is observed where the boundary and surface meet where there appears to be some rearrangement of uranium positions. This T-interface was annealed at 2400 K as at higher temperatures the surfaces were unstable.

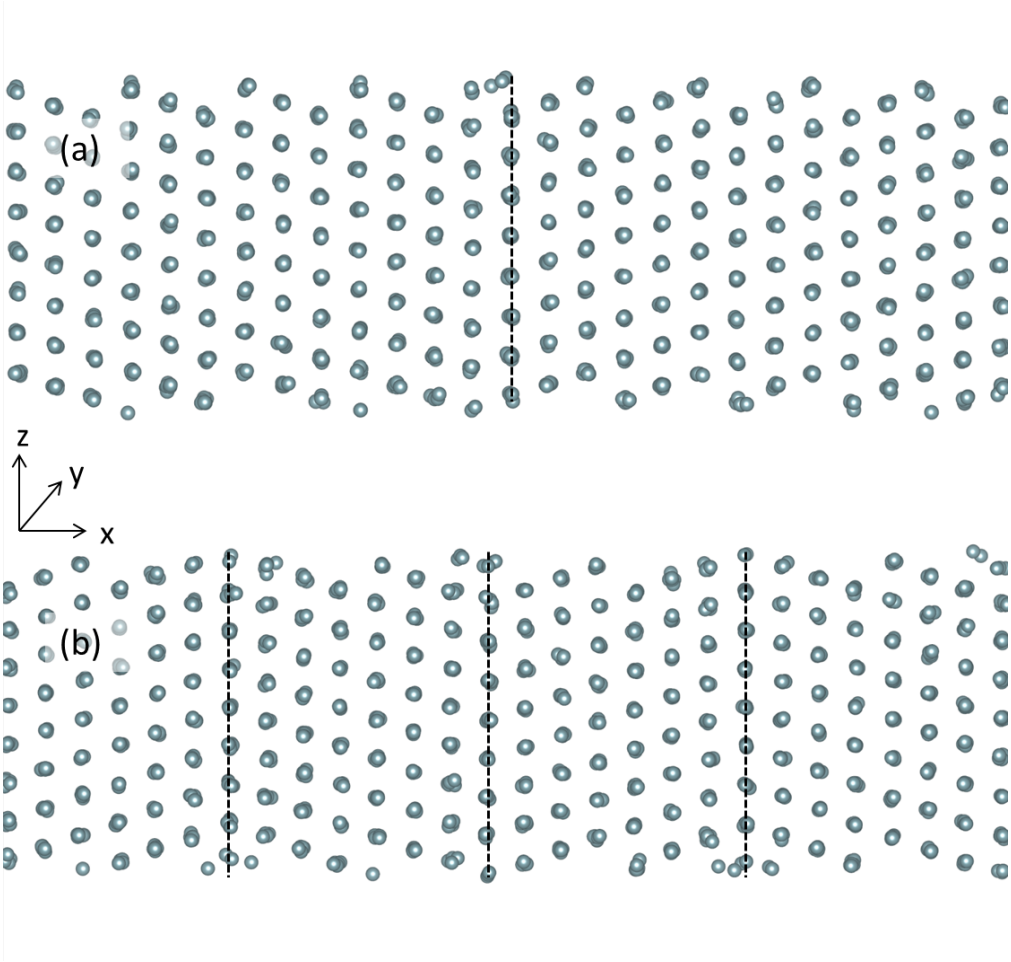

Figure 6.14: Side view of the annealed structures of the (111) T-interfaces, the structure in (a) is made of two grains while structure (b) has 4 constituent grains, the presence of grain boundaries is indicated by dotted lines. Only uranium atoms are shown.

Figure 6.15 shows the release of helium in the two grain system at temperatures between 1400 K and 2400 K. At the lowest temperature no helium is released from the system to the vacuum gap, while at 2400 K 100% of helium is released. At 1400 K there does not appear to be enough thermal energy for significant diffusion to take place and as a result no release of helium was seen. Between these two extremes we see an increase in the percentage released with increasing temperature. One of the most obvious features of this system is the initial release rate which appears to be significantly faster than the average rate of release over the entire simulation length.

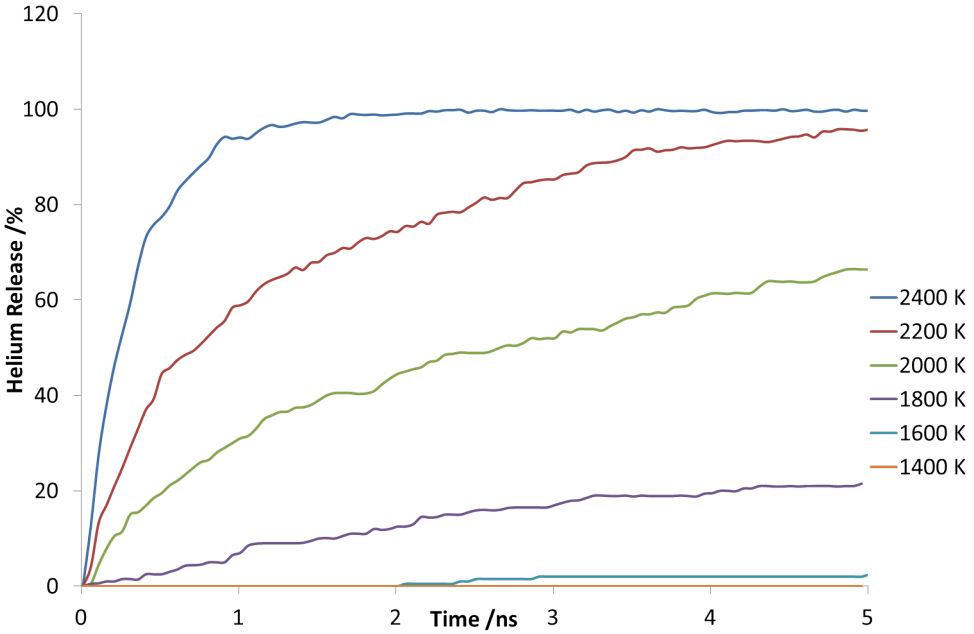

Figure 6.15: Percentage helium released in the $\Sigma 3(111)$ T-interface as a function of time for the model with 2 grains at temperatures between 1400 K and 2400 K

The system containing four boundaries shows a similar pattern, although with some differences. All temperatures showed an increase in the rate of helium release and where possible a corresponding increase in the overall fraction of helium evolution. Indeed some diffusion was seen at the lowest temperature system compared to no release in the system with only grains. Once again at high temperature 100% release of helium is seen and the same is observed for 2200 K.

As the only difference between the two systems is the number of grains present and as a result the number of boundaries this suggests that the increased number of grain boundaries and the inherent reduction in distance between them is dramatically increasing the rate of helium evolution. It is however interesting that in figures 6.15 and 6.16 the initial diffusion rate appears to be higher than the overall rate. One reason for this may be as a result of the tendency of grain boundaries to enhance the diffusion in the bulk region around the interface. In section 6.3 we see that helium diffusion in the $\Sigma 3(111)$ grain boundary is fastest at the boundary and decreases to bulk values at a distance of 8 Å. The simulation cell was designed so that no helium was added to the grain boundary interface, however some helium will still be located in the grain boundary width. Helium which is initially located closest to the interface diffuses faster and as a result the chances of helium atoms diffusing along the boundary to the surface are increased.

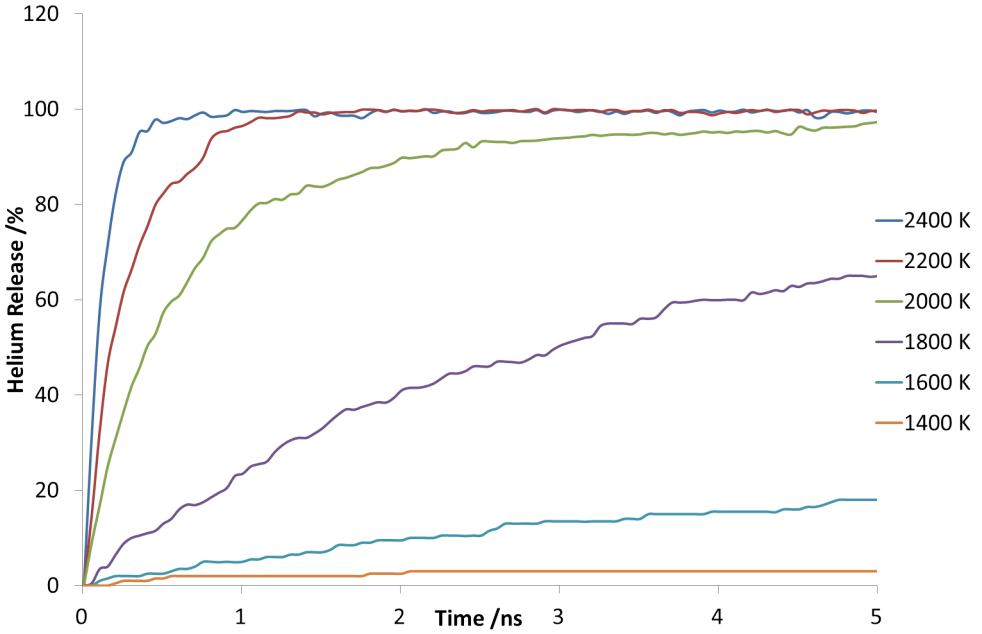

Figure 6.16: Percentage helium released in the $\Sigma 3(111)$ T-interface as a function of time for the model with 4 grains at temperatures between 1400 K and 2400 K

One way of trying to show the migration path of helium is to create an isosurface from the positions of the helium atoms during the simulation. The isosurfaces can be broken down to show a particular time-period or time-periods during the simulation and the resulting isosurfaces added to a diagram of the uranium positions. From the rate data the most helium diffusion was occurring in the initial stages of the simulation and by looking at an isosurface of the system at the highest temperature we should be able to determine the largest number of statistics in a short space of time. Therefore it was possible to show isosurfaces over 10 ps intervals in the initial 40 ps of the simulation with the results for both systems shown in figure 6.17.

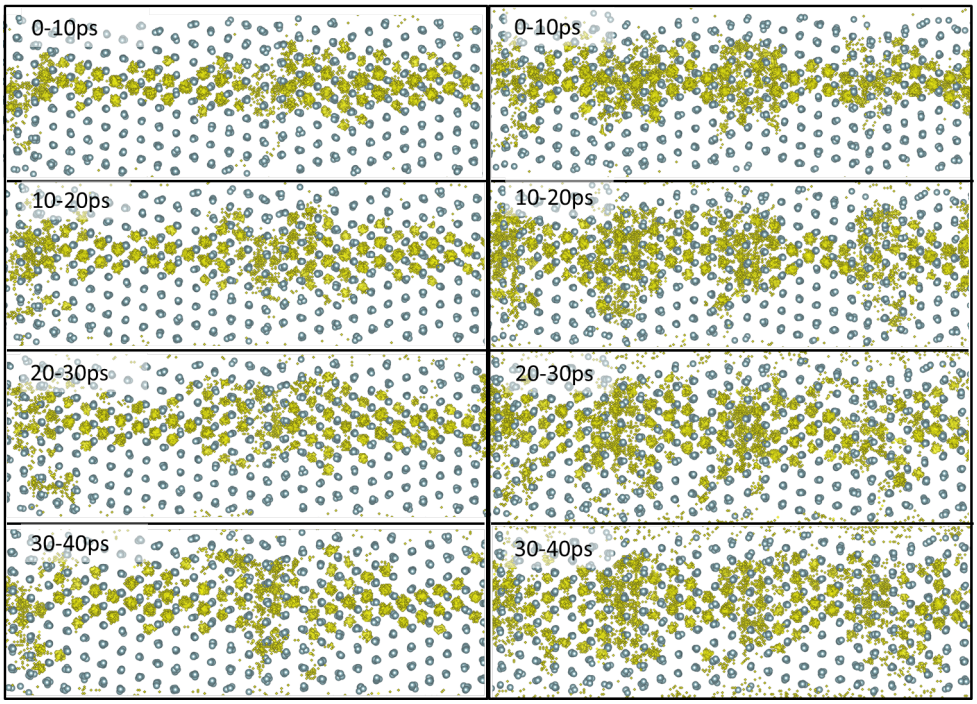

Figure 6.17: Isosurface showing the helium atom positions during the first 40ps of the simulation relative to the uranium ions at temperatures of 2400 K. The left column shows the system consisting of two grains and the right column the system consisting of four grains

From the isosurfaces of the two systems we see a significant difference in diffusion behaviour. The system containing 2 boundaries shows that large numbers of helium atoms stay in or close to their starting positions during the initial 10 ps of the simulation and with the original band still visible throughout. Only at the grain boundaries do we see significant diffusion. Between 30-40 ps it is possible to see helium occupying positions the length of the boundary where helium in the rest of the cell is far more localised. The four boundary system shows a far greater spread of helium positions over the same time-scale which further suggests that the presence of grain boundaries is enhancing diffusion of helium. Similarly to the two boundary system there also appears to be more diffusion at the grain boundary interfaces. Activation energies for these two T-interface systems are predicted to be very similar which suggests that helium diffusion mechanism to the vacuum gap is unaffected by the grain size but in both cases a large error value is attributed to each making it hard to be certain.

Table 6.4: Activation energies of helium release from the $\Sigma 3(111)$ T-interfaces

System	E_a/eV	Error 95% Confidence Level /eV
2 Grains	2.5	1.1
4 Grains	2.2	0.8

6.4.2 $\Sigma 5(210)$

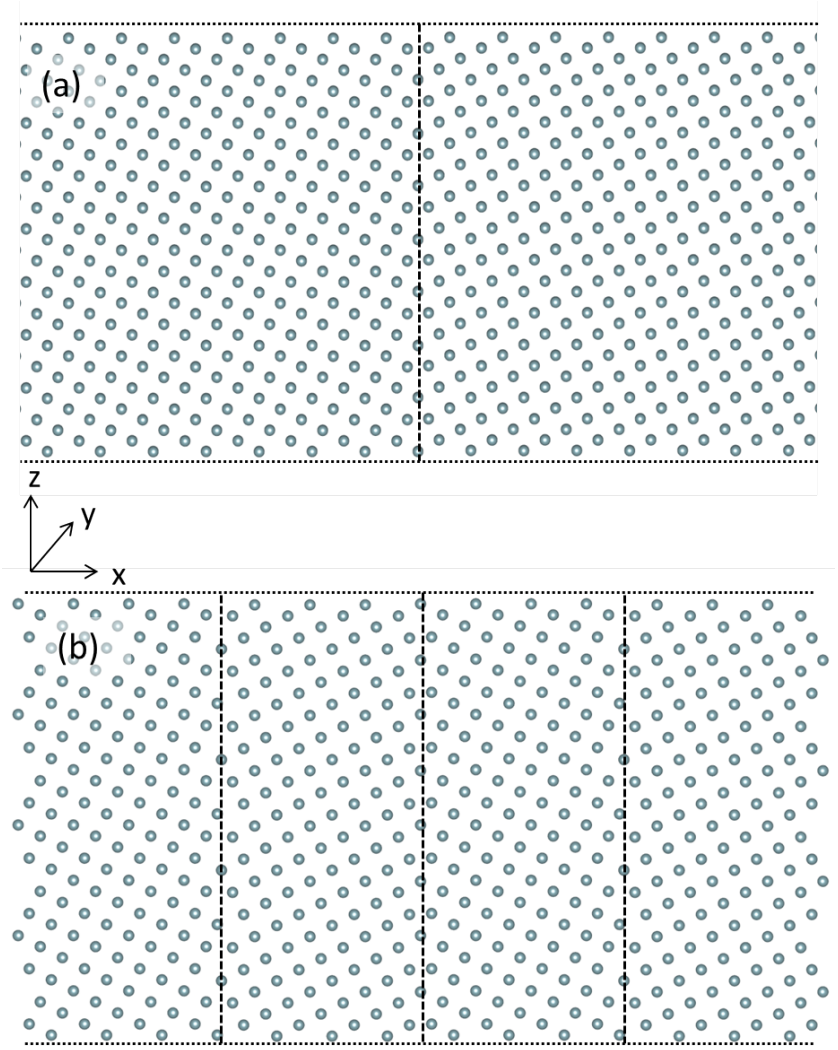

Figure 6.18: Side view of the annealed structures of the $\Sigma 5(210)$ T-interfaces, the structure in (a) is made of two grains while structure (b) has four constituent grains, the presence of grain boundaries is indicated by dashed lines and surfaces by dotted lines. Only uranium atoms are shown.

The structures of the two grain and four grain $\Sigma 5(210)$ T-interface are shown before and after the annealing process in figure 6.18 and 6.19. The surface present in this system is the (1-20). This is a type 3 surface and we can see from the structures that during the annealing process the surfaces have seen some rearrangement. This is likely due to the fact that type 3 surfaces are made up of charged planes meaning a dipole is present at the surface. No major faceting is seen at the surface apart from the point at which the boundary meets the surface. The 2 $\Sigma 5(210)$ structures are significantly thicker than the $\Sigma 3(111)$ tilt boundary as the extra

width was required to stabilise the systems. Even with the thicker cell this T-interface was only stable to temperatures of 2200 K and below.

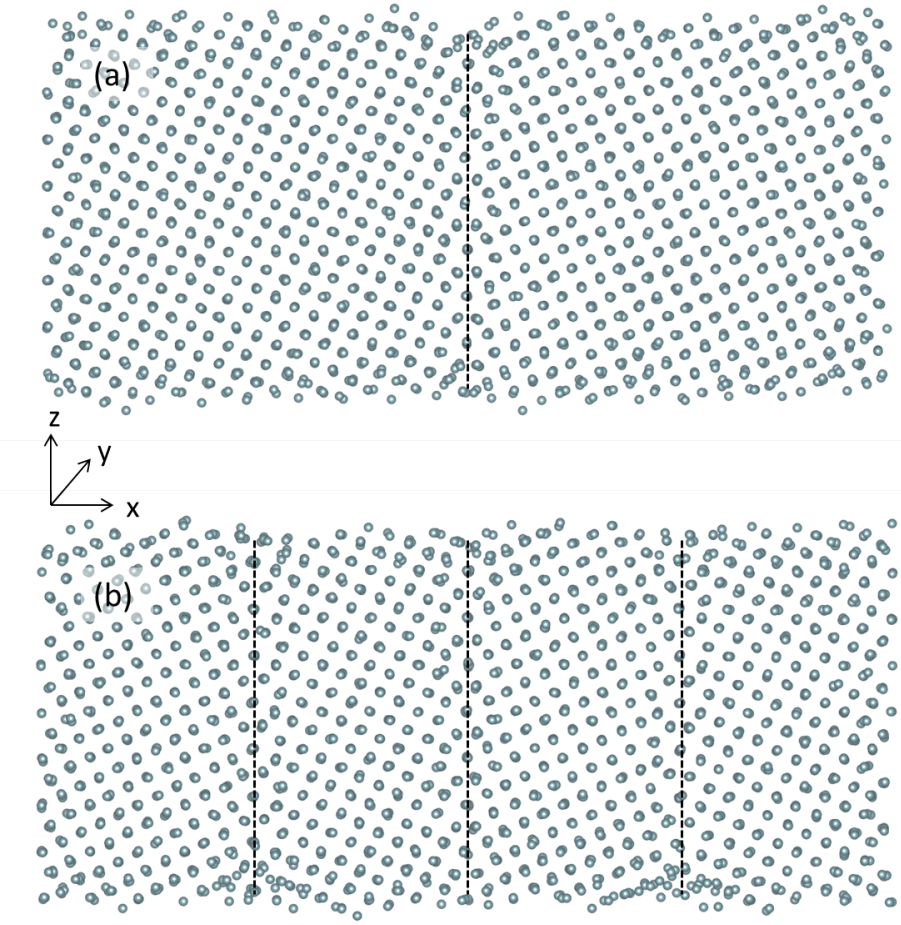

Figure 6.19: Side view of the annealed structures of the $\Sigma 5(210)$ T-interfaces, the structure in (a) is made of two grains while structure (b) has four constituent grains, the presence of grain boundaries is indicated by dotted lines. Only uranium atoms are shown.

Helium release in this T-interface was quite different to that seen in the $\Sigma 3(111)$ T-interface. The fraction of helium released at the end of the simulations for the $\Sigma 5(210)$ was far lower than either $\Sigma 3(111)$ T-interface after 5 ns. Alongside this the rate of release was broadly linear with the rate of evolution constant throughout the simulation. Over the 5 ns this was best illustrated by the system at 2200 K, however this may also be true for lower temperatures but longer time scales are required to fully determine if this is the case.

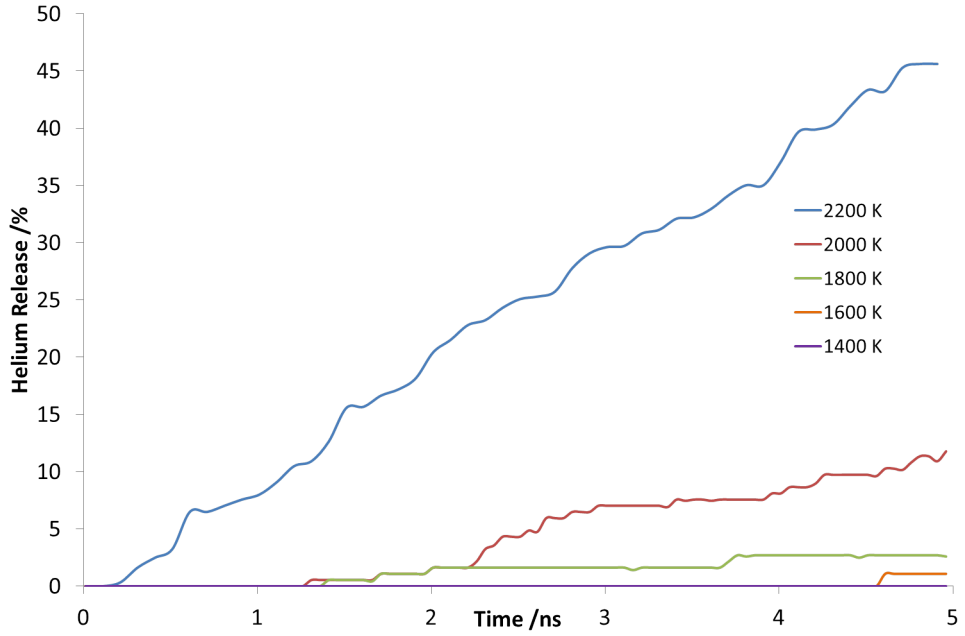

Figure 6.20: Percentage helium released in the $\Sigma5(210)$ T-interface as a function of time for the model with 2 grains at temperatures between 1400 K and 2200 K

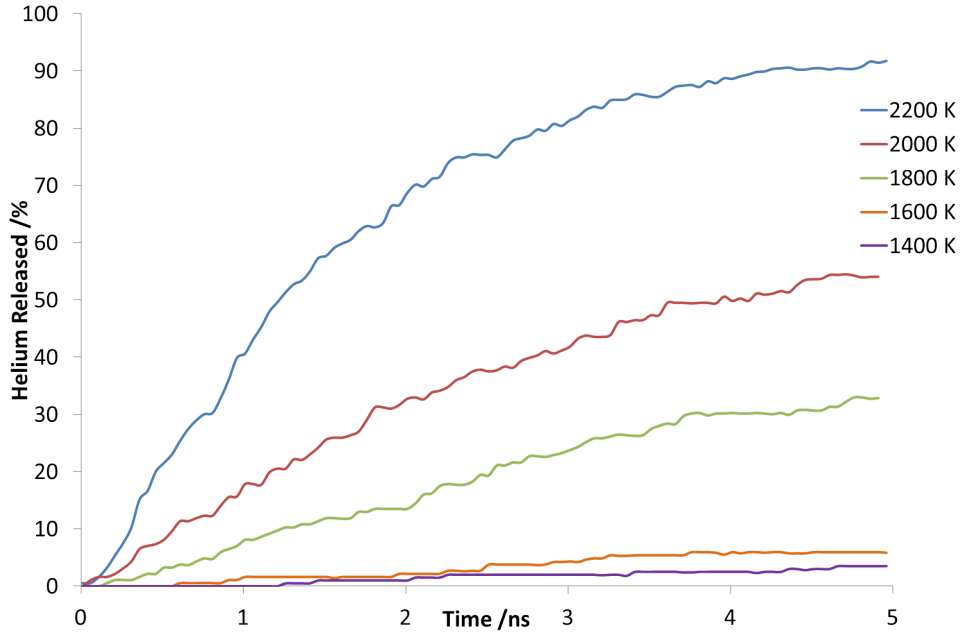

Figure 6.21: Percentage helium released in the $\Sigma5(210)$ T-interface as a function of time for the model with 4 grains at temperatures between 1400 K and 2200 K

It is no surprise that the rate of helium release is significantly slower for the $\Sigma5(210)$ T-interfaces compared to the $\Sigma3(111)$ due to the increased thickness of the slab meaning that helium needs to diffuse further in order to reach the vacuum gap. Additionally in both

the $\Sigma5(210)$ and $\Sigma3(111)$ T-interfaces the helium must diffuse in the Z direction in order to reach the surface and the vacuum gap. However a large discrepancy is seen between diffusion rates in this direction between the two boundary systems. The $\Sigma3(111)$ boundary experiences diffusion in this temperature region up to 25 times faster in the Z direction whereas the $\Sigma5(210)$ boundary only sees diffusion up to 13 times faster.

In the same manner as for the $\Sigma3(111)$ T-interface an isosurface detailing the positions at which helium atoms were recorded during the simulation can be created. As the rate of helium evolution was significantly slower for this system it was necessary to observe behaviour over a longer time-scale (0-300ps) to be able to determine information about diffusion pathways. Isosurfaces for the $\Sigma5(210)$ T-interfaces are shown in figure 6.22.

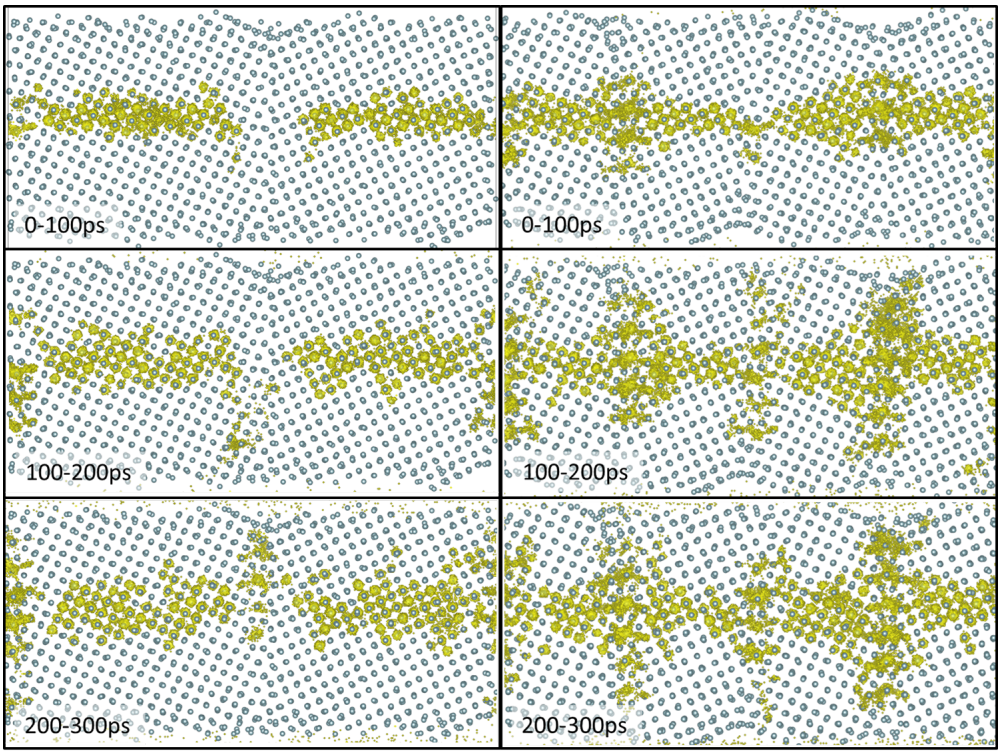

Figure 6.22: Isosurface showing the helium atom positions during the first 300 ps of the simulation relative to the uranium ions at temperatures of 2200 K The left column shows the system consisting of two grains and the right column the system consisting of four grains.

The isosurface for the system containing only two boundaries illustrates the diffusion path along the grain boundary quite effectively. For the first 100 ps little significant diffusion is seen and the helium remains located near to its starting positions with little if any diffusion to the grain boundary interface. As the simulation time progresses the band of helium

gradually widens and helium starts to diffuse along the grain boundary interface. Between 200-300 ps clear diffusion paths for helium can be seen form the central band along the interface to the surface and vacuum gap. A similar pattern is seen over this time-scale for the four grain boundary system however the presence of two extra boundaries leads to a wider distribution of helium and significant diffusion along the grain boundaries is evident earlier than in the 2 grain system.

Table 6.5: Activation energies of helium release from $\Sigma5(210)$ T-interfaces

System	E_a/eV	+/- /eV
2 Grains	2.6	0.3
4 Grains	1.8	0.7

The calculated activation energies support the idea that helium release is being significantly enhanced by the presence of more grain boundaries. The four grain system is more defective and hence may be expected to behave like a system with more oxygen vacancies, i.e. low activation energy pathways. However even though the four grain system has a lower activation energy its error of 0.7 eV gives quite a large range which will overlap that of the two boundary system. It is worth noting that the value of 2.6 eV recorded for the 2 boundary system is very similar to the activation energy of bulk helium diffusion and the $\Sigma3(111)$ T-interfaces.

6.5 Summary

In this chapter we presented a new potential model for helium by modifying the potential model derived by Yakub [109]. This model in conjunction with our UO_2 potential reproduces defect and migration energies of helium in UO_2. Helium conductivity in the bulk is faster than oxygen at the similar temperatures. It has been well documented in literature that the presence of oxygen vacancies will significantly reduce the activation energy of helium diffusion. When studying bulk diffusion we see that the onset of fast ionic behaviour in oxygen causes a similar increase in diffusion of helium.

The segregation and diffusion of helium was studied for six tilt grain boundaries. Energy minimisation calculations suggest helium will segregate to the $\Sigma3(221)$, $\Sigma5(210)$, $\Sigma19(331)$, $\Sigma5(310)$ and $\Sigma11(311)$ grain boundaries. While density profiles from molecular dynamics simulations show that at high temperatures all systems will have helium residing at the grain boundary. The only system that didn't show any stabilisation of helium interstitial atoms during static simulations was observed to have a lower concentration of helium at the boundary compared to the bulk. Bubbles of helium formed in the three systems $\Sigma5(210)$, $\Sigma19(331)$, $\Sigma5(310)$ but only at higher temperatures. However it is possible that given enough time bubbles would form in these systems at lower temperatures as well. What is not clear is whether the other boundaries would form bubbles if simulations were run for a longer time period. The segregation of helium to the boundaries does not have an effect on the boundary structure however, bubble formation in some systems caused the breakdown of the boundary structure. This was particularly true of larger bubbles. In the case of the $\Sigma3(221)$ boundary the segregation of helium caused the boundary to diffuse while the same system without helium did not. Diffusion of helium in boundaries was studied over the same range of temperatures as for oxygen diffusion. While some similarities were seen in the shapes of the diffusion profiles and width of diffusion, normalised diffusion rates of helium were generally higher than those seen for oxygen. However it is possible in some instances that diffusion statistics were altered by the presence of bubbles.

The final part of this chapter was dedicated to a preliminary investigation into how to generate T-interfaces. These are a development of tilt grain boundaries enabling us to investigate the properties of the interface where surfaces and grain boundaries meet. The two T-interfaces generated were chosen for the fact that one had been shown to segregate he-

lium that diffused to the grain boundary $\Sigma5(210)$ while the other did not $\Sigma3(111)$. Although in both cases no bubbles were formed and helium diffused directly to the vacuum gap. By producing isosurfaces illustrating the helium positions at different times during the simulation we showed that the boundaries were the major diffusion pathway to the vacuum. However we cannot say for sure that no helium release to the vacuum gap took place via the surfaces. In order to generate the $\Sigma5(210)$ T-interface a thicker slab was required than the $\Sigma3(111)$ as a result comparing the rate of helium loss between the two is problematic. However by calculating the activation energy of the release of helium the T-interfaces it appeared that the activation energy of release was similar in both systems and also resembled the bulk value. The large error in the slopes used to determine these values make it difficult to draw strong conclusions and any future work on these systems would do well to investigate T-interfaces at smaller temperature intervals to increase the resolution of these values. T-interfaces with a greater number of grains displayed lower activation energies for the release of helium and as a result we can predict that grain size will have a strong bearing on the diffusion of helium from the solid phase to the vacuum gap.

Chapter 7

Conclusions and Future Work

The aim of this investigation is to improve understanding of the role of grain boundaries on oxygen transport in polycrystalline UO_2 through the detailed study of grain boundary interfaces. The work is divided into a number of sections. Chapter 3 focuses on the development of a new potential model intended for use in the simulation of of grain boundary interfaces in UO_2. Bulk properties predicted by this new potential are compared with experimental values and values predicted using literature potentials. In chapter 4 the focus shifts to investigating structure, stability and oxygen transport properties of tilt grain boundaries in UO_2 using the newly derived potential. Chapter 5 centres on the approaches for generating twist grain boundaries and the influence of these interfaces on diffusion pathways for oxygen migration. Chapter 6 initially considers the development of a robust potential model for helium, which was then employed to investigate the segregation and transport of helium in grain boundaries. The final part of this chapter reports simulations on helium diffusion at the interface where a grain boundary meets the external grain surface, known as a T-interface.

7.1 Potential Model

During this investigation we have successfully developed a new potential model specifically for use in modelling grain boundary interfaces in UO_2 using both energy minimisation and molecular dynamics. Further potentials were also developed for ThO_2 and U_3O_8 utilising

the same anion-anion potential to enable interoperability. Although many potentials are available for UO_2, we required a model that was fast to compute but with the necessary accuracy for structure, elasticity and defect properties. Potentials were fitted to experimental structure and elastic properties to accurately reproduce the stress response of the crystal and enable us to model UO_2 structures at high pressures and temperatures and indeed at grain boundary structures where there may be local stresses and strains. The model was validated through the comparison of calculated and experimental values of bulk and defect and surface energies. Calculated defect energies overall were higher than experiment although the anion Frenkel energy was similar and correctly predicted to be the most favourable defect. The uranium Frenkel defect energy in particular is significantly higher than experimental values and as a result it is likely that this model is unsuitable for the investigation of uranium transport. A particular advantage of this model is its very accurate reproduction of the activation energy of oxygen vacancy migration where it was more accurate than any other potential model reported.

Studies of bulk oxygen diffusion highlighted the existence of three different temperature regions each characterised by a distinct diffusion mechanism. The three regions are the vacancy region, lattice diffusion region and superionic region. The activation energy for lattice diffusion calculated from oxygen diffusion simulations is in a similar range to that seen experimentally indicating that this new potential model is suitable for modelling UO_2 transport properties in grain boundaries.

7.2 Tilt Grain Boundaries

The structure, stability and oxygen transport properties of six different tilt grain boundaries were investigated in chapter 4 using the newly derived UO_2 potential. We wanted to extend the range of boundaries considered for UO_2 to begin to investigate trends in oxygen diffusion. But we limited it to boundaries experimentally characterised in fluorite materials. Our approach for generating these boundaries involved first putting two surfaces together, scanning one surface over the other and then annealing at a range of temperatures. We also used thick bulk regions to ensure that each boundary was isolated. All grain boundaries proved to be stable at the temperatures studied with no cleavage or reforming of bulk observed. Boundary instability was observed in some cases in the form of boundary diffusion but

was only detected at higher temperatures for certain boundaries. The mechanism of grain boundary mobility might be an interesting subject for future investigation. The annealing process resulted in structural changes in two of the six grain boundaries and indicates that when investigating these systems the structures predicted by energy minimisation cannot be entirely relied upon as the lowest energy grain boundary structure.

At the temperatures studied all tilt grain boundaries significantly enhance the diffusion of oxygen in UO_2. This enhancement was not limited to the boundary interface as increased diffusion rates are observed in the bulk region surrounding the interface. However the effect of each different tilt boundary on oxygen diffusion varies substantially depending on the structure of the system being studied. Variations in diffusion behaviour manifest as variations in diffusion width, relative intensity and the shape of diffusion profiles. Temperature also has a significant effect on diffusion behaviour. The general trend for all boundaries was for the average normalised diffusion to increase until temperatures around 2600 K where the relative enhancement of diffusion in the grain boundaries gradually decreases. This decrease is as a result of increased diffusion in the bulk reducing the normalised diffusion rates so at high temperatures the contribution of grain boundaries to diffusion in polycrystalline systems is less significant. Structural and temperature dependence also results in variable diffusion behaviour as a result of phase changes. The directional dependence of oxygen diffusion also varied greatly with grain boundary structure and temperature. Some systems displayed mainly isotropic behaviour while others were clearly anisotropic. This varying degree of directional dependence was also temperature dependent with the only constant being at the highest temperatures when the system is nearing fast ion diffusion and the boundary enhancement is significantly reduced. The influence of structure means that in a polycrystalline system not only will the oxidation of the fuel be dependent on grain size but also on grain type.

Through the course of this investigation we have shed new light on the diffusion behaviour of oxygen in grain boundaries and a simple extension would be to investigate a greater number of tilt boundaries. However, we have already studied 6 and while we have identified how the grain boundaries behave we have still to evaluate the mechanism of diffusion in each boundary. In chapter 3 we saw that different diffusion behaviour was observed in the bulk depending on whether vacancies were present in the system. An interesting extension of the current work would be to change the composition, for example, to see what effect if

any the presence of vacancies would have on the diffusion of oxygen in the grain boundaries and whether any segregation occurs from the bulk and if so if any structural alterations are seen as a result.

7.3 Twist Grain Boundaries

In Chapter 5 we describe work on developing new reliable approaches for generating twist grain boundaries and report the impact three of these interfaces have on oxygen diffusion in comparison to tilt boundaries. The challenge in generating these interfaces is to reduce any like-ion interactions at the interface. We describe two different methods that were implemented. The first involved scanning the rotated surfaces relative to one another in order to find the lowest energy configuration. The second method used a combination of oxygen and uranium terminated surface to reduce the like ion density at the interface.

All twist grain boundaries survived energy minimisation and in most cases the different rotations of the same structures behaved similarly. Both methods of construction appear to have removed any significant close range like-ion interactions however, when the thermal stability was probed using molecular dynamics only three grain boundaries survived temperatures exceeding 2000 K. All three were full density systems and as a result we can conclude that the process of scanning twist boundaries is a better method of producing stable interfaces than creating reduced density boundaries using differently terminated surfaces. From annealing experiments we can also conclude that the calculation of static grain boundary energies does not allow us to accurately predict thermal stability as there are many ways a system can be unstable without cleavage of the grain boundaries. Twist boundaries will have different structures to the corresponding tilt boundaries and in some instances display markedly different thermal stability.

Diffusion results for the stable twist boundaries show that they are also fast diffusion pathways for oxygen. In each case normalised diffusion rates increased with temperature and then after reaching a maximum at about 2600 K a sharp decrease was seen as diffusion rates in the bulk increased. This decrease was observed all the way to 3000 K. This behaviour is in line with similar observations for tilt grain boundaries and in fact when compared very little difference was observed between tilt and twist boundaries. Tilt and twist boundaries

showed little variation in terms of their relative effect on diffusion rates or on the directional dependence of diffusion. This leads us to conclude than in terms of investigating the effects of grain boundaries on oxygen diffusion in polycrystalline systems that have been annealed it is sufficient to investigate tilt grain boundaries. These are easier to generate, have a similar range of stability and show very little difference in terms of their effect on oxygen diffusion.

Now that we have identified a preferential method of building stable twist grain boundaries in UO_2 an obvious extension would be to consider a greater range of boundaries. The two chosen for study in this thesis were selected due to the fact that they produce reasonably flat surfaces making the construction process simpler however, these two boundaries showed the least complexity in terms of diffusion behaviour. It may be the case that other twist grain boundaries do not behave in a similar manner to the corresponding tilt boundary. As there is always the possibility that the grains in a polycrystalline system will not all be terminated with the same surfaces another way of further extending this study would be to consider twist boundaries generated from two different miller index surfaces.

Even though reduced density twist boundaries in this case proved to be less stable than the full density systems, we cannot say that this is always the case. The reduced density systems we studied were an extreme case with significantly reduced density and it may be the case that a smaller reduction in density using a more systematic method of removing conflicting atoms would also produce stable twist boundaries. Another way of expanding this study would be to look at the segregation of oxygen vacancies in twist boundaries in a similar manner to the helium segregation study conducted in chapter 6. Performing this sort of calculation on full density twist boundaries may provide a simple test as to whether twist boundaries in UO_2 are more stable with full or reduced density.

7.4 Helium Segregation and Transport at Interfaces

In the final results chapter we presented a modified potential model for helium which was used in conjunction with the Morl potential accurately reproduces defect and migration energies of helium in UO_2. The bulk diffusion properties were determined and then segregation and diffusion of helium was studied for six tilt grain boundaries. Finally the scope of the investigation was then expanded to include a preliminary study of a new type of interface known as a T-interface.

Helium diffusivity in the bulk is faster than oxygen at the similar temperatures. When studying bulk diffusion we see that the onset of fast ionic behaviour in oxygen causes a similar increase in diffusion of helium. Energy minimisation calculations suggest helium will segregate to all but one of the tilt boundaries, the $\Sigma3(111)$, while density profiles from molecular dynamics simulations show that at high temperatures all systems will have some degree of helium residing at the grain boundary. However, only half of the boundaries considered ($\Sigma5(210)$, $\Sigma19(331)$, $\Sigma5(310)$) show any significant segregation above the bulk concentration of helium and in each of these cases helium bubbles of varying size form at the interface. Diffusion of helium in boundaries was studied over the same range of temperatures as for oxygen diffusion. In a similar manner to oxygen diffusion the transport of helium was enhanced in the grain boundary and the surrounding bulk region. While some similarities were seen in the shapes of the diffusion profiles and width of diffusion, normalised diffusion rates of helium were generally higher than those seen for oxygen.

To understand further the segregation and diffusion of helium in tilt grain boundaries a systematic examination of the energies of oxygen vacancies occupied by helium atoms would be worthwhile in a similar way to the investigation of helium interstitial energies. It is generally accepted that a lower energy barrier is present for helium when diffusing via an oxygen vacancy. The enhanced diffusion of oxygen at the boundaries increases the chance of oxygen vacancy defect sites forming at the boundary that may play a role in segregation and bubble formation. From this we may be able to determine information on the mechanism of helium diffusion at the interface.

Whilst we have observed the formation of bubbles at particular grain boundaries we cannot rule out that helium bubbles will only form at some boundaries and at particular temperatures. An obvious extension of this work would be to look at some of these systems over a much longer time frame to see if bubble formation is seen in other systems. Additionally we haven't explored what effect variables such concentration have on helium bubble formation and what the implications are for grain boundary diffusion as a result of bubbles being present.

T-interfaces are a development of tilt grain boundaries enabling us to investigate the properties of the interface where surfaces and grain boundaries meet. Two T-interfaces were generated by cutting surfaces perpendicular to the $\Sigma5(210)$ and $\Sigma3(111)$ grain boundaries to generate slabs. The stability of these systems was then studied using molecular dynam-

ics. With both systems stable at high enough temperatures with respect to grain boundary diffusion no bubbles were formed enabling the investigation of helium transport from the bulk to the vacuum gap. During the simulations helium was released from the T-interface system to the vacuum gap and grain boundaries were shown to be the the major diffusion pathway. However it is difficult to definitively say that all helium diffused to the vacuum gap via the boundaries and no contribution was made by the surface. By calculating the activation energy of the release of helium at the T-interfaces, it appeared that the activation energy of release was similar in both systems and also resembled the bulk value. The large error in the slopes used to determine these values make it difficult to draw definitive conclusions, nevertheless T-interfaces with a greater number of grains displayed lower activation energies for the release of helium and as a result we can predict that grain size will have a strong influence on the diffusion of helium from the solid phase to the vacuum gap.

As this was a preliminary investigation into T-interfaces, there are a great many ways in which the work could be improved and expanded. An obvious extension would be to the investigate different T-interfaces to see how different boundaries and surfaces affect the release of helium. We demonstrated here that creating these interfaces from grain boundaries is viable and produces stable systems. However comparison of the two systems was difficult due to the varying widths. Wider T-interfaces are more computationally expensive due to the increased number of atoms present but will enable us to better study the release of helium via grain boundaries. Similarly by making T-interfaces with similar distances of a similar thickness comparison between different systems would be significantly easier. To obtain better results for the activation energy of helium release it would be necessary to investigate T-interfaces over a greater number of temperature intervals hopefully reducing error values in the activation energy of helium release. Thicker slabs may also increase the stability of the T-interfaces allowing us to study these systems at higher temperatures giving greater opportunity to see if any bubble formation will occur.

7.5 Overall Conclusions

Although we have studied a broad range of interfaces in UO_2 it is possible to draw some overall conclusions. We have successfully demonstrated methodologies to model a range of complex interfaces incorporating both grain boundaries and surfaces. The presence of

grain boundaries both tilt/twist enhance oxygen diffusion in the boundary and the surrounding region although the exact behaviour exhibited by each system varies according to the boundary being studied as well as structure and temperature. Similar behaviour is also true for the diffusion of helium in the same systems. We suggest that the diffusion properties of polycrystalline UO_2 will be dependent on the constituent grains and hence the type of interfaces present. We have shown that potential based methods can no be readily applied to a range of different interfaces, with time, as computer power increases it will become more and more feasible to perform a full statistical sweep of all feasible boundaries and thereby predict the behaviour of the general boundary structure.

Bibliography

[1] Read, M. S. D.; Jackson, R. A., Derivation of enhanced potentials for uranium dioxide and the calculation of lattice and intrinsic defect properties, *Journal of Nuclear Materials* **2010**, *406*, 293.

[2] Guerin, Y.; Was, G. S.; Zinkle, S. J., Materials Challenges for Advanced Nuclear Energy Systems, *Mrs Bulletin* **2009**, *34*, 10.

[3] Zinkle, S. J.; Was, G. S., Materials challenges in nuclear energy, *Acta Materialia* **2013**, *61*, 735.

[4] Chu, S.; Majumdar, A., Opportunities and challenges for a sustainable energy future., *Nature* **2012**, *488*, 294.

[5] Matthews, J. R., Technological Problems and the Future of Research on the Basic Properties of Actinide Oxides, *Journal of the Chemical Society-Faraday Transactions Ii* **1987**, *83*, 1273.

[6] Sari, C.; Benedict, U.; Blank, H., A Study of Ternary System UO_2-PUO_2-PU_2O_3, *Journal of Nuclear Materials* **1970**, *35*, 267.

[7] Nerikar, P.; Watanabe, T.; Tulenko, J. S.; Phillpot, S. R.; Sinnott, S. B., Energetics of Intrinsic Point Pefects in Uranium Dioxide from Electronic-Structure Calculations, *Journal of Nuclear Materials* **2009**, *384*, 61.

[8] Idriss, H., Surface reactions of uranium oxide powder, thin films and single crystals, *Surface Science Reports* **2010**, *65*, 67.

[9] Hoekstra, H. R.; Siegel, S.; Gallagher, F. X., The uranium-oxygen system at high pressure, *Journal of Inorganic and Nuclear Chemistry* **1970**, *32*, 3237.

[10] Katz, J. J.; Seaborg, G. T.; Morss, L. R., *The Chemistry of the actinide elements, Volume 1*, Chapman and Hall **1986**.

[11] Rabinowitch, E.; Katz, J. J., The Chemistry of Uranium **1951**.

[12] Allen, G. C.; Tucker, P. M., Surface oxidation of uranium metal as studied by X-ray photoelectron spectroscopy, *Journal of the Chemical Society, Dalton Transactions* **1973**, 470.

[13] Ellis, W. P., Auger/loss studies of uranium, uranium oxidation, UO_2, U_3O_8, and UF_4, *Surface Science* **1976**, *61*, 37.

[14] Petit, L.; Svane, A.; Szotek, Z.; Temmerman, W. M.; Stocks, G. M., Electronic structure and ionicity of actinide oxides from first principles, *Physical Review B* **2010**, *81*, 045108.

[15] Kim, K. C.; Olander, D. R., Oxygen Diffusion in $UO_2 - x$, *Journal of Nuclear Materials* **1981**, *102*, 192.

[16] Matzke, H., Atomic Transport Properties in UO_2 and Mixed Oxides (U, PU)O_2, *Journal of the Chemical Society-Faraday Transactions Ii* **1987**, *83*, 1121.

[17] Willis, B. T. M., Defect Structure of Hyper Stoichiometric Uranium-Dioxide, *Acta Crystallographica Section A* **1978**, *34*, 88.

[18] Yakub, E.; Ronchi, C.; Staicu, D., Computer simulation of defects formation and equilibrium in non-stoichiometric uranium dioxide, *Journal of Nuclear Materials* **2009**, *389*, 119.

[19] Willis, B. T. M., Crystallographic Studies of Anion Excess in Uranium-Dioxide, *Journal of the Chemical Society-Faraday Transactions Ii* **1987**, *83*, 1073.

[20] Allen, G. C.; Tempest, P. A., Linear ordering of oxygen clusters in hyperstoicheiometric uranium dioxide, *Journal of the Chemical Society, Dalton Transactions* **1982**, 2169.

[21] McEachern, R.; Taylor, P., A review of the oxidation of uranium dioxide at temperatures below 400Â°C, *Journal of Nuclear Materials* **1998**, *254*, 87.

[22] Desgranges, L.; Badinozzi, G.; Simeone, D.; Fischer, H. E., Refinement of the alpha-U_4O_9 Crystalline Structure: New Insight into the U_4O_9 -> U_3O_8 Transformation, *Inorganic Chemistry* **2011**, *50*, 6146.

[23] Belbeoch; B; Boivinea.JC, Structural Changes U_4O_9 **1967**, *90*.

[24] Garrido, F.; Ibberson, R.; Nowicki, L.; Willis, B., Cuboctahedral oxygen clusters in U_3O_7, *Journal of Nuclear Materials* **2003**, *322*, 87.

[25] Tempest, P. A.; Tucker, P. M.; Tyler, J. W., Oxidation of UO_2 Fuel Pellets in Air at 503K and 543K Studied Using X-ray Photoelectron-Spectroscopy and X-ray Diffraction, *Journal of Nuclear Materials* **1988**, *151*, 251.

[26] Desgranges, L.; Baldinozzi, G.; Simon, P.; Guimbretière, G.; Canizares, A., Raman spectrum of U_4O_9: a new interpretation of damage lines in UO_2, *Journal of Raman Spectroscopy* **2012**, *43*, 455.

[27] Yun, Y.; Rusz, J.; Suzuki, M. T.; Oppeneer, P. M., First-principles investigation of higher oxides of uranium and neptunium: U_3O_8 and Np_2O_5, *Physical Review B* **2011**, *83*.

[28] Allen, G.; Tucker, P.; Tyler, J., The behaviour of uranium oxides in low partial pressures of O_2 studied using X-ray photoelectron spectroscopy, *Vacuum* **1982**, *32*, 481.

[29] Pireaux, J.; Riga, J.; Thibaut, E.; Tenret-Noël, C.; Caudano, R.; Verbist, J., Shake-up satellites in the x-ray photoelectron spectra of uranium oxides and fluorides. A band structure scheme for uranium dioxide, UO_2, *Chemical Physics* **1977**, *22*, 113.

[30] Taylor, P.; Wood, D. D.; Duclos, A.; Owen, D. G., Formation of uranium trioxide hydrates on UO_2 fuel in air-steam mixtures near 200Â°C, *Journal of Nuclear Materials* **1989**, *168*, 70.

[31] Loopstra, B. O., Neutron Diffraction Investigation of U_3O_8, *Acta Crystallographica* **1964**, *17*, 651.

[32] Hoekstra; HR; Siegel; S; Fuchs; LH, The Uranium Oxygen System - UO_2.5 TO U_3O_8 **1955**, *59*, 136.

[33] Ball, R. G. J.; Dickens, P. G., Calculation of Structural and Defect Properties of Alpha-U3O8, *Journal of Materials Chemistry* **1991**, *1*, 105.

[34] Fujino, T.; Tagawa, H.; Adachi, T., On some Factors Affecting the Non-Stoichiometry in U_3O_8, *Journal of Nuclear Materials* **1981**, *97*, 93.

[35] Khilla; MA; ElfekeyY; SA; Rofail; NH, Infrared-Absorption Study of Uranium Trioxide Phases **1986**, *40*, 185.

[36] Greaves, C.; Fender, B. E. F., Structure of Alpha-UO_3 by Neutron and Electron-Diffraction, *Acta Crystallographica Section B-Structural Science* **1972**, *28*, 3609.

[37] Lidiard, A., Self-diffusion of uranium in UO_2, *Journal of Nuclear Materials* **1966**, *19*, 106.

[38] Catlow, C. R. A., Point Defect and Electronic Properties of Uranium Dioxide, *Proceedings of the Royal Society of London Series a-Mathematical Physical and Engineering Sciences* **1977**, *353*, 533–561.

[39] Jackson, R. A.; Murray, A. D.; Harding, J. H.; Catlow, C. R. A., The Calculation of Defect Parameters in UO_2, *Philosophical Magazine a-Physics of Condensed Matter Structure Defects and Mechanical Properties* **1986**, *53*, 27.

[40] Morelon, N. D.; Ghaleb, D.; Delaye, J. M.; Van Brutzel, L., A new empirical potential for simulating the formation of defects and their mobility in uranium dioxide, *Philosophical Magazine* **2003**, *83*, 1533.

[41] Govers, K.; Lemehov, S.; Hou, M.; Verwerft, M., Comparison of interatomic potentials for UO_2. Part I: Static calculations, *Journal of Nuclear Materials* **2007**, *366*, 161.

[42] Sorensen, O. T., *Nonstoichiometric Oxides*, Elsevier **1981**.

[43] Willis, B. T. M., Positions of the Oxygen Atoms in UO_2.13, *Nature* **1963**, *197*, 755.

[44] Catlow, C. R. A., Point Defect and Electronic Properties of Uranium Dioxide, *Proceedings of the Royal Society A: Mathematical, Physical and Engineering Sciences* **1977**, *353*, 533.

[45] Geng, H. Y.; Chen, Y.; Kaneta, Y.; Iwasawa, M.; Ohnuma, T.; Kinoshita, M., Point defects and clustering in uranium dioxide by LSDA+U calculations, *Physical Review B* **2008**, *77*.

[46] Grimes, R. W.; Catlow, C. R. A.; Stoneham, A. M., Calculations of Solution Energies of Fission Products in Uranium-Dioxide, *Journal of the American Ceramic Society* **1989**, *72*, 1856.

[47] Middleburgh, S. C.; Grimes, R. W.; Desai, K. H.; Blair, P. R.; Hallstadius, L.; Backman, K.; Van Uffelen, P., Swelling due to fission products and additives dissolved within the uranium dioxide lattice, *Journal of Nuclear Materials* **2012**, *427*, 359.

[48] Catlow, C. R. A.; Grimes, R. W., The Charge State of Xe in UO_2, *Journal of Nuclear Materials* **1989**, *165*, 313.

[49] Grimes, R. W.; Catlow, C. R. A., The Stability of Fission Products in Uranium-Dioxides, *Philosophical Transactions of the Royal Society a-Mathematical Physical and Engineering Sciences* **1991**, *335*, 609.

[50] Moore, E.; Corrales, L. R.; Desai, T.; Devanathan, R., Molecular dynamics simulation of Xe bubble nucleation in nanocrystalline UO_2 nuclear fuel, *Journal of Nuclear Materials* **2011**, *419*, 140.

[51] Govers, K.; Verwerft, M., Classical molecular dynamics investigation of microstructure evolution and grain boundary diffusion in nano-polycrystalline UO_2, *Journal of Nuclear Materials* **2013**, *438*, 134.

[52] Ball, R. G. J.; Grimes, R. W., Diffusion of Xe in UO_2, *Journal of the Chemical Society-Faraday Transactions* **1990**, *86*, 1257.

[53] Allen, G. C.; Tempest, P. A.; Tyler, J. W., Coordination Model for the Defect Structure of Hyperstoichiometric $UO_2 + X$ AND U_4O_9, *Nature* **1982**, *295*, 48.

[54] Cheetham, A. K.; Fender, B. E. F.; Cooper, M. J., Defect structure of calcium fluoride containing excess anions I. Bragg scattering, *Journal of Physics C: Solid State Physics* **1971**, *4*, 3107.

[55] Bevan, D. J. M.; Grey, I. E.; Willis, B. T. M., The Crystal-Structure of Bets-U_4O_9-Y, *Journal of Solid State Chemistry* **1986**, *61*, 1.

[56] Bevan, D. J. M.; Greis, O.; Strähle, J., A new structural principle in anion-excess fluorite-related superlattices, *Acta Crystallographica Section A* **1980**, *36*, 889.

[57] Duffy, D. M., Grain Boundaries in Ionic Crystals, *Journal of Physics C-Solid State Physics* **1986**, *19*.

[58] Sayle, D. C.; Mangili, B. C.; Price, D. W.; Sayle, T. X., Nanopolycrystalline materials; a general atomistic model for simulation, *Physical Chemistry Chemical Physics* **2010**, *12*, 8584.

[59] Ellis, W.; Schwoebel, R., LEED from surface steps on UO_2 single crystals, *Surface Science* **1968**, *11*, 82.

[60] Ellis, W. P., LEED Sudies of UO_2 (111) Vicinal Surfaces, *Surface Science* **1974**, *45*, 569.

[61] Taylor, T.; Ellis, W., A LEED study of UO_2(100) vicinal surfaces, *Surface Science* **1978**, *77*, 321.

[62] Castell, M. R., Scanning tunneling microscopy of the UO_2 (111) surface, *Journal of Vacuum Science & Technology B: Microelectronics and Nanometer Structures* **1996**, *14*, 966.

[63] Castell, M. R., Surface structure and bonding in the strongly correlated metal oxides NiO and UO_2, *Journal of Vacuum Science & Technology A: Vacuum, Surfaces, and Films* **1998**, *16*, 1055.

[64] Castell, M.; Muggelberg, C.; Dudarev, S.; Sutton, A.; Briggs, G.; Goddard, D., Imaging insulating oxides by elevated-temperature STM, *Applied Physics A: Materials Science & Processing* **1998**, *66*, S963.

[65] Skomurski, F. N.; Ewing, R. C.; Rohl, A. L.; Gale, J. D.; Becker, U., Quantum mechanical vs. empirical potential modeling of uranium dioxide (UO_2) surfaces: (111), (110), and (100), *American Mineralogist* **2006**, *91*, 1761.

[66] Abramowski, M.; Grimes, R. W.; Owens, S., Morphology of UO_2, *Journal of Nuclear Materials* **1999**, *275*, 12.

[67] Sayle, T. X. T.; Parker, S. C.; Sayle, D. C., Shape of CeO_2 nanoparticles using simulated amorphisation and recrystallisation., *Chemical communications (Cambridge, England)* **2004**, 2438.

[68] Skomurski, F. N.; Shuller, L. C.; Ewing, R. C.; Becker, U., Corrosion of UO_2 and ThO_2: A quantum-mechanical investigation, *Journal of Nuclear Materials* **2008**, *375*, 290.

[69] Nerikar, P. V.; Rudman, K.; Desai, T. G.; Byler, D.; Unal, C.; McClellan, K. J.; Phillpot, S. R.; Sinnott, S. B.; Peralta, P.; Uberuaga, B. P.; Stanek, C. R., Grain Boundaries in Uranium Dioxide: Scanning Electron Microscopy Experiments and Atomistic Simulations, *Journal of the American Ceramic Society* **2011**, *94*, 1893.

[70] Vonlanthen, P.; Grobety, B., CSL grain boundary distribution in alumina and zirconia ceramics, *Ceramics International* **2008**, *34*, 1459.

[71] Lei, Y.; Ito, Y.; Browning, N. D.; Mazanec, T. J., Segregation Effects at Grain Boundaries in Fluorite-Structured Ceramics, *Journal of the American Ceramic Society* **2002**, *85*, 2359.

[72] Baik, H. S.; Kim, M.; Park, G.-S.; Song, S. A.; Varela, M.; Franceschetti, A.; Pantelides, S. T.; Pennycook, S. J., Interface structure and non-stoichiometry in HfO_2 dielectrics, *Applied Physics Letters* **2004**, *85*, 672.

[73] Marinopoulos, A. G., First principles study of segregation to the Σ5(310) grain boundary of cubic zirconia., *Journal of physics. Condensed matter : an Institute of Physics journal* **2011**, *23*, 085005.

[74] Dickey, E. C.; Fan, X. D.; Pennycook, S. J., Structure and chemistry of yttria-stabilized cubic-zirconia symmetric tilt grain boundaries, *Journal of the American Ceramic Society* **2001**, *84*, 1361.

[75] Mao; ZG; Sinnott, Ab initio calculations of pristine and doped zirconia Sigma 5 (310)/[001] tilt grain boundaries **2002**, *85*, 1594.

[76] Fisher, C. A.; Matsubara, H., The influence of grain boundary misorientation on ionic conductivity in YSZ, *Journal of the European Ceramic Society* **1999**, *19*, 703.

[77] Hojo, H.; Mizoguchi, T.; Ohta, H.; Findlay, S. D.; Shibata, N.; Yamamoto, T.; Ikuhara, Y., Atomic Structure of a CeO_2 Grain Boundary: The Role of Oxygen Vacancies, *Nano Letters* **2010**, *10*, 4668.

[78] Feng, B.; Hojo, H.; Mizoguchi, T.; Ohta, H.; Findlay, S. D.; Sato, Y.; Shibata, N.; Yamamoto, T.; Ikuhara, Y., Atomic structure of a Sigma 3 110 /(111) grain boundary in CeO_2, *Applied Physics Letters* **2012**, *100*.

[79] Van Brutzel, L.; Vincent-Aublant, E., Grain boundary influence on displacement cascades in UO_2: A molecular dynamics study, *Journal of Nuclear Materials* **2008**, *377*, 522.

[80] Verkerk, M. J.; Winnubst, A. J. A.; Burggraaf, A. J., Effect of impurities on sintering and conductivity of yttria-stabilized zirconia, *Journal of Materials Science* **1982**, *17*, 3113.

[81] Sutton, A.; Balluffi, R., *Interfaces in Crystalline Materials*, OUP Oxford **1995**.

[82] Shibata, N.; Oba, F.; Yamamoto, T.; Ikuhara, Y., Structure, energy and solute segregation behaviour of 110 symmetric tilt grain boundaries in yttria-stabilized cubic zirconia, *Philosophical Magazine* **2004**, *84*, 2381.

[83] Wolf, D.; Benedek, R.; Levinson, L., Grain Boundary Phenomena in Electronic Ceramics, *Advances in Ceramics* **1981**.

[84] Wolf, D., On the Stability of (001) CSL Twist Boundaries in MgO : A Theoretical Study, *Le Journal de Physique Colloques* **1982**, *43*, C6–45–C6–63.

[85] Sun, C. P.; Balluffi, R. W., Secondary grain boundary dislocations in [001] twist boundaries in MgO I. Intrinsic structures, *Philosophical Magazine A* **1982**, *46*, 49.

[86] Tasker; PW; Duffy; DM, On the Structure of Twist Grain Boundaries in Ionic Oxides **1983**, *47*.

[87] Duffy; DM; Tasker; PW, A General Structure for Coincidence Twist Grain Boundaries in Rock-Salt Structured Oxides **1984**, *67*.

[88] Nerikar, P. V.; Parfitt, D. C.; Casillas Trujillo, L. A.; Andersson, D. A.; Unal, C.; Sinnott, S. B.; Grimes, R. W.; Uberuaga, B. P.; Stanek, C. R., Segregation of xenon to dislocations and grain boundaries in uranium dioxide, *Physical Review B* **2011**, *84*, 174105.

[89] Desai, T. G.; Nerikar, P.; Uberuaga, B. P., The role of grain boundary structure in stress-induced phase transformation in UO_2, *Modelling and Simulation in Materials Science and Engineering* **2009**, *17*, 10.

[90] Dorado, B.; Garcia, P.; Carlot, G.; Davoisne, C.; Fraczkiewicz, M.; Pasquet, B.; Freyss, M.; Valot, C.; Baldinozzi, G.; Simeone, D.; Bertolus, M., First-principles calculation and experimental study of oxygen diffusion in uranium dioxide, *Physical Review B* **2011**, *83*.

[91] Matzke, H., Diffusion-Processes in Nuclear-Fuels, *Journal of the Less-Common Metals* **1986**, *121*, 537.

[92] Olander, D. R.; ; Demonstration, U. S. E. R.; of Reactor Development, D. A. D., *Fundamental aspects of nuclear reactor fuel elements: prepared for the Division of Reactor Development and Demonstration, Energy Research and Development Administration*, Technical Information Center, Office of Public Affairs, Energy Research and Development Administration **1976**.

[93] Kleykamp, H., The chemical state of the fission products in oxide fuels, *Journal of Nuclear Materials* **1985**, *131*, 221.

[94] Aronson, S.; Roof, R. B.; Belle, J., Kinetic Study of the Oxidation of Uranium Dioxide, *Journal of Chemical Physics* **1957**, *27*.

[95] Auskern, A. B.; Belle, J., Oygen Ion Self-Diffusion in Uranium Dioxide, *Journal of Nuclear Materials* **1961**, *3*.

[96] Kupryazhkin, A. Y.; Zhiganov, A. N.; Risovany, D. V.; Nekrassov, K. A.; Risovany, V. D.; Golovanov, V. N., Simulation of diffusion of oxygen and uranium in uranium dioxide nanocrystals, *Journal of Nuclear Materials* **2008**, *372*, 233.

[97] Kurosaki, K.; Yamada, K.; Uno, M.; Yamanaka, S.; Yamamoto, K.; Namekawa, T., Molecular dynamics study of mixed oxide fuel, *Journal of Nuclear Materials* **2001**, *294*, 160.

[98] Sabioni, A. C. S.; Ferraz, W. B.; Millot, F., Effect of grain-boundaries on uranium and oxygen diffusion in polycrystalline UO_2, *Journal of Nuclear Materials* **2000**, *278*, 364.

[99] Marin, J. F.; Contamin, P., Uranium and Oxygen Self Diffusion in UO_2, *Journal of Nuclear Materials* **1969**, *30*, 16.

[100] Vincent-Aublant, E.; Delaye, J. M.; Van Brutzel, L., Self-diffusion near symmetrical tilt grain boundaries in UO_2 matrix: A molecular dynamics simulation study, *Journal of Nuclear Materials* **2009**, *392*, 114.

[101] Arima, T.; Yoshida, K.; Idemitsu, K.; Inagaki, Y.; Sato, I., Molecular dynamics analysis of diffusion of uranium and oxygen ions in uranium dioxide, in Rao, L.; Tobin, J. G.; Shuh, D. K., editors, *Actinides 2009*, volume 9, Iop Publishing Ltd, Bristol **2010**.

[102] Baker, M. M.; Less, L. N.; Orman, S., Uranium + Water Reaction .1. Kinetics, Products and Mechanism, *Transactions of the Faraday Society* **1966**, *62*, 2513.

[103] Wood, D. H.; Snowden, S. A.; Howe, H. J.; Thomas, L. L.; Moon, D. W.; Gregg, H. R.; Miller, P. E., No Title, *Journal of Nuclear Materials* 113.

[104] Roudil, D.; Bonhoure, J.; Pik, R.; Cuney, M.; Jegou, C.; Gauthier-Lafaye, F., Diffusion of radiogenic helium in natural uranium oxides, *Journal of Nuclear Materials* **2008**, *378*, 70.

[105] Bostrom, W. A., US Atomic Energy Comission Report WAPD-183, Technical Report WAPD-183 **1957**.

[106] Rufeh, F.; , D. R.; Pigford, T. H., Solubility of Helium in UO_2, *Transactions of the American Nuclear Society* **1964**, *7*, 90.

[107] Sung, P., *Equilibrium Solubility and Diffusivity of Helium in Single-Crystal Uranium Oxide*, Ph.D. thesis **1967**.

[108] Guilbert, S.; Sauvage, T.; Garcia, P.; Carlot, G.; Barthe, M. F.; Desgardin, P.; Blondiaux, G.; Corbel, C.; Piron, J. P.; Gras, J. M., He migration in implanted UO_2 sintered disks, *Journal of Nuclear Materials* **2004**, *327*, 88.

[109] Yakub, E.; Ronchi, C.; Staicu, D., Diffusion of helium in non-stoichiometric uranium dioxide, *Journal of Nuclear Materials* **2010**, *400*, 189.

[110] Ronchi, C.; Hiernaut, J. P., Helium diffusion in uranium and plutonium oxides, *Journal of Nuclear Materials* **2004**, *325*, 1.

[111] Guilbert, S.; Sauvage, T.; Erramli, H.; Barthe, M. F.; Desgardin, P.; Blondiaux, G.; Corbel, C.; Piron, J. P., Helium behavior in UO_2 polycrystalline disks, *Journal of Nuclear Materials* **2003**, *321*, 121.

[112] Sattonnay, G.; Garrido, F.; Thome, L., Behaviour of helium in UO_2 single crystals: a transmission electron microscopy investigation, *Philosophical Magazine Letters* **2004**, *84*, 109.

[113] Sattonnay, G.; Vincent, L.; Garrido, F.; Thome, L., Xenon versus helium behavior in UO_2 single crystals: A TEM investigation, *Journal of Nuclear Materials* **2006**, *355*, 131.

[114] Roudil, D.; Deschanels, X.; Trocellier, P.; Jegou, C.; Peuget, S.; Bart, J. M., Helium thermal diffusion in a uranium dioxide matrix, *Journal of Nuclear Materials* **2004**, *325*, 148.

[115] Garrido, F.; Nowicki, L.; Sattonnay, G.; Sauvage, T.; Thome, L., Lattice location of helium in uranium dioxide single crystals, *Nuclear Instruments & Methods in Physics Research Section B-Beam Interactions with Materials and Atoms* **2004**, *219*, 196.

[116] Kim, H.; Park, K.; Kim, B. G.; Choo, Y. S.; Kim, K. S.; Song, K. W.; Hong, K. P.; Kang, Y. H., Xenon diffusivity in thoria-urania fuel, *Nuclear Technology* **2004**, *147*, 149.

[117] Martin, G.; Garcia, P.; Sabathier, C.; Carlot, G.; Sauvage, T.; Desgardin, P.; Raepsaet, C.; Khodja, H., Helium release in uranium dioxide in relation to grain boundaries and free surfaces, *Nuclear Instruments & Methods in Physics Research Section B-Beam Interactions with Materials and Atoms* **2010**, *268*, 2133.

[118] Born, M.; Huang, K., *Dynamical Theory of Crystal Lattices*, Oxford **1954**.

[119] Ewald, P. P., Die Berechnung optischer und elektrostatischer Gitterpotentiale, *Annalen der Physik* **1921**, *369*, 253.

[120] Parry, D. E., Electrostatic Potential in Surface Region of an Ionic Crystal, *Surface Science* **1975**, *49*, 433.

[121] Dick, B. G.; Overhauser, A. W., Theory of the Dielectric Constants of Alkali Halide Crystals, *Physical Review* **1958**, *112*, 90.

[122] Gale, J. D., GULP: A computer program for the symmetry-adapted simulation of solids, *Journal of the Chemical Society-Faraday Transactions* **1997**, *93*, 629.

[123] Watson, G. W.; Kelsey, E. T.; DeLeeuw, N. H.; Harris, D. J.; Parker, S. C., Atomistic simulation of dislocations, surfaces and interfaces in MgO, *Journal of the Chemical Society-Faraday Transactions* **1996**, *92*, 433.

[124] Fletcher, R.; Reeves, C. M., Function minimization by conjugate gradients, *The Computer Journal* **1964**, *7*, 149.

[125] Norgett, M. J.; Fletcher, R., Fast Matrix Methods for Calculating Relaxation about Defects in Crystals, *Journal of Physics Part C Solid State Physics* **1970**, *3*, L190.

[126] Verlet, L., Computer "Experiments" on Classical Fluids. I. Thermodynamical Properties of Lennard-Jones Molecules, *Physical Review* **1967**, *159*, 98.

[127] Hockney, R. W.; Eastwood, J. W., *Computer simulations using particles*, McGraw-Hill, New York **1981**.

[128] Nose, S., A Unified Formulation of the Constant Temperature Molecular-Dynamics Methods, *Journal of Chemical Physics* **1984**, *81*, 511.

[129] Melchionna, S.; Ciccotti, G.; Holian, B. L., Hoover Npt Dynamics for Systems Varying in Shape and Size, *Molecular Physics* **1993**, *78*, 533.

[130] Marrink, S.-J.; Berendsen, H. J. C., Simulation of water transport through a lipid membrane, *The Journal of Physical Chemistry* **1994**, *98*, 4155.

[131] Kerisit, S.; Parker, S. C., Free energy of adsorption of water and metal ions on the {1014} calcite surface, *Journal of the American Chemical Society* **2004**, *126*, 10152.

[132] Crabtree, J. C.; Molinari, M.; Parker, S. C.; Purton, J. A., Simulation of the Adsorption and Transport of CO_2 on Faujasite Surfaces, *The Journal of Physical Chemistry C* **2013**, *117*, 21778.

[133] Mott, N.; Littleton, M., Conduction in polar crystals. I. Electrolytic conduction in solid salts, *Transactions of the Faraday Society* **1938**.

[134] Du, Z.; Allan, N.; Blundy, J.; Purton, J.; Brooker, R., Atomistic simulation of the mechanisms of noble gas incorporation in minerals, *Geochimica et Cosmochimica Acta* **2008**, *72*, 554.

[135] Islam, M. S.; Fisher, C. A. J., Lithium and sodium battery cathode materials: computational insights into voltage, diffusion and nanostructural properties., *Chemical Society reviews* **2014**, *43*, 185.

[136] Bertaut, F., Le terme electrostatique de l'energie de surface, *Compte Rendus Hebdomadaire des Seances de l'Academie des Sciences* **1958**, *246*, 3447.

[137] Tasker, P. W., Surface Energies, Surface Tensions and the Surface Structure of the Alklai Halide Crystals, *Philosophical Magazine a-Physics of Condensed Matter Structure Defects and Mechanical Properties* **1979**, *39*, 119.

[138] Oliver, P. M.; Parker, S. C.; Mackrodt, W. C., Computer-Simulation of the Crystal Morphology of Nio, *Modelling and Simulation in Materials Science and Engineering* **1993**, *1*, 755.

[139] Gibbs, J. W., *The Collected Works*, Longmans, Green and Co., New York **1928**.

[140] Wulff, G., Zur Frage der Geschwindigkeit des Wachstums und der auflösung der Krystallflächen, *Zeitschrift fur Krystallographie und Mineralogie* **1901**, *34*, 449–530.

[141] Benson, G. C.; Freeman, P. I.; Dempsey, E., Calculation of Cohesive and Surface Energies of Thorium and Uranium Oxides, *Journal of the American Ceramic Society* **1963**, *46*, 43.

[142] Dolling, G.; Cowley, R. A.; Woods, A. D. B., Crystal Dynamics of Uranium Dioxide, *Canadian Journal of Physics* **1965**, *43*, 1397–&.

[143] Tharmalingam, K., A theoretical study of the energies of formation of point defects in CaF 2 and UO 2, *Philosophical Magazine* **1971**, *23*, 199.

[144] Catlow, C. R. A., Fission-Gas Diffusion in UO_2, *Proceedings of the Royal Society of London Series a-Mathematical Physical and Engineering Sciences* **1978**, *364*, 473.

[145] Walker, J. R.; Catlow, C. R. A., Structural and Dynamic Properties of UO_2 at High Temperatures, *Journal of Physics C-Solid State Physics* **1981**, *14*, L979.

[146] Lewis, G. V.; Catlow, C. R. A., Potential Models for Ionic Oxides, *Journal of Physics C-Solid State Physics* **1985**, *18*, 1149.

[147] Jackson, R. A.; Murray, A. D.; Catlow, C. R. A., The Calculation of Basic Defect Energies of UO_2, *Physica B & C* **1985**, *131*, 136.

[148] Jackson, R. A.; Catlow, C. R. A., Trapping and Solution of Fission XE in UO_2 .1. Single Gas Atoms and Solution from Underpressurised Bubbles, *Journal of Nuclear Materials* **1985**, *127*, 161–166.

[149] Jackson, R. A.; Catlow, C. R. A., Trapping and Solution of Fission Xe IN UO_2 .2. Solution from Small Pressurised Bubbles, *Journal of Nuclear Materials* **1985**, *127*, 167.

[150] Lindan, P. J. D.; Gillan, M. J., The Dynamical Simulation of Super-Ionic UO_2 Using Shell-Model Potentials, *Philosophical Magazine B-Physics of Condensed Matter Statistical Mechanics Electronic Optical and Magnetic Properties* **1994**, *69*, 535.

[151] Sindzingre, P.; Gillan, M. J., A Molecular Dynamics Study of Solid and Liquid UO_2, *Journal of Physics C-Solid State Physics* **1988**, *21*, 4017–4031.

[152] Karakasidis, T.; Lindan, P. J. D., A Comment on a Rigid-Ion Potential for UO_2 - Comment, *Journal of Physics-Condensed Matter* **1994**, *6*, 2965.

[153] Van Brutzel, L.; Delaye, J. M.; Ghaleb, D.; Rarivomanantsoa, M., Molecular dynamics studies of displacement cascades in the uranium dioxide matrix, *Philosophical Magazine* **2003**, *83*, 4083.

[154] Grimes, R. W.; Ball, R. G. J.; Catlow, C. R. A., Site Preference and Binding of Iodine and Cesium in Uranium-Dioxide, *Journal of Physics and Chemistry of Solids* **1992**, *53*, 475.

[155] Grimes, R. W., Simulating the Behaviour of Fission-Products in UO_2, *Scientific Basis for Nuclear Waste Management Xv* **1992**, *257*, 361.

[156] Yamada, K.; Kurosaki, K.; Uno, M.; Yamanaka, S., Evaluation of thermal properties of uranium dioxide by molecular dynamics, *Journal of Alloys and Compounds* **2000**, *307*, 10.

[157] Arima, T.; Yamasaki, S.; Inagaki, Y.; Idemitsu, K., Evaluation of Thermal Properties of UO_2 and PuO_2 by Equilibrium Molecular Dynamics Simulations from 300 to 2000K, *Journal of Alloys and Compounds* **2005**, *400*, 43.

[158] Meis, C.; Chartier, A., Calculation of the threshold displacement energies in UO_2 using ionic potentials, *Journal of Nuclear Materials* **2005**, *341*, 25.

[159] Malavasi, G.; Pedone, A.; Menziani, M. C., Towards a quantitative rationalization of multicomponent glass properties by means of molecular dynamics simulations, *Molecular Simulation* **2006**, *32*.

[160] Sayle, T. X. T.; Molinari, M.; Das, S.; Bhatta, U. M.; Mobus, G.; Parker, S. C.; Seal, S.; Sayle, D. C., Environment-mediated structure, surface redox activity and reactivity of ceria nanoparticles, *Nanoscale* **2013**, *5*, 6063.

[161] Barrett, S. A.; Jacobson, A. J.; Tofield, B. C.; Fender, B. E. F., The Preparation and Structure of Barium Uranium Oxide $BaUO_3 + X$, *Acta Crystallographica Section B-Structural Science* **1982**, *38*.

[162] Fritz, I. J., Elastic Properties of UO_2 at High Pressure, *Journal of Applied Physics* **1976**, *47*.

[163] Gale, J. D.; Rohl, A. L., The General Utility Lattice Program (GULP), *Molecular Simulation* **2003**, *29*, 291.

[164] Yun, Y.; Oppeneer, P. M.; Kim, H.; Park, K., Defect energetics and Xe diffusion in UO_2 and ThO_2, *Acta Materialia* **2009**, *57*, 1655–1659.

[165] Taylor, D., Thermal Expansion Data .2. Binary Oxides with the Fluorite and Rutile Structures, MO_2, and the Antifluorite Structure, M_2O, *Transactions and Journal of the British Ceramic Society* **1984**, *83*, 32.

[166] Macedo, P. M.; Capps, W.; Wachtman, J. B., Elastic Constants of Single Crystal ThO_2 at 25-Degrees-C, *Journal of the American Ceramic Society* **1964**, *47*, 651.

[167] Hadari, Z.; Kroupp, M.; Wolfson, Y., Self Diffusion Measurement of Oxygen in UO_2 by Nuclear Reaction O-18(P,Gamma)F-19, *Journal of Applied Physics* **1971**, *42*.

[168] Sabioni, A. C. S.; Ferraz, W. B.; Millot, F., First study of uranium self-diffusion in UO_2 by SIMS, *Journal of Nuclear Materials* **1998**, *257*, 180.

[169] Grimes, R. W.; Catlow, C. R. A., The Stability of Fission Products in Uranium-Dioxide, *Philosophical Transactions of the Royal Society a-Mathematical Physical and Engineering Sciences* **1991**, *335*, 609.

[170] Colbourn, E. A.; Mackrodt, W. C., The Calculated Defect Structure of Thoria, *Journal of Nuclear Materials* **1983**, *118*, 50.

[171] Loopstra, B. O., Phase Transition in Alpha-U_3O_8 at 210C, *Journal of Applied Crystallography* **1970**, *3*, 94.

[172] Galmarini, S.; Aschauer, U.; Bowen, P.; Parker, S. C., Atomistic Simulation of Y-Doped alpha-Alumina Interfaces, *Journal of the American Ceramic Society* **2008**, *91*, 3643.

[173] Smith, W.; Forester, T. R., DL_POLY_2.0: A general-purpose parallel molecular dynamics simulation package, *Journal of Molecular Graphics* **1996**, *14*, 136.

[174] Gao, Y.; Shewmon, P.; Dregia, S., Coincidence interphase boundaries in MgO/Ni system, *Scripta Metallurgica* **1988**, *22*, 15216.

[175] Garcia, P.; Martin, G.; Desgardin, P.; Carlot, G.; Sauvage, T.; Sabathier, C.; Castellier, E.; Khodja, H.; Barthe, M. F., A study of helium mobility in polycrystalline uranium dioxide, *Journal of Nuclear Materials* **2012**, *430*, 156–165.

[176] Ma, L.; Ray, A. K., Formation energies and swelling of uranium dioxide by point defects, *Physics Letters A* **2012**, *376*, 1499.

[177] Grimes, R. W.; Miller, R. H.; Catlow, C. R. A., The Behaviour of Helium in UO_2 - Solution and Migration Energies, *Journal of Nuclear Materials* **1990**, *172*, 123.

[178] Yakub, E., Helium solubility in uranium dioxide from molecular dynamics simulations, *Journal of Nuclear Materials* **2011**, *414*, 83.

[179] Yun, Y.; Eriksson, O.; Oppeneer, P. M., Theory of He trapping, diffusion, and clustering in UO_2, *Journal of Nuclear Materials* **2009**, *385*, 510.